THE (P,N) CHARGE-EXCHANGE REACTION IN INVERSE KINEMATICS AS A PROBE FOR ISOVECTOR GIANT RESONANCES IN EXOTIC NUCLEI

By

Samuel Israel Lipschutz

A DISSERTATION

Submitted to
Michigan State University
in partial fulfillment of the requirements
for the degree of

Physics—Doctor of Philosophy

2018

ABSTRACT

THE (P,N) CHARGE-EXCHANGE REACTION IN INVERSE KINEMATICS AS A PROBE FOR ISOVECTOR GIANT RESONANCES IN EXOTIC NUCLEI

By

Samuel Israel Lipschutz

Charge-exchange experiments at intermediate (∼100 MeV/u) beam energies have long been a tool to study isovector giant resonances in nuclei. Since the 1970s, many probes and techniques have been developed to study and isolate different isovector giant resonances, which have illuminated the spin-isospin response of nuclei. However, these experiments have almost solely been restricted to stable nuclei. The advent of rare-isotope beam facilities has created increased interest in studying these resonances in radioactive nuclei. Such experiments are important for better constraining models that aim to describe the properties of nuclei and nuclear matter, with important applications in astro and neutrino physics. To take advantage of these rare-isotope facilities, new techniques in inverse kinematics need to be developed and validated. This thesis presents a new technique for studying isovector giant resonances on unstable nuclei in the $\Delta T_z = -1$ direction, through the (p,n) reaction in inverse kinematics. The technique was validated through the measurement of the absolute differential cross section in the neutron-rich ^{16}C(p,n)^{16}N* reaction at 100 MeV/u up to ∼20 MeV of excitation energy. From the data, the Gamow-Teller (GT) strength distribution [B(GT)] and the spin-dipole (SD) differential cross section were extracted. The extracted B(GT) was compared with shell-model calculations in order to test their reliability in the neutron-rich, high-excitation energy regime. A total GT strength up to 20 MeV was extracted and compared to the model-independent sum rule, giving a quenching factor of 73.5 $\pm 2.8(st) \pm 15.5(sys)$%. This experiment provided one of the first measurements of isovector

strength in a neutron-rich nucleus and has paved the way for future exploration of isovector giant resonances in exotic nuclei.

This thesis is dedicated to you, the reader, so that you may feel special.

ACKNOWLEDGMENTS

No PhD is completed in isolation, and certainly not this one. Without the help and guidance of countless people, my research could not have been completed, and this thesis could not have been written. Though I cannot thank everyone by name, know that I am grateful for all the help you have given me and for what it has allowed me to accomplish.

I would like to give a special and wholehearted thanks to my advisor, Remco Zegers. Even in the depths of the great "factor of four" debate of 2017, you continued to provide the same excellent advice and mentorship that you have given me over the past six years. Though our opinions on Dutch licorice sharply diverge, it has not impacted your tireless commitment to see me through to the end. I would also like to thank the members of my committee for providing guidance and assistance throughout my time at the lab: Sean Liddick, Alex Brown, Michael Thoennessen, and Norman Birge.

Shumpei Noji requires special acknowledgment. Without your steadfast assistance much of this thesis would not exists. Throughout the years you have gone above and beyond to help me many times. Thank you.

By any measure, completing a PhD is a difficult task. Beyond the research and coursework challenges, maintaining the necessary perseverance and optimism that is needed to finish is an undertaking of its own. This was only possible with the help and friendship of my fellow students. Alanna, Bethany, Charlie, Chris, Eric, and Juan: you have been true friends since the beginning.

Most importantly, I would like to thank my mother and father. Naturally, without you, I wouldn't have gotten very far in life. It must be a distinct source of pride to have two sons who have squandered their twenties obtaining their PhDs.

Finally, I want to thank Jeny for supporting and encouraging me since the day we met. The help you have given me in just the last few days has been immeasurable. You have been there for me throughout the toughest parts of this process. I dont know how I could have done it without you.

TABLE OF CONTENTS

LIST OF TABLES

LIST OF FIGURES

Chapter 1

Introduction

1.1 The Atomic Nucleus

Nuclear physics is a unique field of study. While it has had significant impact on the world from its beginnings, a robust and a comprehensive predictive theory remains elusive. The most basic goal of nuclear science is to understand the forces that bind the atomic nucleus together and, with those forces, understand the many phenomena observed in nuclei and their interactions. Though they are not fundamental particles, the nuclear problem is typically defined in terms of the nucleon constituents—protons and neutrons—that interact via the strong nuclear force.

Beginning with Rutherford's discovery of the nucleus [1], the field has grown to discover more than 3000 different isotopes out of approximately 7000 predicted to exist [2]. These different nuclei are organized in a way similar to the periodic table of the elements, called the chart of the nuclides. This chart is shown in Fig. 1.1, where the number of neutrons is plotted on the horizontal axis and the number of protons is plotted on the vertical axis.

The vertical and horizontal dashed lines in Fig. 1.1 indicated the "magic numbers" (2, 8, 20, 28, 50, 82, 126). The magic numbers and their meaning were a crucial discovery for nuclear physics. They correspond to numbers of nucleons that form and designate particularly stable or strongly bound nuclei. This is a phenomenon that is similar to the noble

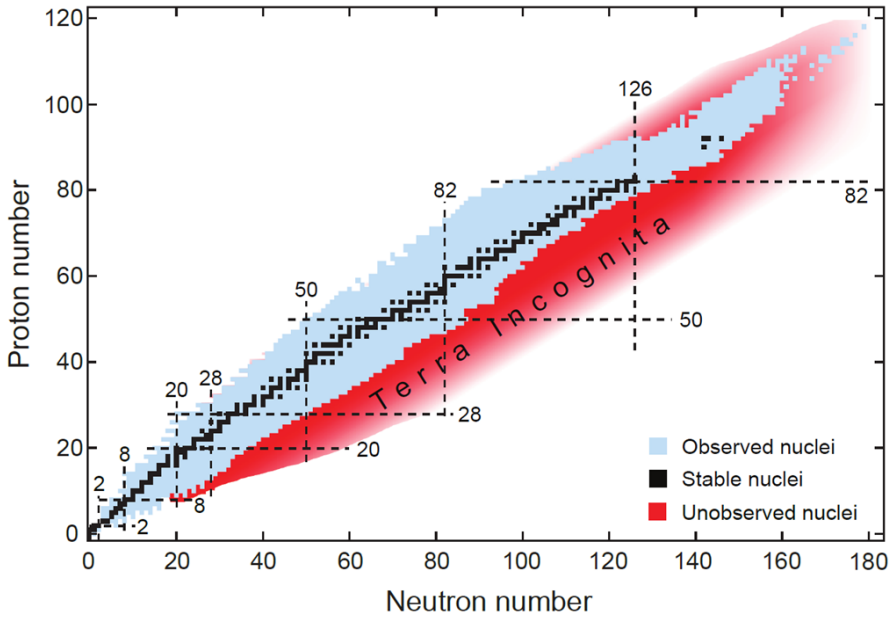

Figure 1.1: Chart of the nuclides showing the number of neutrons on the x axis and the number of protons on the y axis. The black squares show the stable nuclei, the blue region shows nuclei that have been observed but are unstable, and the red region shows nuclei that are predicted to exist but have not been observed experimentally. The dashed lines show the nuclear magic numbers. Figure taken from Ref. [3].

gases of atomic physics, where a completely filled outer electron shell makes them inert. The magic numbers were first recognized by Maria Mayer in 1948 [4], and later further explained by Mayer [5], and Haxel, Jensen, and Suess in 1949 [6]. The insight made independently by Mayer and Jensen et al. was the necessity of a strong spin-orbit interaction to reproduce the observed magic numbers. Both Mayer and Jensen were awarded a portion of the Nobel Prize in Physics in 1963 for creating and explaining the nuclear shell model.

1.2 The Nuclear Shell Model

The nuclear shell model organizes the protons and neutrons of a nucleus into shells that attempt to reproduce the observed magic numbers. Strictly speaking, the nucleus is a self-bound system of A nucleons, where the attractive nuclear potential between all the particles

binds the nucleus. The shell model, however, is a mean-field approximation that describes the motion of the individual nucleons within an average potential that models the total effect of the remaining $A-1$ nucleons. This marks a significant difference from the atomic case. For an atom the negatively charged electrons are bound by the Coulomb potential well of the positively charged nucleus, and not by the collective effect of all other electrons in the system.

There are two traditional forms of the potential used in the nuclear shell model: a harmonic-oscillator

$$V(r) = \frac{1}{2}m\omega^2 r^2, \tag{1.1}$$

or Woods-Saxon potential

$$V(r) = \frac{V_0}{1 + exp[(r-R)/a]}. \tag{1.2}$$

For the harmonic-oscillator potential, m is the nucleon mass and ω is the oscillator frequency. For the Woods-Saxon potential, V_0 is the depth, R is the radius, and a is the diffuseness of the potential well. In addition to the potential well described by $V(r)$, a term to model the spin-orbit interaction between the nucleons is also included. For the spin-orbit potential, it is important to note that it must vanish at the center of the nucleus [7]. This motivates using a potential shape that is peaked at the surface. The derivative of a Wood-Saxon is typically used,

$$V_{so}(r) = V_{so}\frac{1}{r}\frac{df_{so}(r)}{dr}, \tag{1.3}$$

where

$$f_{so} = \frac{1}{1 + exp[(r-R_{so})/a_{so}]} \tag{1.4}$$

These potentials are summarized in Fig. 1.2, where the neutron single-particle states of

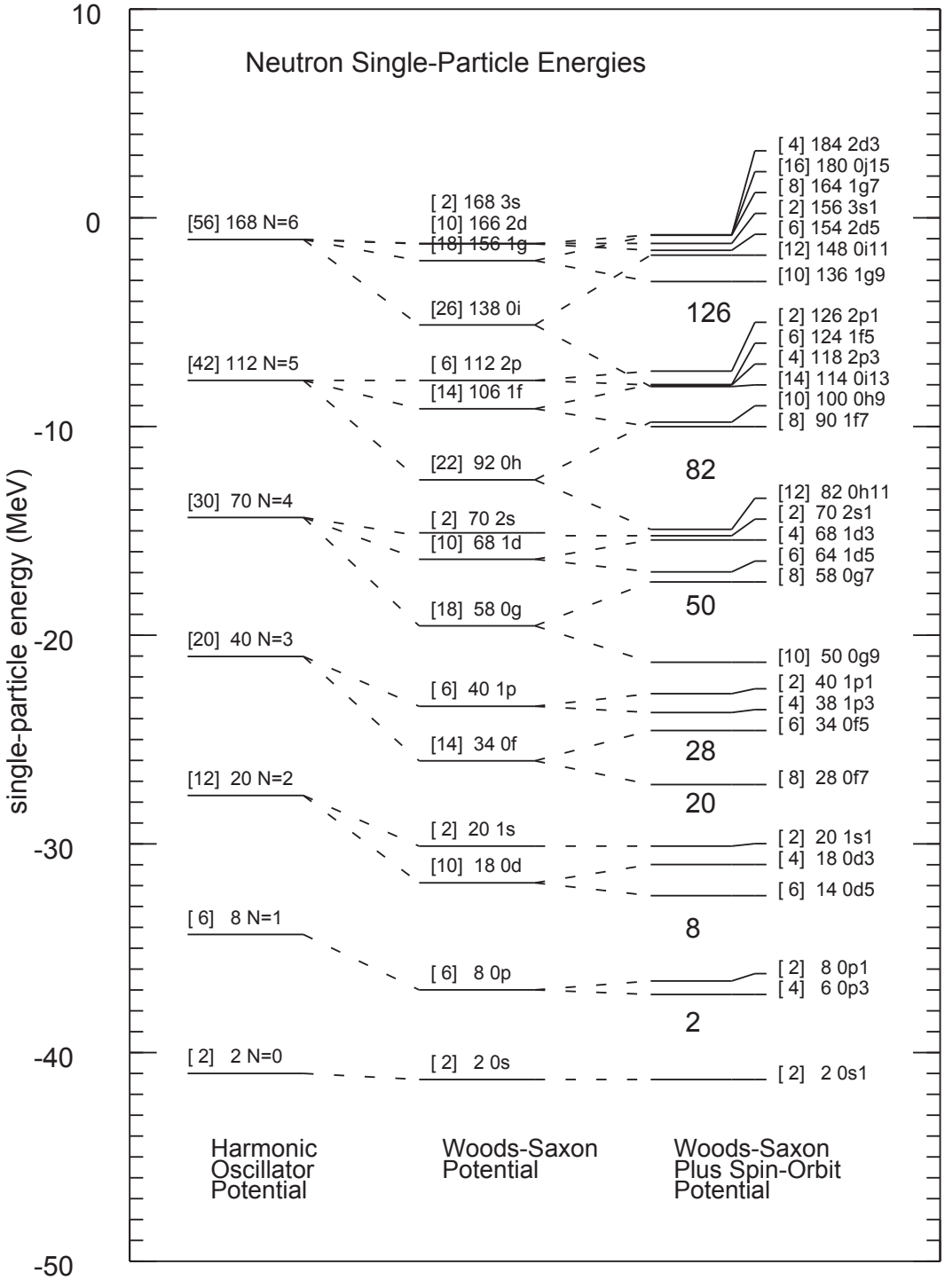

Figure 1.2: Neutron single-particle states in ^{208}Pb with three different potential models. The left shows a harmonic oscillator potential, the center shows a Woods-Saxon potential, and the right shows a Woods-Saxon plus spin-orbit potential. The numbers in brackets give the maximum number of neutrons that each state can hold while the adjacent numbers give the running sum. Figure taken from Ref. [7].

^{208}Pb are shown. Though the harmonic oscillator clearly has the wrong asymptotic behavior (V(r$\rightarrow \infty$)$\rightarrow \infty$), it reproduces several of the observed magic numbers (2, 8, and 20). The Woods-Saxon potential, shown in the center of Fig. 1.2, breaks the the l degeneracy by bringing states with higher l values down in energy, but still fails to reproduce the observed magic numbers above 20. Adding the spin-orbit term completely breaks the degeneracy of the states and reproduces the magic numbers as Mayer and Jensen et al. first showed. The spin-orbit term in the nuclear case is of opposite sign to the atomic case, bringing higher J states lower in energy. This is shown as the right column in Fig. 1.2.

This basic description of the shell model is referred to as the independent-particle model and works well for nuclei with one nucleon more or less than a magic number. In these circumstances the nucleus can be modeled well by an inert "core" and one orbiting nucleon. There the low-lying excited states of the nucleus can be understood as the valence nucleon simply moving into higher orbitals of the potential created by the core. However, in the more common case of several nucleons outside a closed core, the problem becomes more complex, since the interaction between the valence nucleons must be taken into account.

This is done by solving the the Schrödinger equation,

$$\hat{H}\Psi = E\Psi, \tag{1.5}$$

where $\hat{H}$ is the Hamiltonian, Ψ is the wave function, and E is the energy. Unfortunately, we cannot write down the full expression for $\hat{H}$, since we don't know the true shape of the nuclear potential. Following the notation of [7], the Hamiltonian is often modeled as,

$$H = \left(\sum_{k=0}^{n}(T_k + U_k)\right) + \left(\sum_{k<l}^{n} V_{kl}\right) = H^0 + W, \tag{1.6}$$

where T_k is the kinetic energy operator, U_k is the single particle potential, n is the number of nucleons, and V_{kl} is a two body interaction that is chosen to reproduce the experimental data. Using the single particle states from H^0 as a basis, the problem is cast into a matrix-diagonalization problem where the off-diagonal terms come from the interaction. This gives a series solution of the form,

$$\Psi = \sum_{n=0}^{\infty} = c_n \Phi_n \tag{1.7}$$

where Φ_n is a Slater determinate for each possible arrangement of nucleons among the different single-particle states and c_n is the coefficient from the diagonalization. A clear problem with equation 1.7 is that the sum goes to infinity, since there are an infinite number of single-particle states at higher and higher energies. This is clearly impossible to calculate, so the series must be truncated. This puts the problem into a specific model space where only certain single-particle levels are used (for example only the $0p$ shell). This approach is used in modern shell-model programs such as OXBASH [8], NuShell, and NuShellX [9]

The shell structure and associated magic numbers presented in Fig. 1.2 were developed and validated with experimental information from stable nuclei. However, in unstable nuclei the energies between shells can change and the ordering of the single-particle levels can change. The large shell gaps that create the familiar magic numbers can vanish and create new, smaller ones at different proton and neutron numbers. This phenomenon is often referred to as *shell evolution* or *shell inversion*, and understanding its behavior is a significant goal of nuclear physics (see Ref. [10] and references therein). Light, unstable nuclei where large neutron-to-proton ratios can be achieved have been used as a fertile testing ground for nuclear structure models and for understanding the role of shell evolution in nuclei. Of particular interest to charge-exchange studies is the role that the isovector part of the

nucleon-nucleon (NN) interaction plays in shell evolution. This role has been investigated previously and the interested reader is directed to Refs. [11, 12] for more information.

1.3 Giant Resonances

Giant resonances in nuclei occur at high excitation energy, where a large fraction of the nucleons participate in a collective mode. Historically, they are considered a *giant* resonance if they exhaust more than 50% of the associated sum rule (an expression for the total amount of strength for a given operator, see Section 1.8 for more information) for that mode. Giant resonances were first observed by Bethe and Gentner in 1937 [13], where they excited the isovector giant dipole resonance (IVGDR) through photo absorption experiments on a variety of targets. Systematic study of the IVGDR was enabled in 1947 with the development of the betatron, which allowed for high-energy γ rays to be produced through the bremsstrahlung process [14]. This led Baldwin et al. to study the photo-fission and photo-absorption responses of nuclei in detail from 10-100 MeV [15, 16]. In the early 1970s, a second giant resonance was observed by Pitthan and Walcher in the (e, e') reaction at 65 MeV on ^{208}Pb [17]. This was determined to be the isoscalar giant quadruple resonance (ISGQR). Having found both isovector and isoscalar giant resonances, many experiments were undertaken to study them in detail using a variety of probes. The interested reader is referred to Ref. [14] for more information on the historical development of giant resonances.

From a macroscopic perspective, giant resonances can be thought of as resonant oscillations of a nuclear liquid drop. Some of these modes are depicted in Fig. 1.3, where they are organized in terms of their orbital angular momentum. Shown in the figure are breathing modes ($\Delta L = 0$), where the protons and neutrons oscillate radial outwards, dipole modes

($\Delta L = 1$), where the protons and neutrons oscillate against themselves, quadrupole (ΔL=2) and octupole modes ($\Delta L = 3$). As depicted in the figure, each of these resonances can occur with spin and isospin degrees of freedom. When a unit of spin is transferred ($\Delta S = 1$), the spin up (down) protons and neutrons will oscillate out of phase with the spin down (up) protons and neutrons. Similarly, a unit of isospin ($\Delta T = 1$) can be transferred, causing the protons to oscillate out of phase with the neutrons. For example, the isovector spin giant dipole resonance (IVSGDR or spin-dipole resonance (SDR)) can be thought of as protons with spin up oscillating against neutrons with spin down, superimposed with the reverse.

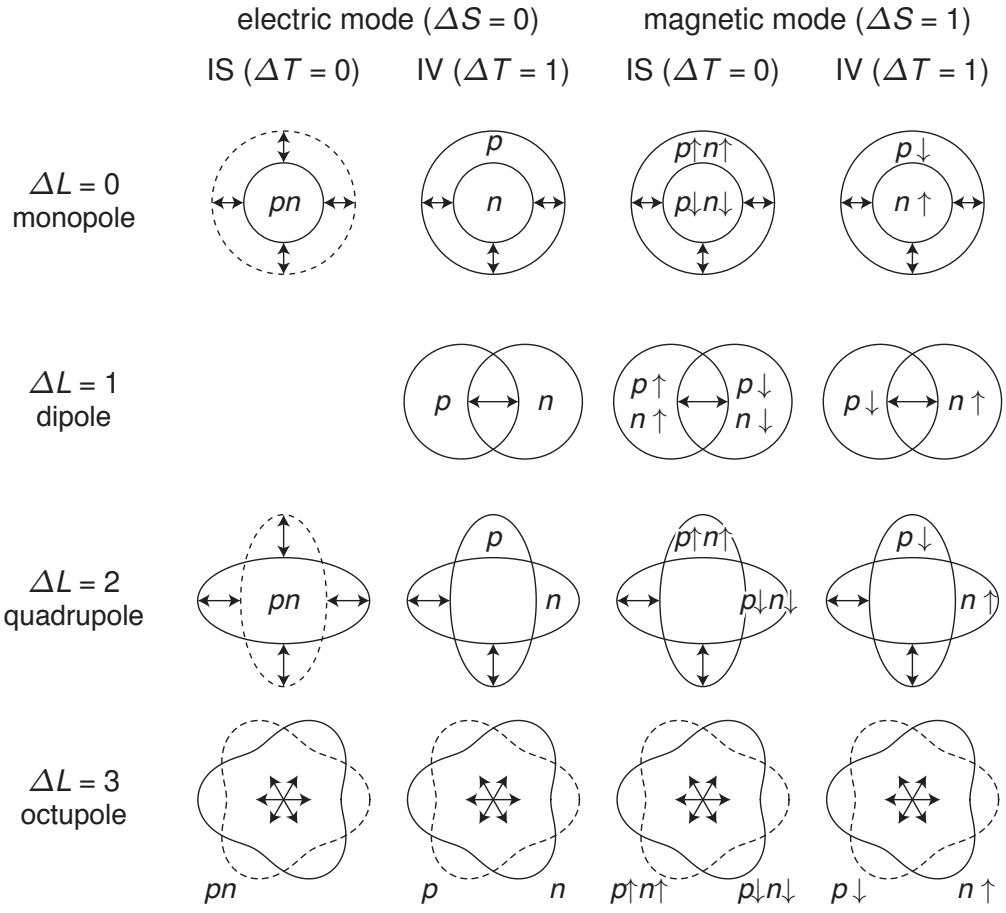

Figure 1.3: Schematic of the macroscopic depiction of various giant resonances. For each ΔL value, the different possible spin and isospin transfers are shown. Figure taken from Ref. [18].

From a microscopic perspective, giant resonances are a coherent superposition of one-particle, one-hole (1p-1h) excitations. A general expression for the operators that mediate giant resonances can be written as,

$$O^{\pm}_{JM} = \sum_{k} r_k^{\lambda} [Y_{\Delta L} \otimes \hat{\sigma}_k]^J_M \hat{\tau}_{\pm k}, \tag{1.8}$$

where $Y_{\Delta L}$ is a spherical harmonic, $\hat{\sigma}$ is the vector spin operator, $\hat{\tau}_{\pm}$ is the isospin ladder operator, k runs through each nucleon in the target nucleus, $\lambda = 2\Delta n + \Delta L$, and n is the principle quantum number. For example, the isovector ($\Delta T = 1$) spin ($\Delta S = 1$) giant dipole ($\Delta L = 1$) resonance and can be written as,

$$SD^{\pm}_{JM} = \sum_{k} r_k [Y_1 \otimes \hat{\sigma}_k]^J_M \hat{\tau}_{\pm k} \tag{1.9}$$

This picture is especially important for the Gamow-Teller (GT) and the Fermi (F) giant resonances, which involve only spin and isospin degrees of freedom and therefore have no macroscopic, oscillatory picture. These resonances can be excited and studied by charge-exchange reactions and will be discussed in Section 1.4.

In general, giant resonances offer powerful insight into the collective properties of nuclei and provide a stringent testing ground for nuclear structure models at high excitation energy. Many studies have investigated isoscalar electric resonances using the (α, α') reaction to extract bulk nuclear properties and to test theoretical models [19, 20, 21, 22, 23, 24, 25, 26, 27, 28, 29]. In particular, isoscalar monopole resonances can be used to extract the compression modulus of nuclear matter K_{nm} [30]. This was first done by Youngblood et al. who measured the ISGMR strength distributions in several nuclei, from which they determined $K_{nm} =$

231 ± 5 MeV [31, 32]. Searches for the isovector giant monopole resonance (IVGMR) have also been done on several stable nuclei, using nuclear [33, 34, 35] and pion [36] charge-exchange reactions. Studying the IVGMR resonance gives a fundamental understanding of the isovector part of the residual nuclear interaction and provides information on isospin-symmetry breaking and isospin mixing in nuclei [33, 34].

The spin-dipole resonance can be used to give a model-independent measure of neutron skin thickness through its non-energy-weighted sum rule. This was done recently for the first time by Yako et al., where ^{90}Zr(p,n) and ^{90}Zr(n,p) were measured at 300 MeV. This gave a neutron rms radius of $\sqrt{\langle r^2 \rangle_n} = 4.26 \pm 0.04$ fm and a neutron skin thickness of $\delta_{np} = 0.07 \pm 0.04$ fm [37]. Neutron skin thickness has also been extracted from studies of the pygmy dipole resonance in unstable nuclei [38]. Neutron skin thicknesses make constraints on the neutron equation of state that are important at high density and so are useful for neutron star properties [39, 40, 41]. Of particular interest to this thesis are the isovector giant resonances induced by charge-exchange reactions. They have received decades of study from a variety of probes. The following sections present details about charge-exchange reactions and their role in the giant resonance arena.

1.4 Nuclear Charge-Exchange Reactions

Nuclear charge-exchange reactions occur when participating nuclei exchange charge. The nuclei's proton number changes by one ($\Delta Z = \pm 1$), while its mass number remains the same ($\Delta A = 0$). In terms of isospin formalism, this occurs with $\Delta T_z = \pm 1$. As an illustrative example, consider the case of the ^{12}C(p,n)^{12}N reaction. The isospin projection for ^{12}C can

be easily calculated as,

$$T_z = \frac{N - Z}{2} = \frac{6 - 6}{2} = 0. \tag{1.10}$$

The total isospin for the ground state can be taken as the smallest value that can accommodate the projection, so ^{12}C must be $T = 0, T_z = 0$. Following similar arguments, ^{12}N must be $T = 1, T_z = -1$. Therefore, charge-exchange reactions must change the isospin by 1, and are thus isovector transitions ($\Delta T = 1$). In general, charge-exchange reactions can transfer any amount of orbital angular momentum (ΔL) and can occur with or without a spin transfer ($\Delta S = 0, 1$). This gives charge-exchange reactions access to a wide variety of spin-isospin responses in nuclei [42].

The simplest reaction meditated by charge-exchange is the Fermi transition, which is characterized by the quantum numbers $\Delta T = 1$, $\Delta L = 0$, $\Delta S = 0$. Using Equation 1.8 the operator for the Fermi transition must be,

$$O(F) = \sum_k \hat{\tau}_{\pm k}. \tag{1.11}$$

Nearly all the Fermi transition strength is located in the so-called isobaric analog state (IAS). The next simplest excitation is the Gamow-Teller (GT) ($\Delta T = 1$, $\Delta L = 0$, $\Delta S = 1$) transition,

$$O(GT) = \sum_k \hat{\sigma}_k \hat{\tau}_{\pm k}, \tag{1.12}$$

where the spin-transfer operator has been added. The GT and Fermi transitions, induced through charge-exchange reactions, have great interest since they connect the same initial and final states as β decay. It has been shown, as outlined in Sections 1.5 and 2.3, that there exists a proportionality between charge-exchange cross sections for Fermi and GT transitions

and their associated β decay matrix elements.

The GT strength is defined as the square of the matrix element between an initial state i and final state f mediated by the GT operator,

$$B(GT_{\pm}) = \frac{|\langle f||\sum_k \hat{\sigma}_k \hat{\tau}_{\pm k}||i\rangle|^2}{2J_i + 1}, \tag{1.13}$$

where the $\langle f||O||i\rangle$ notation refers to the reduced matrix element and J_i is the total angular momentum of the initial state. The GT and Fermi strength are directly related to the β decay ft value (partial half-life times the phase space factor f),

$$ft = \frac{C}{B(F) + (g_A/g_V)^2 B(GT)}, \tag{1.14}$$

where C is a constant, $B(F)$ is the Fermi strength, and g_A and g_V are the axial and vector coupling constants. Throughout this thesis, the value $g_A/g_V = 1.251 \pm 0.009$ as determined from neutron β decay is used [43]. Further, the convention for B(GT) is that the β decay of the free neutron has B(GT)=3.

The Fermi strength is concentrated into a single transition to the isobaric analog state (IAS), where the wave function has only been modified by a neutron becoming a proton or vice-versa. This means that for transitions to other states, the relation simplifies to,

$$ft = \frac{C}{(g_A/g_V)^2 B(GT)}, \tag{1.15}$$

connecting β decay half-life measurements directly to the GT strength. However, unlike β decay, charge-exchange reactions are not limited in excitation energy by the β-decay Q-value window. This gives charge-exchange reactions access to the full isovector response of nuclei,

up to high excitation energy, and therefore makes them a powerful tool for the investigation of isovector excitations, including the isovector giant resonances.

1.5 Historical Development of Charge-Exchange Probes

Charge-exchange experiments began in 1958 when a proton beam was impinged on a deuterium gas target—the first (p,n) reaction [44]. In 1961, (p,n) measurements were done by Anderson et al. [45], where the IAS was first measured. In 1962, a measurement by Bowen et al. [46] saw the GT giant resonance, but it was incorrectly interpreted as the IAS. It was not until 1975 that Doering et al. [47] first measured and identified the GT giant resonance in the ^{90}Zr(p,n) reaction at 35 MeV. In 1980, the nature of the proportionality between (p,n) cross section and GT strength was determined by Goodman et al. [48]. Again studying the ^{90}Zr(p,n) reaction, but at 120 MeV, Goodman et al. observed that the GT giant resonance was preferentially excited at 0° in the (p,n) charge-exchange cross section and with simple corrections for distortion effects, proportional to GT strength. These initial experiments began a long line of (p,n) measurements on a range of stable targets, many of which were done at the Indiana University Cyclotron Facility (IUCF)[49, 50, 48, 51, 52, 53, 54, 55].

Throughout the 1980s, there was clear empirical evidence for the proportionality between the (p,n) charge-exchange cross section and GT strength. However, it wasn't until 1987 that the theoretical framework for the proportionality was formalized by Taddeucci et al. [56]. The success of (p,n) charge-exchange reactions for understanding the collective spin-isospin modes in nuclei motivated finding other charge-exchange probes to isolate different isovector resonances. The (n,p) [57] and (t,^{3}He) [58] reactions were first used in the 1970s to explore the $\Delta T_z = +1$ direction. Additionally, (d,^{2}He) experiments have been undertaken [59, 60].

Heavy ion probes such as the (^{7}Li,^{7}Be) were used to add spin flip selectivity [61]. In the mid 1980s, the resolution of the $\Delta T_z = -1$ direction was improved over (p,n) with the introduction of the (^{3}He,t) reaction [62]. For all of these probes, similar proportionality relationships between cross section and B(GT) were established.

The aforementioned probes and techniques have all contributed to a detailed and rich understanding of giant resonances on stable nuclei. However, with the advent of rare-isotope beam facilities, studying isovector giant resonances on unstable nuclei has received increased interest. Measuring the GT giant resonance in unstable, neutron-rich nuclei in the medium-heavy mass region validates nuclear-structure models needed for calculating electron capture rates [63, 64]. These rates (particularly in the *pf* and *sdg* shells) play an important role in type II supernovae (see Ref. [65] and reference therein). With unstable neutron-rich nuclei, increased neutron excesses make charge-exchange studies more sensitive to neutron skin measurements—which makes more stringent constraints than are possible with stable nuclei. In general, studying isovector giant resonances in exotic nuclei is useful for understanding the underlying nuclear structure since the sensitivity of the underlying degrees of freedom is increased compared to stable nuclei [14].

To perform charge-exchange experiments with rare isotopes, new techniques need to be developed for experiments in inverse kinematics, where the unstable nucleus of interest is impinged on the stable probe serving as the target. In the $\Delta T = +1$ direction this has been done with the (^{7}Li,^{7}Be) reaction with a rare-isotope beam of ^{34}P [66]. For the $\Delta T_z = -1$ direction, a relatively new technique for studying isovector giant resonances (GT and SD giant resonance) has been developed using the (p,n) reaction in inverse kinematics. The development and validation of this probe is the focus of this thesis.

1.6 The (p,n) Probe in Inverse Kinematics

In (p,n) experiments in inverse kinematics, an unstable isotope is impinged on a thick, liquid-hydrogen target. The energy and angle of the low-energy recoiled neutron is measured. Missing-mass spectroscopy is used to calculate the center-of-mass (COM) scattering angle and excitation energy of the ejectile (see Chapter 3 for technical details). This technique has several advantages:

- The (p,n) probe is the simplest of the charge-exchange probes. It is well established and provides model independent extractions of GT strength.
- The lower beam rates in rare-isotope experiments can be offset by a thick liquid hydrogen target. Since the experiment is performed in inverse kinematics, the excitation energy resolution is less sensitive to the energy loss of the beam in the target. Further, the neutron can easily escape the target for detection.
- The simplicity of the missing-mass spectroscopy allows for the extraction of the isovector response up to high excitation energy of any nucleus. The scattering angle and excitation energy come from the measurement of the recoiled neutron.

The technique was first used to measure the ^{56}Ni(p,n) and ^{55}Co(p,n) reactions in inverse kinematics at 110 MeV/u [63, 64]. Other measurements have also been performed, including ^{12}Be(p,n)^{12}B [67] and an invariant-mass measurement of the ^{14}Be(p,n)^{14}B reaction at 69 MeV/u [68]. Instead of probing the isovector response of the nucleus up to high excitation energies, Ref. [64] focused on benchmarking electron-capture rate calculations needed for core-collapse supernovae simulations. The next round of experiments utilizing this technique have since occurred, with ^{132}Sn(p,n)^{132}Sb at RIKEN and ^{16}C(p,n)^{16}N at NSCL (experiment

number e10003). The ^{16}C(p,n)^{16}N experiment is described in this thesis and seeks to validate the probe's ability to explore the isovector response of radioactive nuclei up to high excitation energies.

^{16}C is a good choice for this goal for the following reasons:

- Since it is a light system the cross section is expected to be relatively high due to relatively small distortion effects from the nuclear mean field.
- High beam rates are achievable, ensuring that sufficient statistics will be obtained in the measurement.
- The whole GT resonance region can be covered in the experiment.
- Detailed shell-model calculations are feasible for comparison.

With the full GT response measured, the quenching of the GT strength in an unstable neutron rich-nucleus can be measured (assuming the $\beta+$ strength is zero). Alongside the full GT giant resonance, a portion of the SD resonance will be measured. This cross section can be compared to shell-model and reaction code predictions.

The shell-model depiction of the GT and SD resonances are given in Fig. 1.4. The different 1p-1h contributions to the resonances are shown. ^{16}C is a cross-shell nucleus, with two neutrons in the *sd* shell. For the GT transitions, there will be contributions from both the *p* and *sd* shells. In the notation of the OXBASH program, configurations with two nucleons in the *sd* shell are called $2\hbar\omega$ configurations. This naming is with reference to an ^{16}O core, which is a 0 $\hbar\omega$ configuration. Since GT transitions are associated with no change in $\hbar\omega$, the final states in ^{16}N will be remain in $2\hbar\omega$ configurations. The SD resonance changes major oscillator shells ($\hbar\omega = 1$), so it will have many contributions including transitions into

the pf shell. This means that there can be transitions from the $2\hbar\omega$ configuration of the ^{16}C ground state to either 1 or 3 $\hbar\omega$ configurations in ^{16}N. To include all of these different components the shell-model calculations were done in the full *spsdpf* model space. The details and results of shell-model calculations for these resonances are given in Chapter 2.

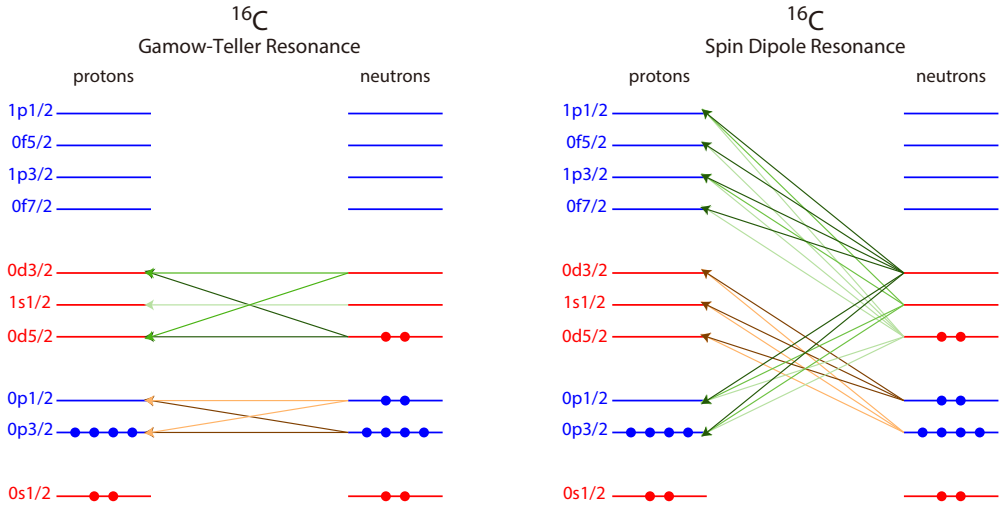

Figure 1.4: Shell-model schematic showing the different 1p-1h contributions of the GT and SD giant resonances in the ^{16}C(p,n)^{16}N reaction.

1.7 β Decay of ^{16}C

Several β-decay studies of ^{16}C have already been performed [69, 70, 71]. From the first measurement in 1976 by Alburger et al., the low-lying structure of ^{16}N has generated interest as a testing ground for shell-model interactions. Initial efforts by Snover et al. with the Millener-Kurath (MK) interaction failed to reproduce the observed GT strength for the two, strong GT states at 3.3 and 4.3 MeV [72]. Significant improvements were made by Warburton et al. [73] in 1992 with the use of the WBT interaction. There, the 0p shell part of the interaction was determined simultaneously with the cross-shell part, which improved the results. A more recent β-decay study by Grevy et al. identified a new state at 6 MeV

[71]. Table 1.1 shows a summary of the 1^+ states that have been observed in β decay measurements and the corresponding shell-model results.

Experimental				Theory	
E_x [MeV]	J^π	log(ft)	B(GT)	B(GT)_{MK}	$\text{B(GT)}_{\text{WBT}}$
3.353	1^+	3.551 ±0.012	1.104 ± 0.03	0.001^a	0.84^a
4.320	1^+	3.83 ±0.05	0.586 ± 0.07	0.903^a	0.21^a
6.00	1^+	3.86 ±0.1	0.543 ± 0.12		0.36^b

Table 1.1: Summary of the results from previous β-decay measurements of ^{16}C and from theoretical calculations. ^{a} taken from Ref. [73]. ^{b} taken from Ref. [71].

These β-decay experiments have provided constraints and insights for shell-model theories for the low-lying states in ^{16}N. With the ^{16}C(p,n)^{16}N measurement, the full GT response of ^{16}N will be probed. This will provide a stringent test for the shell model at higher excitation energies, which are unavailable to β-decay studies.

1.8 The Gamow-Teller Sum Rule

Many model-independent sum rules exist for the operators that mediate the excitation of giant resonances. They are categorized into energy-weighted (EW) and non-energy-weighted (NEW) sum rules (SR). For general information about SRs, the reader is referred to Ref. [14]. Of interest to this thesis is the NEWSR for the GT and the Fermi operators. The GT sum rule is,

$$S_- - S_+ = 3(N - Z), \tag{1.16}$$

and the Fermi sum rule is,

$$S_- - S_+ = (N - Z). \tag{1.17}$$

The $S_{\pm}$ indicates the total strength in the $\beta+$ and $\beta-$ directions, for the GT and Fermi operators respectively. Equations 1.16 and 1.17 are simple and model independent—all you need to know is the N and Z of the initial nucleus. A full derivation of the GT sum rule is given in Appendix A. For the neutron-rich case of ^{16}C, Equation 1.16 is simplified, since the transitions in the $\beta+$ direction will be Pauli blocked. In this case, Equation 1.16 can be approximated as,

$$S_{-} \approx 3(N - Z). \tag{1.18}$$

This means that the total summed strength in ^{16}C can be probed by measuring only the $\beta-$ direction and then directly comparing the result with the sum rule. This will be done in the ^{16}C(p,n)^{16}N reaction described in this thesis. For the Fermi transition, close to 100% of the NEWSR is exhausted in the transition to the IAS. For ^{16}C, this would mean that the Fermi strength in the $\beta-$ direction would be 4.

1.9 Quenching of Gamow-Teller Strength

A reoccurring feature of charge-exchange and β -decay studies is missing GT strength. In β-decay experiments, the strength from individual states is compared to shell model predictions where a systematic reduction is seen. With charge-exchange reactions, the whole GT response can be probed and the summed strength can be extracted, including the GT giant resonance. When the total strength is compared to the model-independent sum rule for the GT operator, a systematic reduction in strength is also observed. This phenomenon is known as quenching and has been studied for many decades [74, 75]. Consider again the

form of GT single particle operator,

$$O(GT) = g_A/g_V \hat{\vec{\sigma}}\hat{\tau}_{\pm}, \tag{1.19}$$

where the coupling constants are included. This equation gives the free-nucleon form of the operator. In the β-decay context, quenching of the nuclear matrix element can be thought of as a renormalization of the decay of the free-nucleon. Degrees of freedom not included in the model space of the calculation require a correction to either the value of g_A/g_V or to the nuclear matrix element of $\hat{\vec{\sigma}}\hat{\tau}$ [76]. Different mechanisms have been proposed for quenching, such as higher-order nuclear configuration mixing (2p-2h and above) and couplings to nucleon degrees of freedom (the Δ isobar) [77, 76, 78]. These mechanism serve to push the missing strength to higher excitation energies. In charge-exchange experiments, a significant fraction of the missing strength has been observed at energies above the GT giant resonance. By measuring both the $\beta+$ and $\beta-$ directions with the ^{90}Zr(p,n) and ^{90}Zr(n,p) reactions, 88$\pm$6% of the sum-rule strength was observed. This was done by looking up to 50 MeV of excitation energy [79, 80, 81, 82].

The amount of quenching of GT strength has been studied in the p, sd, and pf shells by using β-decay information and comparing it to shell-model calculations. These results are summarized in Table 1.2. As mentioned in Section 1.8, the ^{16}C(p,n)^{16}N reaction will measure the strength in the $\beta-$ direction and give a measurement of the quenching of summed GT strength in an unstable neutron-rich nucleus. This value will be compared to the results in table 1.2.

Region	Quenching Factor
p-shell	1-0.19$\left(\frac{A}{16}\right)^{0.35}$ [77]
sd-shell	0.76 [76]
pf-shell	0.744 [83]

Table 1.2: Quenching factors of GT strength for nuclei occupying the p, sd and pf shells. The factors presented are the quenching of the GT operator. To find the quenching of GT strength, the factor must be squared, so in the sd shell it is $0.76^2 = 0.58$.

Chapter 2

Theoretical Techniques

I demand rigor

A foolish 1^{st} year graduate student

This chapter gives a brief overview of the theoretical tools used in the calculation of GT strength and charge-exchange cross section. It does not give a rigorous derivation of the theoretical framework, but instead focuses on the necessary ideas needed for charge-exchange studies. For a development of nuclear reaction formalism, the reader is referred to Ref. [84].

2.1 Distorted Wave Born Approximation

This section gives a brief overview of the distorted wave born approximation and its relevance to charge-exchange reactions. Here the aim is solve the time-independent Schödinger equation for the nuclear reaction problem,

$$\hat{H}\Psi = E\Psi. \tag{2.1}$$

In the asymptotic limit ($r \to \infty$), the wave function should take the following form,

$$\Psi = \Psi_{beam} + \Psi_{scatt} = C\left(e^{ik_i z} + f(\theta,\phi)\frac{e^{ik_f r}}{R}\right) \tag{2.2}$$

where $e^{ik_i z}$ represents the beam as an incoming plane wave and e^{ikf^r}/r is the outgoing spherical wave from the scattering. $f(\theta, \phi)$ is known as the *scattering amplitude*, which contains the scattering information of the reaction. The differential cross section is directly related to the scattering amplitude by,

$$\frac{d\sigma}{d\Omega} = |f(\theta, \phi)|^2. \tag{2.3}$$

In order to calculate the charge-exchange differential cross section, we need to find an expression for the scattering amplitude f. To do this we return to the Schrödinger equation but write it more explicitly as,

$$\left(-\frac{\hbar^2\nabla^2}{2\mu} + V\right)\Psi = \frac{\hbar^2 k^2}{2\mu}\Psi, \tag{2.4}$$

where E has been replaced by $E = \frac{\hbar^2 k^2}{2\mu}$ and the kinetic part of the Hamiltonian has been written explicitly. Rearranging this expression yields,

$$\left(\nabla^2 + k^2\right)\Psi(\vec{r}) = \frac{2\mu}{\hbar^2}V(\vec{r})\Psi(\vec{r}), \tag{2.5}$$

where the dependence on the spatial coordinate $\vec{r}$ has been included for clarity. This equation can be cast into the standard Green's function problem by setting $\hat{D} = \left(\nabla^2 + k^2\right)$ and $\rho = \frac{2\mu}{\hbar^2}V(\vec{r})\Psi(\vec{r})$ yielding,

$$\hat{D}\Psi = \rho. \tag{2.6}$$

This equation has the solution,

$$\Psi(\vec{r}) = \phi(\vec{r}) + \frac{2\mu}{\hbar^2}\int G_{\pm}(\vec{r},\vec{r}')V(\vec{r}')\Psi(\vec{r}')d\vec{r}' \tag{2.7}$$

where $G_{\pm}(\vec{r},\vec{r}')$ is the Green's function of the operator $\hat{D}$ and $\phi(\vec{r})$ is the solution to the homogeneous equation $\hat{D}\Psi = 0$. The $\pm$ notation in the Green's function refers to the post and prior forms of the solution. Both an incoming plane wave with outgoing spherical wave (prior form) and an outgoing plane wave with an incoming spherical wave (post form) satisfy the boundary conditions. In the calculations of the charge-exchange cross section, the prior form is used. It can be shown (see for example Ref. [84]) that the Green's function takes the form of,

$$G_{\pm}(\vec{r},\vec{r}') = -\frac{e^{\pm ik|\vec{r}-\vec{r}'|}}{4\pi|\vec{r}-\vec{r}'|}. \tag{2.8}$$

Substituting the Green's function into equation 2.7 and applying the approximation $|\vec{r}-\vec{r}'| = \sqrt{r^2+r'^2-2\vec{r}\cdot\vec{r}'} \approx r\sqrt{1-2\vec{r}\cdot\vec{r}'/r^2}$ we have,

$$\Psi(\vec{r})_{\pm} = \phi(\vec{r})_{\pm} - \frac{2\mu}{4\pi\hbar^2}\int \frac{e^{\pm ikr}}{r}e^{\mp i\vec{k}'\vec{r}'}V(\vec{r}')\Psi(\vec{r}')d\vec{r}' \tag{2.9}$$

$$\Psi(\vec{r})_{\pm} = \phi(\vec{r})_{\pm} - \frac{2\mu}{4\pi\hbar^2}\frac{e^{\pm ikr}}{r}\int e^{\mp i\vec{k}'\vec{r}'}V(\vec{r}')\Psi(\vec{r}')d\vec{r}'. \tag{2.10}$$

Comparing Equation 2.10 with Equation 2.2 the scattering amplitude can be identified as,

$$f(\vec{k},\vec{k}') = -\frac{2\mu}{4\pi\hbar^2}\int e^{\mp i\vec{k}'\vec{r}'}V(\vec{r}')\Psi(\vec{r}')d\vec{r}' \tag{2.11}$$

So far in the derivation there has only been the well constrained approximation that $r >> r'$.

However, the expression for the scattering amplitude in Equation 2.11 contains the total wave function, which is the unknown we started with. To arrive at a useful result, the Born Approximation is made where the form of the solution in Equation 2.10 is recursively inserted into Equation 2.11. This gives a series solution, where each term contains higher and higher orders of the potential V. Taking just the first term, we have,

$$f(\vec{k},\vec{k}') \approx -\frac{2\mu}{4\pi\hbar^2}\int e^{\mp i\vec{q}'\vec{r}'}V(\vec{r}')d\vec{r}', \tag{2.12}$$

where $\vec{q} = \vec{k} - \vec{k}'$ is the momentum transferred. This gives a clear and explicit way to calculate the scattering amplitude. This is the first order Plane Wave Born Approximation (PWBA). This result is often written in terms of the T matrix,

$$\begin{aligned} T &= \langle \phi \,|\, V \,|\, \Psi \rangle \\ T &\approx \langle \phi \,|\, V \,|\, \phi \rangle \,, \end{aligned} \tag{2.13}$$

where ϕ are plane waves.

To derive the Distorted Wave Born Approximation (DWBA), it is useful to rewrite Equation 2.10 in an operator form known as the *Lipmann-Schwinger equation*,

$$|\Psi_\pm\rangle = |\phi\rangle + G_\pm V\,|\Psi_\pm\rangle\,, \tag{2.14}$$

which, under the Born Approximation reduces to,

$$|\Psi_\pm\rangle = |\phi\rangle + G_\pm V\,|\phi_\pm\rangle\,. \tag{2.15}$$

In nuclear reactions, the potential is often divided into two parts, $V = U + W$, where U is the part of the potential that describes elastic scattering for the system while W contains the residual interaction that is not included in U. U is chosen such that,

$$|\chi\rangle = |\phi\rangle + G_{\pm}^{U} U |\phi\rangle \,, \tag{2.16}$$

where $|\chi\rangle$ is referred to as a distorted wave and $G_{\pm}^{U}$ is the Greens function for the problem containing only U. For charge-exchange calculations, W contains the interaction responsible for exciting the spin-isospin degrees of freedom in the target nucleus. The purpose of this separation becomes clear when you consider the total T matrix with these two potentials,

$$T = \langle \phi \,|\, W + U \,|\, \Psi \rangle \,. \tag{2.17}$$

For clarity, the full wave function is used in the above relation. It can be shown that,

$$T = \left\langle \phi^{-} \,\middle|\, U \,\middle|\, \chi^{+} \right\rangle + \left\langle \chi^{-} \,\middle|\, W \,\middle|\, \Psi \right\rangle \tag{2.18}$$

Since U only models the average potential of elastic scattering, it cannot connect the initial to the final states we are interested in for charge-exchange reactions. This leaves only the second term,

$$T = \left\langle \chi^{-} \,\middle|\, W \,\middle|\, \Psi \right\rangle , \tag{2.19}$$

where the effect of the U potential is incorporated into the determination of the distorted wave χ^{-}. Reapplying the Born Approximation, we arrive at the T matrix for first order

DWBA,

$$T^{DWBA} = \langle \chi^- \,|\, W \,|\, \chi^+ \rangle \tag{2.20}$$

So far the internal state of target and residual nucleus has been omitted from the derivation to focus on the details of the reaction theory. Equation 2.20 is rewritten in terms of a form factor $F(\vec{R})$,

$$T^{DWBA} = \left\langle \chi^- \,\middle|\, F(\vec{R}) \,\middle|\, \chi^+ \right\rangle, \tag{2.21}$$

where $\vec{R}$ is the spatial distance between the center of the target nucleus and the position of the incident probe. The form factor is,

$$F(\vec{R}) = \int dr_T dr_p \; \rho_p V_{eff} \rho_T, \tag{2.22}$$

where the residual interaction has been relabeled as V_{eff}. ρ are the transition densities of the target and projectile,

$$\rho = \sum_\alpha OBTD_\alpha \, \langle \phi_{f_\alpha} || \hat{\sigma} \hat{\tau}_\pm || \phi_{i_\alpha} \rangle \, . \tag{2.23}$$

The one-body transition densities (OBTD) are calculated in the shell model between the initial and final states. The sum over α runs over the contributions from the different 1p-1h combinations for single particle level transitions ϕ_{i_α} to ϕ_{f_α}. The single-particle wave functions are modeled with Woods-Saxon potentials. With the formalism above, the only remaining unknown is the form of the effective NN interaction that can meditate charge-exchange reactions.

2.2 Effective Interaction

In this section, the phenomenological nucleon-nucleon interaction that is used to model charge-exchange reactions is discussed (V_{eff}). The long-standing choice for interaction in the charge-exchange community has been the Love and Franey (LF) N-N interaction [85, 86]. The LF interaction is attractive for charge-exchange studies since it is directly parameterized in terms of the spin and isospin operators that are of interest for charge-exchange reactions. The potential between nucleons i and j is structured into central, spin-orbit, and tensor terms,

$$V_{ij} = V^C(r_{ij}) + V^{LS}(r_{ij})\vec{L}\cdot\vec{S} + V^T(r_{ij})S_{ij}, \tag{2.24}$$

where S_{ij} is the tensor operator

$$S_{ij} = 3\frac{(\hat{\sigma}_i \cdot r_{ij})(\hat{\sigma}_j \cdot r_{ij})}{r_{ij}^2} - \hat{\sigma}_i \cdot \hat{\sigma}_j \tag{2.25}$$

The radial dependence of each of these terms is expanded as a sum of Yukawa potentials,

$$V(r) = \sum_i V_i Y(r/R_i), \tag{2.26}$$

where $Y(x) = e^{-x}/x$. The parameters V_i and the ranges R_i are fit to nucleon-nucleon scattering. The result of the work by Love and Franey gave effective nucleon-nucleon T matrices at a variety of incident beam energies. For the ^{16}C(p,n)^{16}N at 100 MeV/u, the LF interaction at 140 MeV was used. The 140 MeV interaction was chosen over the 100 MeV interaction because the parameters were better determined from the nucleon-nucleon scattering data [85, 86]. The GT component of the interaction does not change significantly

between these energies. However, the magnitude of the τ component of the NN interaction reduces with increasing energy. This is corrected for by using Equation 2.31. The interaction is folded over the transition densities of the target and projectile to arrive at the form factor given in Equation 2.23.

2.3 Proportionality

This section provides a brief overview of proportionality between GT strength and charge-exchange cross section. The interested reader is referred to [56] for the complete derivation and a detailed discussion. Taddeucci et al. showed that the form of this relationship is a simple proportionality,

$$\left(\frac{d\sigma}{d\Omega}\right)_{q\to 0} = \hat{\sigma} B(GT), \tag{2.27}$$

where the $q \to 0$ indicates that the cross section needs to be extrapolated to zero linear momentum transfer. The $\hat{\sigma}$ is the proportionality constant of the expression and is called the unit cross section. Within DWBA and under the limits of high beam energy ($>\sim$100 MeV/u) and the Eikonal approximation, Taddeucci et al. showed that the unit cross section factors into three components,

$$\hat{\sigma} = K N_D |J_{\sigma\tau}|^2. \tag{2.28}$$

K is the kinematic factor,

$$\frac{E_i E_f}{(\hbar^2 c^2 \pi^2)^2} \frac{k_f}{k_i}. \tag{2.29}$$

N_D is a distortion factor and $J_{\sigma\tau}$ is a volume integral of the relevant interaction (in this case, the Love Franey interaction). N_D can be calculated as the ratio of distorted- and plane-wave cross sections (see Equation 2.23 of Ref. [56]).

While the factorization of the proportionality gives insight, the unit cross section is often determined empirically. When β-decay information for a low-lying state is available, $\hat{\sigma}$ can be found by using the known B(GT) value and the measured charge-exchange cross section. When such information is not available, the unit cross section can sometimes be estimated by looking at compiled dependencies between $\hat{\sigma}$ and mass number. Fig. 2.1 shows the mass dependence of the unit cross section over a range of nuclei for the (p,n) reaction at 120 MeV. The parameterization was determined by Taddeucci et al. [56].

The ratio of GT and Fermi unit cross sections was also investigated by Taddeucci et al. They defined,

$$R^2 = \frac{\hat{\sigma}_{GT}(E_p, A)}{\hat{\sigma}_F(E_p, A)} \tag{2.30}$$

The dependence of R^2 on incident energy and mass number was investigated experimentally by measuring R^2 for a set of targets at a variety of beam energies. A linear dependence on E_p was found,

$$R(E_p) = \frac{E_p}{55.0 \pm 0.4 \text{ MeV}}. \tag{2.31}$$

Fig. 2.2 shows this dependence for ^{14}C. The deviations below 50 MeV are below the incident energy region where the proportionality is applicable.

2.4 Technical Details of Calculations

The cross-section calculations for the ^{16}C(p,n)^{16}N reaction at 100 MeV/u were completed using the DW81 code [87] (see Ref. [88] for a description of the original formalism). The theoretical GT strengths and one-body transition densities were calculated using OXBASH [8] in the *spsdpf* model space using either the WBT or WBP interactions. The optical

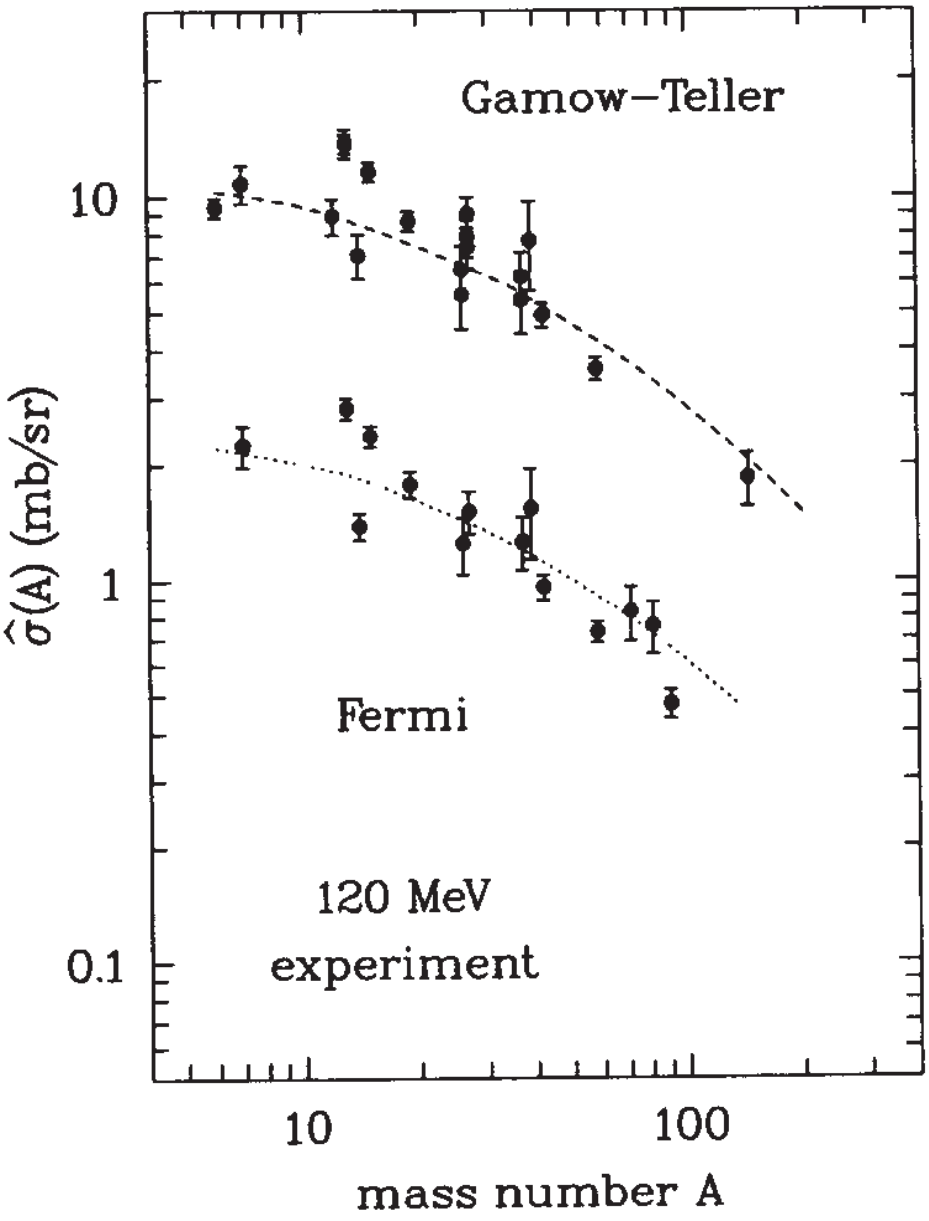

Figure 2.1: Experimental unit $\hat{\sigma}_{GT}$ and $\hat{\sigma}_F$ as a function of mass number. The dashed and dotted lines are the result of the parameterization of Taddeucci et al. Figure is reproduced from Ref. [56].

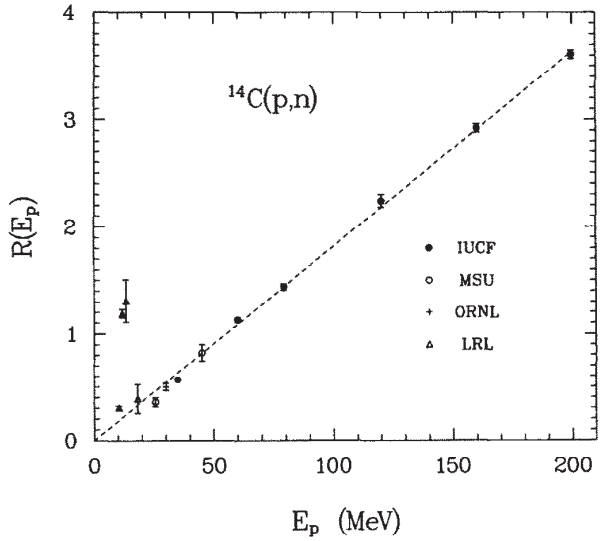

Figure 2.2: The square root of the ratio of the GT and Fermi unit cross sections as a function of incident proton energy. The data points come from reactions on ^{14}C at various energies. The dashed line is a linear fit to the data above 50 MeV. Figure taken from Ref. [56], see references therein.

potentials for the proton-^{16}C entrance channel and the neutron-^{16}N exit channel come from the parameterizations given in Refs. [89, 56]. The parameters used for the ^{16}C(p,n)^{16}N calculation are given in Table 2.1 for convenience. The LF interaction at 140 MeV was used for the N-N potential. The binding energies of the single-particle wave functions in the initial and final state were calculated using a Skyrme interaction.

Potential	V	r	a	W	r	a
p-V	30.68	1.23	0.71	7.12	1.41	0.57
p-SO	3.54	1.00	0.65	-1.07	0.97	0.62
n-V	25.16	1.23	0.71	7.12	1.41	0.57
n-SO	4.01	1.00	0.65	-1.07	0.97	0.62

Table 2.1: Parameters for the optical potentials used in the ^{16}C(p,n)^{16}N cross-section calculations. All parameters are given in MeV and Fermi. V refers to a volume term and SO a spin-orbit term. The volume terms are Woods-Saxon potentials. The spin-orbit terms are derivatives of Woods-Saxons. The p and n refer to the potentials for the proton (entrance) and neutron (exit) channels.

2.5 Shell Model Results

This section presents the results from the shell-model calculations performed with OXBASH. We start in the $\left|J^\pi = 0^+; T = 2\right\rangle$ ^{16}C ground state. In charge-exchange reactions ($\Delta T = 1$), the final state in ^{16}N can be $T_i = 2 \otimes \Delta T = 1 \rightarrow T_f = 1, 2, 3$. If T_i is high, transitions to higher T states are suppressed by their Clebsch-Gordan coefficients. For the ^{16}C(p,n)^{16}N reaction, these factors are given in Table 2.2.

T_f	Coefficient	Factor
T+1	$\frac{1}{(T+1)(2T+1)}$	0.11
T	$\frac{1}{T+1}$	0.33
T-1	$\frac{2T-1}{2T+1}$	1

Table 2.2: Isospin Clebsch-Gordan factors for the $T_i = 2 \rightarrow T_f = 1, 2, 3$ transitions. The factors give in column 3 are normalized to the $T - 1$ transition.

In terms of angular momentum, the important transitions are $J^\pi_f = 1^+$ (GT transitions), and $J^\pi_f = 0^-, 1^-, 2^-$ (dipole transitions). Fig. 2.3 shows the GT strength distributions

for $0+ \rightarrow 1+$ transitions calculated with OXBASH in the *spsdpf* model space, and the WBP and WBT interactions. Configurations in both the p and sd shells are included in the calculation. Transitions to $T = 1$ and $T = 2$ finals states are shown. Within this model space, the full strength of the sum rule is exhausted in the $\Delta T_z = -1$ direction (the $\Delta T_z = +1$ is Pauli blocked), so the sum of all calculated states is ~ 12[1]. The $T = 3$ states contribute < 0.002 to the total strength and are neglected. Both interactions predict the majority of the GT strength to be below approximately 12 MeV, with strong states near 10 MeV. The $T_f = 2$ strength is a small component appearing at higher energies. The shell model does not give intrinsic widths to these states, which since they occur above particle separation thresholds are expected to be several MeV wide.

Fig. 2.4 shows the more complicated case of spin-dipole transitions, calculated with the WBP interaction. Unlike the GT transitions, no simple proportionality between spin-dipole strength (B(SD)) and charge-exchange cross section has been established. The typical approach is to directly compare measured cross sections with theoretical cross section calculated in DWBA. Fig. 2.4 therefore shows the cross section value at the angle where it is maximized for each shell model state with $J^{\pi}_f = 0^-, 1^-, 2^-$. The excitation energy of the states are aligned such that the first 2^- state is at 0 MeV (the ground state of ^{16}N is 2^-). The shell model predicts a 0^- ground state with slightly lower energy ($\sim$300 keV), and so appears negative in Fig. 2.4. This difference is within the error of the calculation and below the resolution of the experiment. The shell model predicts several strong states at $\sim$5-10 MeV. Above $\sim$12 MeV, substantial strength comes form many states. The resonances is expected to extend above 20 MeV.

[1]For ^{16}C, the GT sum rule is: $3(N - Z) = 3(10 - 6) = 12$

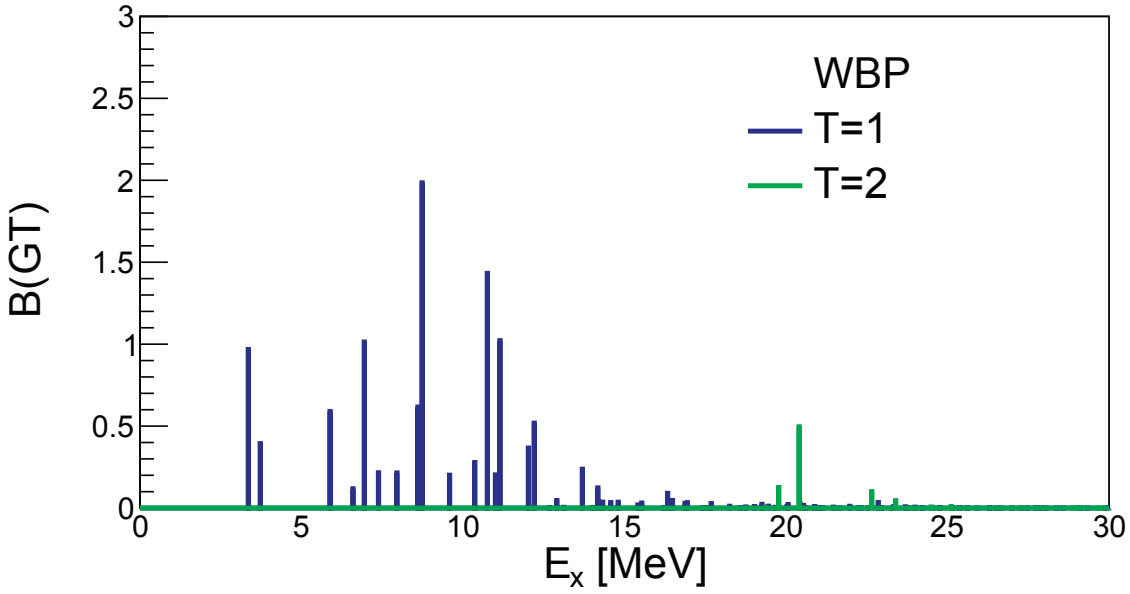

(a)

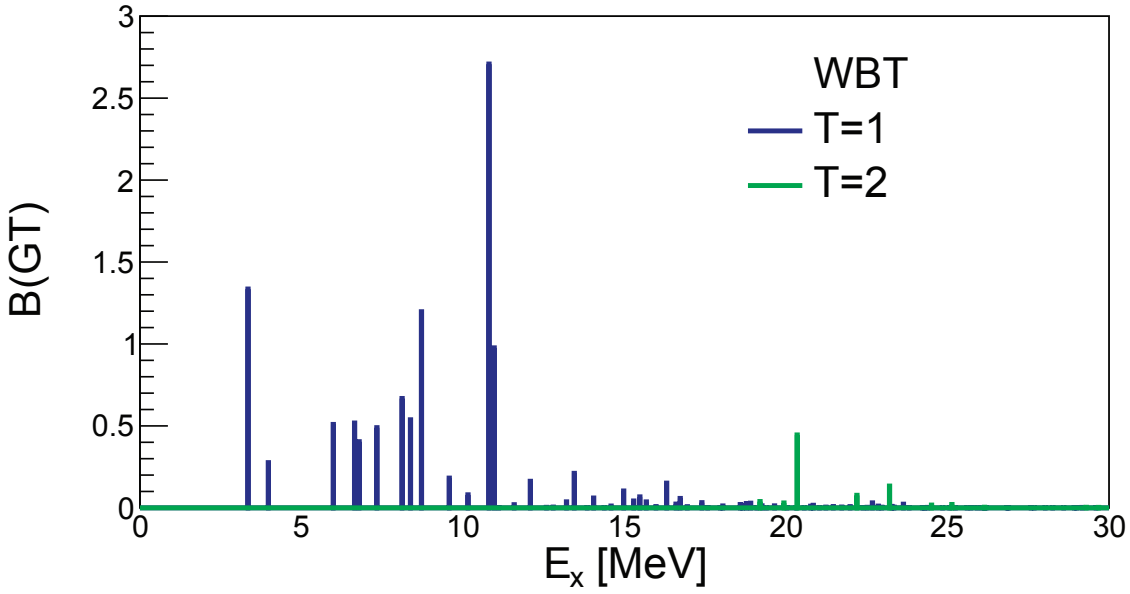

(b)

Figure 2.3: Shell Model calculations of B(GT) for $^{16}\mathrm{C}\big|0^+;T=2\big\rangle \rightarrow ^{16}\mathrm{N}\big|1^+;T=1,2\big\rangle$ transitions. The WBP (a) and WBT (b) interactions were used in the *spsdpf* model space.

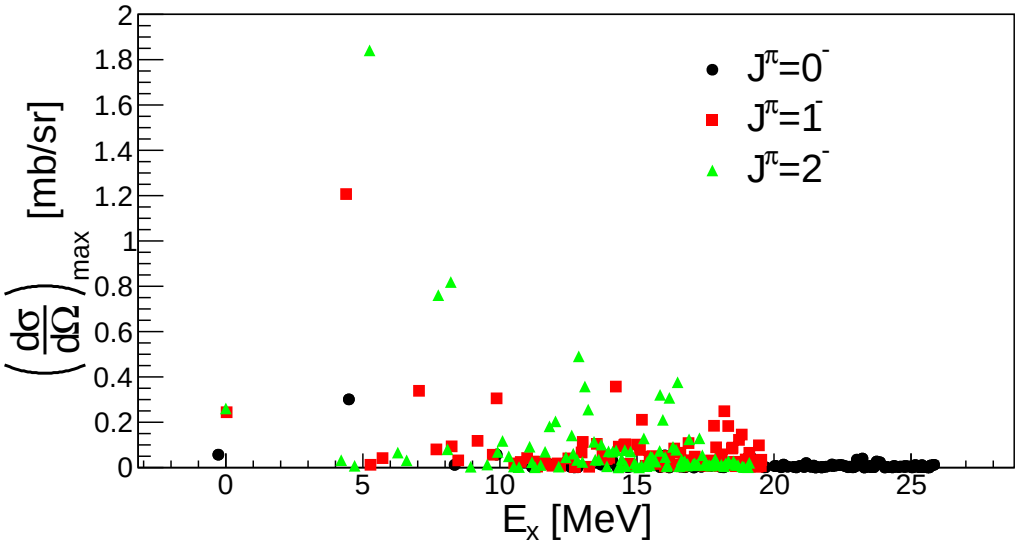

Figure 2.4: Shell-model spectrum with the WBP interaction for the SD strength in ^{16}N, presented as the peak cross-section value for each state. Transitions into final states of ^{16}N with $J^\pi_f = 0^-, 1^-, 2^-$ are shown. All states have $T = 1$.

2.6 DWBA Results

Within the shell-model and DWBA theory the proportionality between the charge-exchange cross section at vanishing momentum transfer and B(GT) can be explored. This is done by taking many shell-model states and calculating their differential cross sections at $q = 0$. Then, a theoretical proportionality constant ($\hat{\sigma}$) is found for each state by dividing the cross section by the B(GT) value from the shell model. This analysis is presented in Fig. 2.5

A consistent proportionality is seen for the stronger states, with a gradual decrease in quality for the weakest transitions. The spreading in the weaker states comes from the interplay between the $\sigma\tau$ and the tensor-τ portion of the effective NN interaction. The tensor-τ portion mediates ΔL=2 ΔS=1 transitions that interfere with the desired GT transitions (see Chapter 6 for more details). Since these proportionality breaking effects occur in weak transitions, they don't contribute much to the final GT spectrum. The scatter in the strong

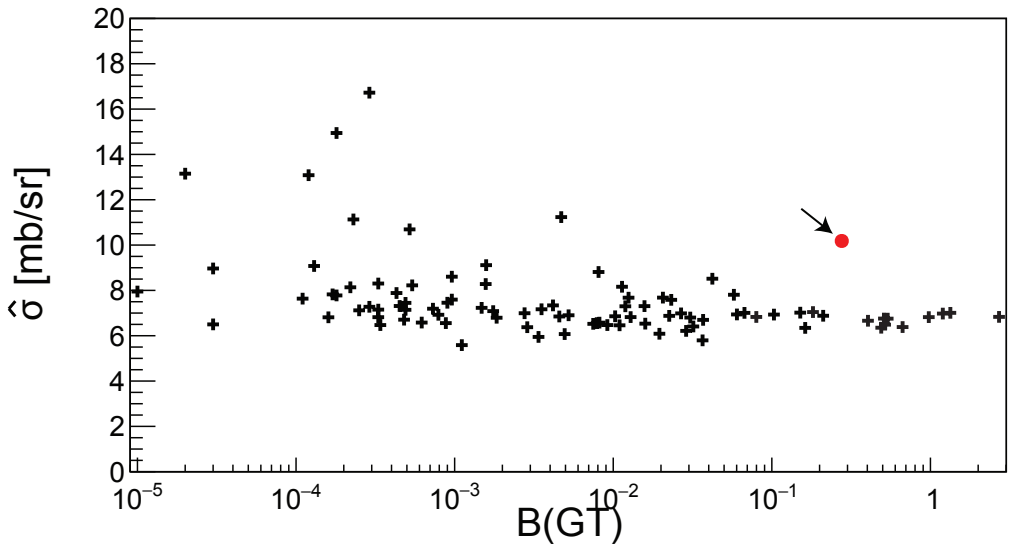

Figure 2.5: Scatter plot of the shell-model B(GT) for $0^+ \rightarrow 1^+$ transitions against the theoretical $\hat{\sigma}$ determined from DWBA. The shell-model calculation was done with the WBT interaction in the *spsdpf* model space. The red dot indicates the 2^{nd} shell-model state. In e10003 states with strengths below ~ 0.05 could not be discerned.

states tends to be evenly distributed giving the average $\hat{\sigma}_{GT}$ a small error. The red dot indicates the transition to the 2^{nd} 1^+ shell model state and is a clear outlier with a significantly higher predicted $\hat{\sigma}$. The detailed properties of this state will be discussed in Chapter 6.

In order to isolate the different orbital angular momentum transfers in the data, a multipole decomposition analysis (MDA) will have to be performed. Details on the procedure for the MDA is given in Section 5.2. Here the calculations of the characteristic angular distributions needed for the MDA are shown. Angular distributions with pure $\Delta L = 0$ $\Delta S = 1$ components from the $0^+ \rightarrow 1^+$ transitions were used as a model for the characteristic $\Delta L = 0$ angular distribution. The calculations to 1^- final states were used for the characteristic dipole angular distribution. Transitions to 2^+ final states were used for the quadrupole component. For each multipole, the first 100 shell-model states were examined with the Q value in the reaction calculation set to zero. From these angular distributions, a representative

strong state was chosen as the model for each ΔL transfer. The deviation between these states was small compared to the overall systematic error of the measurement. These model angular distributions are shown in Fig. 2.6.

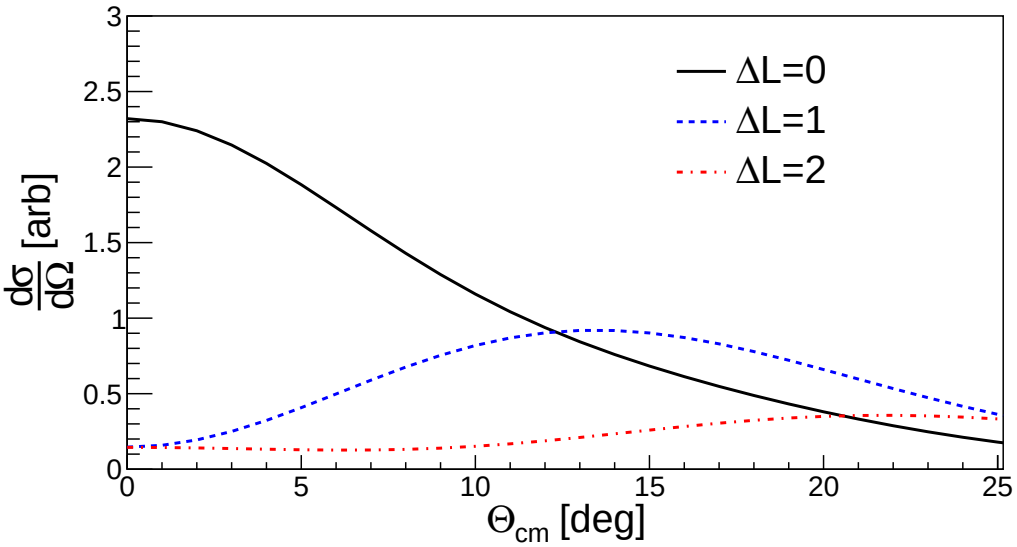

Figure 2.6: The model angular distributions for $\Delta L = 0, 1, 2$ that are used in the MDA analysis.

Chapter 3

Experiment

Nothing works! Everything is broken!

Ancient Proverb

The (p,n) charge-exchange experiment in inverse kinematics involves the detection of low-energy neutrons in coincidence with fast residues in a magnetic spectrometer. The neutron laboratory scattering angle and neutron kinetic energy provide event-by-event kinematic information necessary to reconstruct the excitation energy in ^{16}N and the center-of-mass (COM) scattering angle. For experiment e10003, the neutrons were detected using two low-energy neutron-detector arrays: LENDA [90, 91] and VANDLE [92, 93]. The fast residues of ^{16}N were detected by the S800 Spectrograph [94]. The experiment ran in March of 2015 with the goal of extracting the Gamow-Teller strength distribution up to 20 MeV of excitation energy in ^{16}N. Details on the experimental equipment and method will be given in the sections below.

3.1 Experimental Method

Fig. 3.1 shows kinematic correlations between the laboratory neutron kinetic energy and scattering angle, and the excitation energy in ^{16}N and COM scattering angle for the ^{16}C(p,n)^{16}N reaction at 100 MeV/u. As Fig. 3.1 shows, to cover the excitation energy regime of interest (0-20 MeV) and the COM scattering angles of interest (0-15 degrees), a large range of labo-

ratory neutron scattering angles and low neutron energy must be measured.

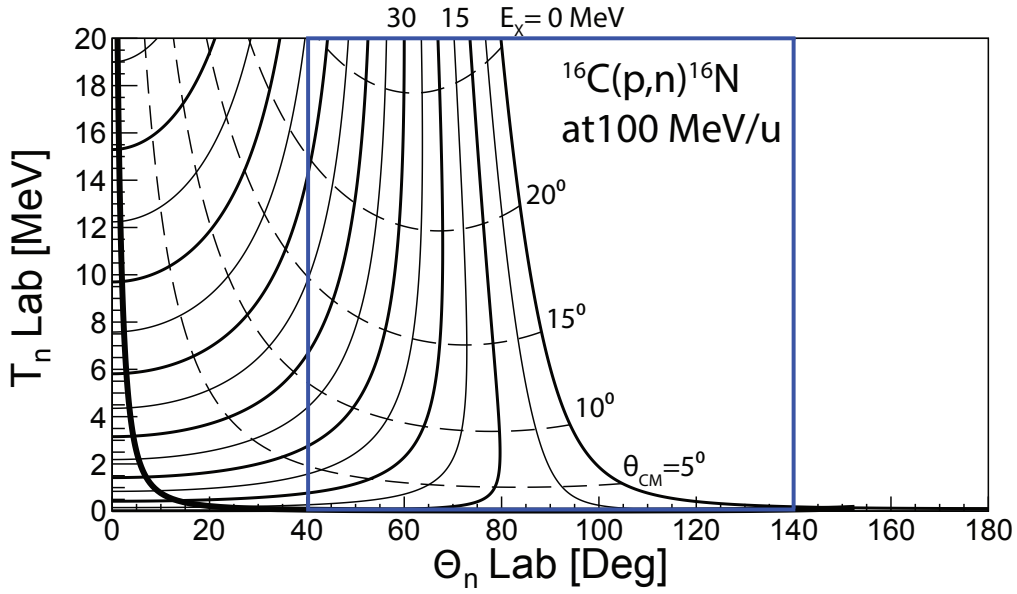

Figure 3.1: Kinematic correlations for the ^{16}C(p,n)^{16}N reaction at 100 MeV/u, in the plane of the laboratory neutron angle (θ_n) and neutron kinetic energy (T_n). The blue box indicates the approximate coverage of the neutron detectors in e10003. Solid lines indicate the excitation energies in ^{16}N. Dashed lines show the COM scattering angles.

To this end, the centers of the LENDA and VANDLE bars were placed 1 m from the center of the target so as to cover laboratory scattering angles between approximately 40 and 140 degrees. A schematic of the setup can seen in Fig 3.2. Each array was split in half and arranged such that one section of LENDA was placed on the opposite side of the beam line from the corresponding section of VANDLE. The angles of the bars were further arranged such that the gap in angular coverage between two LENDA bars was filled by the VANDLE bars on the opposite side of the beam line. The arrangements of different sections of LENDA and VANDLE allowed both arrays to span the full laboratory angular range being measured, while also preventing any systematic bias between the two arrays from differences in the neutron background on either side of the beam line. The choice to arrange the angles

of the bars to fill the angular gaps in the detectors on the opposite side of the beam line allowed for continuous laboratory angular coverage and reduced systematic uncertainties in the estimation of geometrical acceptance. This is because regions of near zero acceptance, where systematic uncertainties due to slight deviations in detector placement are large, were avoided. Fig. 3.3 shows a picture of the complete experimental setup.

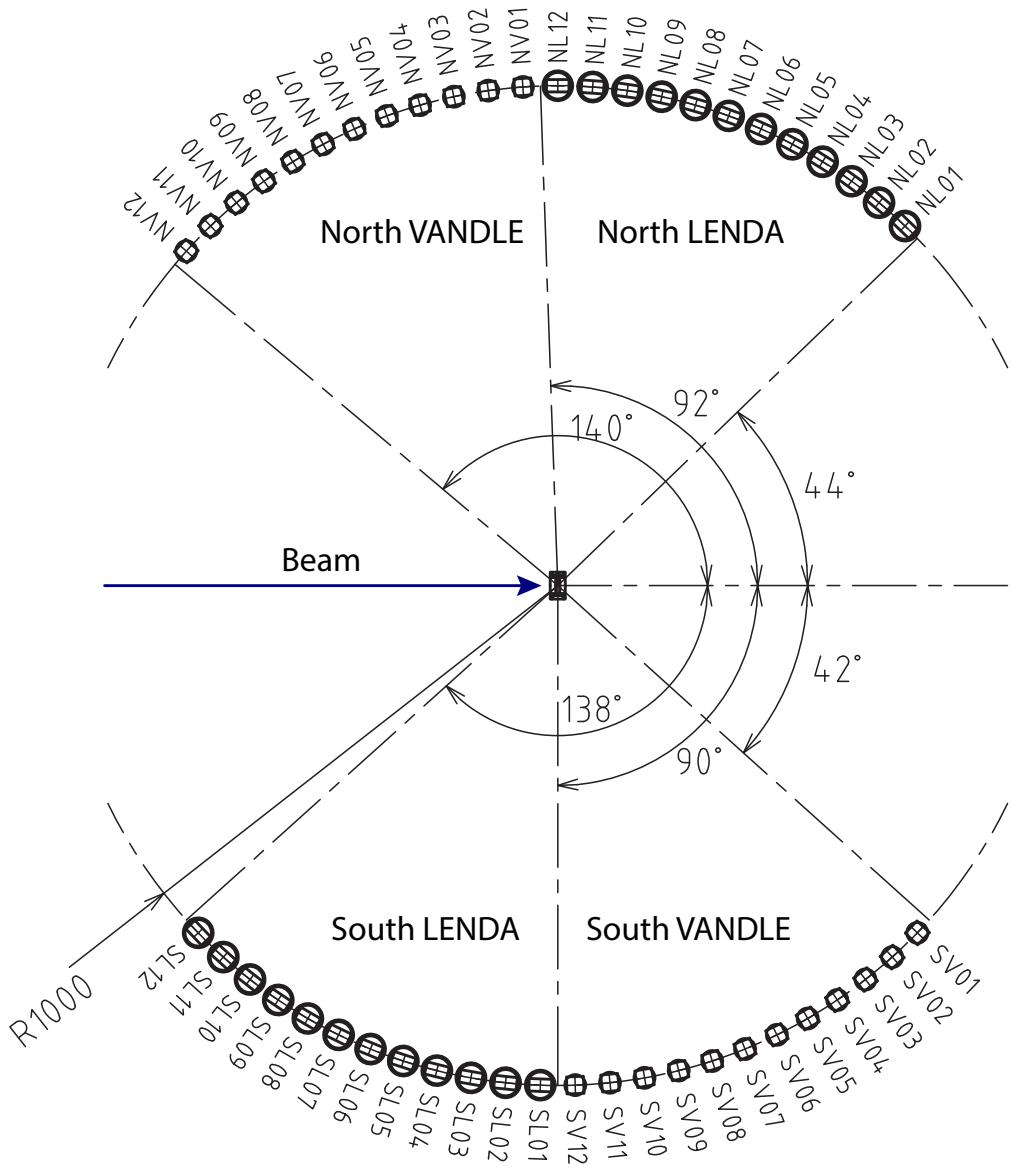

Figure 3.2: Top-view schematic of the experimental setup for the neutron detectors.

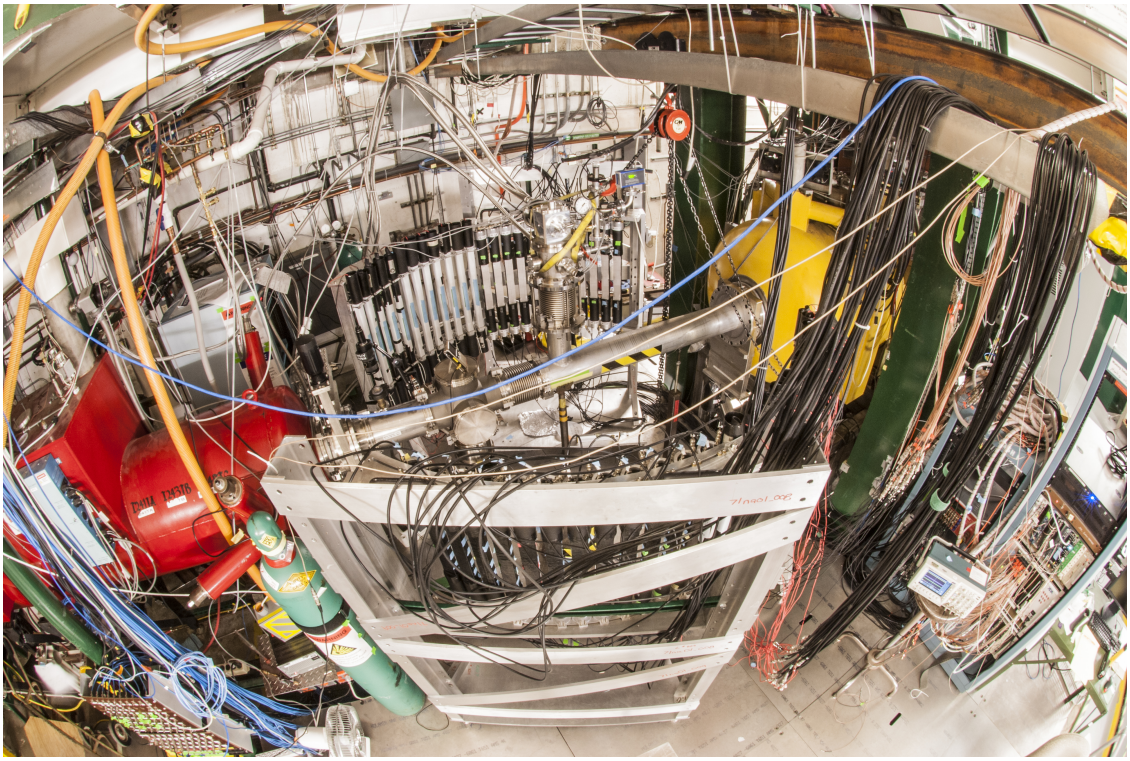

Figure 3.3: Picture of the complete setup for experiment e10003. In the bottom center of the picture, the south LENDA bars are visible. The north VANDLE bars can be seen in the top left. The liquid hydrogen target can be seen in the center of the photograph.

To isolate events that could be due to charge-exchange reactions, the ejectile was analyzed in the S800 Spectrograph. Since the experiment aimed to measure up to excitation energies of 20 MeV in ^{16}N, the 1n, 1p, 2n, 1p1n emission thresholds were exceeded. This caused several different nucleon decay channels to open (^{16}N, ^{15}N, ^{15}C, ^{14}C, ^{14}N), each of which needed to be measured to find the total charge-exchange cross section. The momentum spread of these residual ejectiles after the momentum kick from the decayed nucleons can be greater than the momentum acceptance of the S800 Spectrograph ($\frac{dp}{p} = 5\%$ [94]) . To account for this, seven different magnetic-rigidity settings were used to capture a large enough fraction of the momentum spectrum for each decay channel. The different decay channels and their associated rigidity settings used during the experiment are shown in Table 3.1.

E_x in ^{16}N	Reaction	Detected Particle	Set Centroid Rigidities
$0 \rightarrow 2.4$ MeV	^{16}C(p,n)^{16}N	^{16}N	3.2828, 3.338 Tm
>2.489 MeV	^{16}C(p,n)^{16}N $\rightarrow$ ^{15}N + n	^{15}N	2.98, 3.1325 Tm
>11.478 MeV	^{16}C(p,n)^{16}N $\rightarrow$ ^{15}C + p	^{15}C	3.52, 3.6565 Tm
>12.696 MeV	^{16}C(p,n)^{16}N $\rightarrow$ ^{14}C + p + n	^{14}C	3.2828, 3.38 Tm
>13.322 MeV	^{16}C(p,n)^{16}N $\rightarrow$ ^{14}N + n + n	^{14}N	2.98, 2.9 Tm

Table 3.1: Table of the different decay channels accessible in the ^{16}C(p,n)^{16}N reaction for ranges of excitation energy in ^{16}N and their associated magnetic rigidities. The acceptance of each rigidity setting is $\pm$ %5.

With the kinematic information provided by the low-energy recoiled neutron and the momentum information of the fast ejectile, the differential cross section could be reconstructed up to 20 MeV of excitation energy in ^{16}N.

3.2 Experimental Equipment

3.2.1 Beam Creation and Delivery

The ^{16}C(p,n)^{16}N reaction was performed with a beam of radioactive ^{16}C nuclei. Radioactive ion beams are created at the NSCL through the process of projectile fragmentation, where an accelerated stable ion beam is impinged on a thick ^{9}Be production target. The impinging ions are fragmented in flight by the target, creating a wide array of different residual isotopes, some of which are the unstable, exotic isotopes that are of interest for study. The specific isotopes of interest are then selected in flight by their magnetic rigidity using the A1900 fragment separator [95], possibly resulting in a nearly pure beam of the isotope of interest. This beam can be directed to one of several different experimental areas for study.

3.2.2 Ion Source

At the NSCL, there are two options for ion sources: the Superconducting Source for Ions (SuSI) [96, 97] and the Advanced Room TEMperature Ion Source (ARTEMIS) [98]. Both take a stable element and ionize it using the Electron Cyclotron Resonance (ECR) method. In the ECR method, a plasma is confined by a magnetic field while microwave power is applied at the electron cyclotron frequency,

$$\omega_c = \frac{eB}{m_e}, \tag{3.1}$$

where e is the electron charge, m_e is the electron mass, and B is the applied magnetic field strength. The particles are ionized by collisions with the moving electrons. The ions are then extracted and injected into the K500 cyclotron for acceleration. For e10003, the SuSI

source was used to produce $^{18}O^{3+}$ ions.

3.2.3 Cyclotrons

The coupled cyclotron facility at the NSCL [99, 100] houses two super-conducting cyclotrons, the K500 and the K1200, where the numeric designations refer to the maximum extraction energy achievable for protons. The cyclotrons accelerate charged ions by applying a strong radio-frequency (RF) electric field, while a magnetic field constrains the path of the particles to a circular orbit. Since the acceleration is more effective with higher charge states, a stripper foil designed to remove electrons from the ions is placed at the entrance to K1200. For light and medium-heavy nuclei, this allows for the creation of completely ionized beams. Fig. 3.4 shows a schematic of the two cyclotrons.

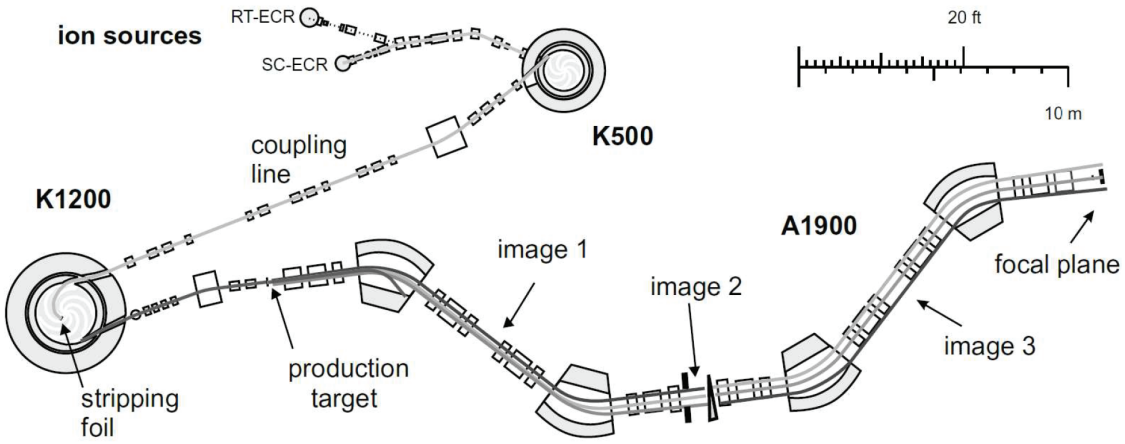

Figure 3.4: Schematic showing the coupled cyclotrons and the A1900 fragment separator. Figure taken from Ref. [95].

For e10003, the K500 cyclotron accelerated a beam of $^{18}O^{3+}$ ions to an energy of 10.91 MeV/u. These ions were extracted and sent through the stripper foil at the entrance to the K1200 cyclotron, where the completely ionized ^{18}O nuclei were further accelerated to 120 MeV/u. The beam was then impinged on a 846 mg/cm^2 target of ^{9}Be for fragmentation.

The resulting fragments then entered the A1900 fragment separator.

3.2.4 A1900

The A1900 fragment separator [95] consists of four dipole bending magnets and eight quadrupole triplet focusing magnets. The magnetic field of the dipole magnets serves to disperse the incoming particles according to their magnetic rigidity,

$$B\rho = p/q, \tag{3.2}$$

where B is the magnetic field, ρ is the bending radius, q is the charge and p is the relativistic momentum. Together, $B\rho$ is called the magnetic rigidity. Further selection is accomplished by placing a wedge at the intermediate image of the A1900 (see "image 2" in Fig. 3.4). The wedge causes species of different atomic numbers to lose different amounts of energy, allowing the particles to be separated by their new magnetic rigidities in the following two dipole magnets.

For e10003, the magnets were tuned to select ^{16}C. The slits at the first image of the separator were set such that the momentum acceptance was $\frac{dp}{p}$= 0.54%. An aluminum wedge of 240 mg/cm^2 was placed at the intermediate image of the A1900 to further remove contaminants. This resulted in a 97.8% pure beam of ^{16}C, with an intensity of $3.0 \cdot 10^4$ $\frac{\text{pps}}{\text{pnA } ^{18}0}$ as measured at the focal plane of the A1900. The largest remaining contaminant in the beam was ^{14}B.

3.2.5 S800 Spectrograph

Following the selection of ^{16}C in the A1900, the beam was transported through the transfer line to the S3 experimental vault. The S3 vault consists of the S3 analysis line and the S800 Spectrograph as can be seen in Fig. 3.5. The spectrograph has a momentum acceptance of 5% and covers a solid angle of 20 msr. The analysis line can operate at maximum rigidity of 4.9 Tm and is limited to 4 Tm for the spectrograph itself. Since the reconstruction of the excitation energy and COM scattering angle for the (p,n) reaction in inverse kinematics comes entirely from the measurement of the recoiled neutron, high resolution of the ejectile was not needed. Therefore, S800 beam line was operated in achromatic beam-transport mode.

The fast ejectile particles from the ^{16}C(p,n)^{16}N reaction were bent through the dipoles of the spectrograph into a series of focal-plane detectors. The purpose of the focal-plane detectors were to determine the hit position, angle, energy loss, and time-of-flight of the ions. From these parameters, the momentum, scattering angle, and particle identity (PID) can be determined. These focal-plane detectors are briefly described below.

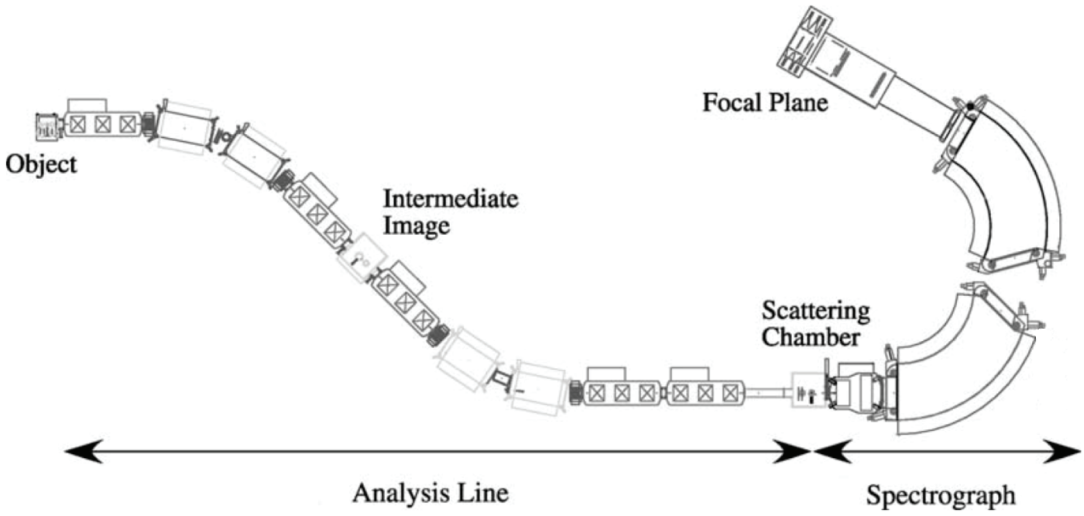

Figure 3.5: Schematic of the S800 analysis line and spectrometer. Figure adapted from [94].

3.2.6 Focal Plane Detectors

The first particle detectors at the S800 focal plane [101] are the Cathode Readout Drift Chambers (CRDCs). There are two CRDCs separated by 1073 mm allowing for two horizontal and vertical position measurements. Each CRDC is filled with a mixture of 20% isobutane and 80% carbon tetrafluoride. As the particle passes through the CRDCs, it ionizes the gas mixture, causing the freed electrons to drift towards an array of 224 cathode pads which lie along the dispersive (x) axis. As is illustrated in Fig. 3.6, the dispersive position can be determined by analyzing the image charge distribution on the pads. The non-dispersive (y) position is inferred from the drift time of the electrons in the detector. The drift time is determined from the difference between the S800 DAQ trigger time and the CRDC anode signal. Calibration details for the CRDCs are given in Chapter 4. From these two position measurements the dispersive and non-dispersive angles of the particle can be determined. This yields a total of four values: the dispersive position and angle (xfp and afp) and the non-dispersive position and angle (yfp and bfp).

After the CRDCs, the particle passes through an ion chamber filled with a gas mixture (90% argon and 10% methane), where the energy loss of the beam is measured. As in the CRDCs the particle ionizes the gas mixture, which causes electrons to drift to one of 16 anodes, where the charge is read out. The amount of energy lost in the ion chamber is proportional to the square of the charge of the particle as given in the Bethe-Bloch formula [103],

$$-\frac{dE}{dx} = \frac{4\pi e^4 Z^2}{m_0 v^2} n_{abs} z_{abs} \left(ln\frac{2m_0 v^2}{I} - ln\left(1 - \frac{v^2}{c^2}\right) - \frac{v^2}{c^2} \right), \tag{3.3}$$

where Z is the charge of the incident particle, n_{abs} and z_{abs} are the number density and atomic number of the absorbing material, m_0 is the electron's rest mass, I is the average ionization

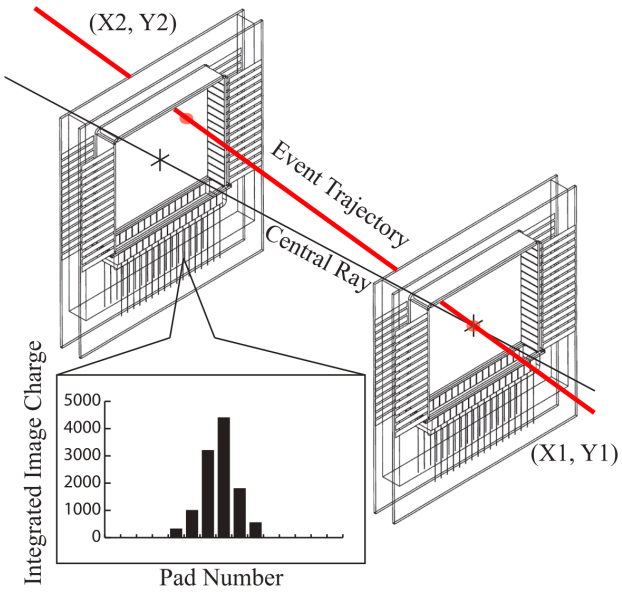

Figure 3.6: Schematic of the two cathode readout drift chambers, with an example event trajectory passing through the detectors. The inset shows an example of a charge distribution detected by the pads. Figure originally taken from Ref. [101] and modified by Ref. [102]

potential of the absorbing material respectively, and v is the velocity of the incident particle. Hence, by measuring the energy loss, the square of the atomic number can be determined after correcting for the difference in velocity across the focal plane.

The final detector at the S800 focal plane was a 5-mm thick plastic scintillator, referred to as the E1 scintillator. It serves as the trigger for the S800 data acquisition and gives time and energy readouts from the PMTs attached at each end of the detector. The E1 scintillator measures the TOF of the outgoing ejectiles in the ^{16}C(p,n)^{16}N reaction with reference to the object scintillator described below. The TOF from the object scintillator to the focal plane is proportional to the mass number of the ejectile and is used with the energy-loss measurement to determine the particle identification at the S800 focal plane.

The object scintillator is a thin plastic scintillator that is placed in the path of the beam in the object box of the S800 analysis line (see "object" in Fig. 3.5). For e10003, a 1127 μm

thick object scintillator was used. To ensure high-precision timing measurements could be made with these detectors and the neutron detectors, the signals from the object and focal plane scintillators were split and sent into both the S800 DAQ and the LENDA/VANDLE digital data acquisition system.

3.2.7 Liquid-Hydrogen Target

The reaction target in e10003 was the Ursinus liquid-hydrogen target. It had an average thickness of approximately 66 mg/cm^2 and a radius of 35 mm. The temperature was kept at approximately 19 K, at a pressure of just above 1 atm. Two 125 μm Kapton foils contain the liquid in the target. Fig. 3.7 shows the measured phase transition from gas to liquid, when the target was filled and cooled at the beginning of the experiment. The temperature and pressure were monitored throughout the experiment and any fluctuations of the density were corrected for on a run-by-run basis. Details on the target thickness determination are given in Section 4.5.3.

3.2.8 LENDA and VANDLE

The Low Energy Neutron Detector Array (LENDA) [90, 91] is an array of 24 BC-408 plastic scintillator bars built by the charge-exchange group at the NSCL. Each bar has dimensions of 4.5 x 2.5 x 30 cm. It is designed to measure the kinetic energy of neutrons via the time-of-flight method with kinetic energies from 100 keV-10 MeV and with a neutron kinetic-energy resolution of approximately 5%. A Hamamastu H6410 photomultiplier tube (PMT) is attached directly to each end of the LENDA bars to read out the scintillation light. At 1-m distance, the laboratory scattering-angular coverage of a LENDA bar is 2.58 degrees, and

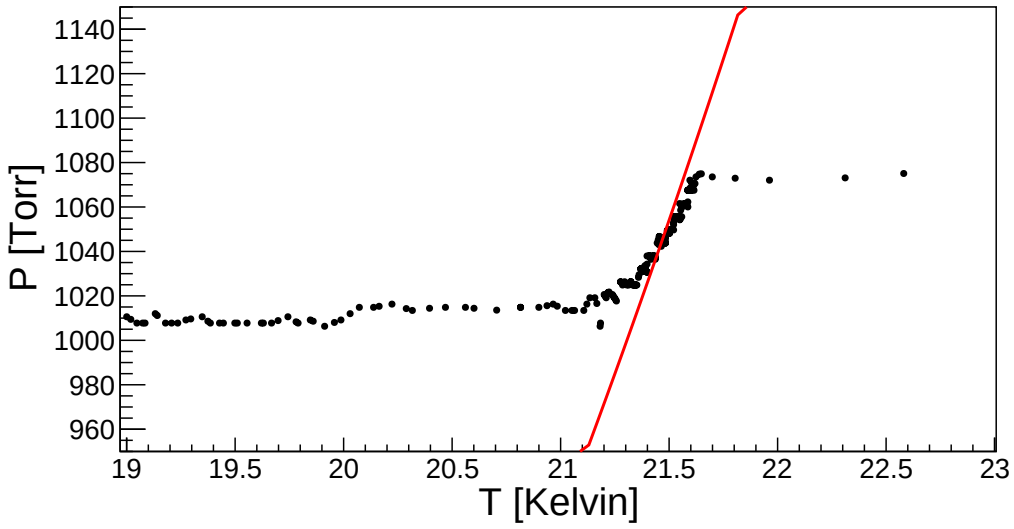

Figure 3.7: Pressure-temperature diagram for the liquid hydrogen target showing the phase transition from gas to liquid. The red line indicates the expected relationship taken from [104].

its vertical position resolution, determined from the time difference of the top and bottom PMTs, is 6 cm.

VANDLE, the Versatile Array of Neutron Detectors at Low Energy, is a similar set of neutron TOF detectors from the University of Tennessee [92, 93]. VANDLE is comprised of three different sized detectors, 3 x 3 x 60 cm (small) 3 x 6 x 120 cm (medium) and 5 x 5 x 200 cm (large), allowing different experimental layouts to be optimized to the energy resolution and range needed. For e10003, 24 of the small sized plastic scintillator bars were used. Similar to LENDA, VANDLE is able to measure low-energy neutrons with comparable energy resolution and detection efficiency. Both sets of detectors had the signals from each PMT sent into the Pixie DDAS System. Details about the digital system and the performance of LENDA are given in Section 3.3.

3.3 Digital Data Acquisition System

The data acquisition system (DAQ) for LENDA was upgraded prior to the running of this experiment in order to utilize a digital data acquisition system (DDAS). This upgrade effort was a significant portion of the work that makes up this thesis. Using a digital system allowed the VANDLE detectors to be easily integrated with the new DAQ, since adding more detectors only meant using more DDAS modules. The following sections give a brief overview of DDAS and describe the capabilities achieved for LENDA with DDAS.

3.3.1 DDAS Overview

The fundamental function of DDAS is to produce a digitized waveform, which is referred to as the trace. Each signal from the detector system is sent through a Nyquist filter and into a high-frequency analog to digital converter (ADC), where the analogue voltage is sampled to produce a digital waveform [105].

LENDA and VANDLE were instrumented with XIA's Digital Gamma Finder Pixie-16 boards [105]. For each of the 16 channels on the board, 250 megasamples per second (MSPS), 14-bit flash ADCs were used to perform the digitization of the incoming detector signals. After capturing the waveforms, 4 field-programmable gate arrays (FPGAs) implement on-board trace-processing routines to extract both time and energy information for each pulse. The Pixie-16 modules were placed in a PXI/PCI crate, which was controlled by a National Instruments MXI-4 crate controller connected with fiber-optic cable to a dedicated computer.

3.3.2 Digital Timing

Unlike an analog system, where timing and energy measurements are performed by two independent circuits, DDAS extracts this information simultaneously from the trace. This is accomplished for both time and energy through digital filtering algorithms, either on the board or in off-line analysis. For the 250-MSPS digitizers (a period of 4 ns between clock ticks) used in e10003, some form of interpolation scheme is needed to achieve timing resolution below the sampling frequency. This can be accomplished by selecting an appropriate function for the detector signal of interest and fitting that function to the waveform to extract a sub-clock tick time for each pulse. Prior to e10003, this method was successfully implemented for VANDLE where a detector-limited timing resolution of 0.6 ns was achieved over the full energy range using the fit function,

$$f(t) = \alpha e^{-(t-\phi)/\beta}(1 - e^{-(t-\phi)^4/\gamma}). \tag{3.4}$$

With the highest energy signals, a timing resolution of 0.5 ns was achieved [92]. The fitting method requires significant computational post processing and the creation of a library of appropriate functions for each detector signal. An alternate choice—and the one that was utilized in e10003 for both LENDA and VANDLE—is to use a digital constant fraction discriminator (CFD) algorithm similar to the one implemented on the Pixie boards [105, 106]. Higher-order interpolations of the CFD are done off line in software that are unavailable on the board. The implementation for this work is as follows. The trace is processed through

a symmetric trapezoidal filter,

$$FF[i] = \sum_{j=i-(T_r-1)}^{i} Tr[j] - \sum_{j=i-(2T_r+T_g-1)}^{i-(T_r+T_g)} Tr[j] \tag{3.5}$$

where T_r is referred to as the rise time, T_g the gap time and Tr the trace points. The filtered trace is used to form a digital CFD,

$$CFD[i+D] = FF[i+D] - w\ FF[i] \tag{3.6}$$

where D is a user specified delay and w is a scaling factor [105, 107]. The units of T_r, T_g, and D are in clock ticks and w is a unitless scaling factor. The sub clock-tick timing information is then determined from a linear interpolation of the CFD's zero crossing (this technique will be referred to as the *Linear Algorithm*). In Fig. 3.8, an example of this procedure is shown. The filled circles are a trace for a gamma ray from a ^{22}Na source generated by one photo multiplier tube (PMT) of a LENDA bar. The filled squares are its corresponding CFD signal with filter parameters $T_r = 6$, $T_g = 2$, $D = 4$, $w = 5/8$.

3.3.3 Intrinsic Timing Resolution of DDAS

One of the significant challenges for high-precision timing with DDAS is the occurrence of non-linearities in the system's response to fast scintillator pulses [92, 106]. This behavior makes it difficult to rely on a simple linear interpolation of the CFD's zero crossing. This non-linearity is maximized when the arrival time of a signal places its zero crossing in between two clock ticks, which for the 250 MHz digitizers used here is a time difference of 2 ns. To explore this behavior for LENDA, a ^{22}Na source was placed on a LENDA bar where the

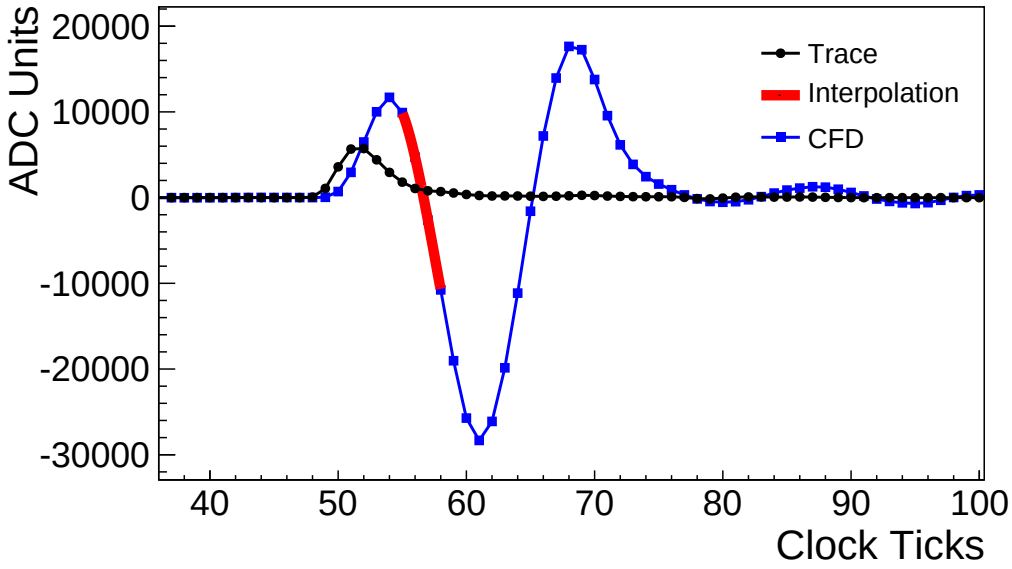

Figure 3.8: Example of digital trace from LENDA (filled circles) with overlaid digital CFD (filled squares). The thick line is the third-order interpolation function calculated for this event.

signal from one PMT of the bar was split into DDAS with a 2 ns delay added to one copy of the signal. Signals from both the 511 and 1275 keV gamma rays from ^{22}Na were used in the following analysis. The CFD algorithm described above was performed on each signal with the filter set $T_r = 2$, $T_g = 0$, $D = 4$, and $w = 1/8$. This parameter set corresponds to the optimum choice for the *Cubic Algorithm* (described below) and is one example of the linear-interpolation algorithm failing in the presence of a non-linear CFD signal. Figure 3.9 shows the time difference between these two signals after correcting for the dependence of the time difference on signal amplitude (a phenomenon known as "walk"). The walk correction was done by plotting the pulse height against the time difference and correcting for any observed correlation of the time difference on the pulse height. The pulse heights in this data set ranged from approximately 4% to 58% of maximum ADC value. The linear interpolation with the above parameter set (labeled in the plot as "Unoptimized Linear")

introduces systematic biases and fails to achieve good timing resolution.

However, the shape of the digital CFD signal in the neighborhood of the zero crossing is a function of the CFD filter parameters. By performing an optimization of those parameters, significant improvement can be achieved in the performance of the linear-interpolation method. As the parameters for the CFD algorithm are discrete, a brute-force approach was used for the optimization. Each trace in the data was processed with every possible filter combination in the ranges $T_r = 1 - 8$, $T_g = 0 - 3$, $D = 1 - 8$, $w = 1/8 - 7/8$ (T_r, T_g, D were limited to integer values, while w was limited to steps of 1/8). The parameter set that achieved the best resolution was taken as the optimum set. The result of that optimization ($T_r = 6$, $T_g = 2$, $D = 4$, and $w = 5/8$) is shown in Fig. 3.9, where it is labeled as "Optimized Linear." Significant improvement is made in the linear method after the optimization, but as Fig. 3.9 shows, there is still some systematic bias in the distribution.

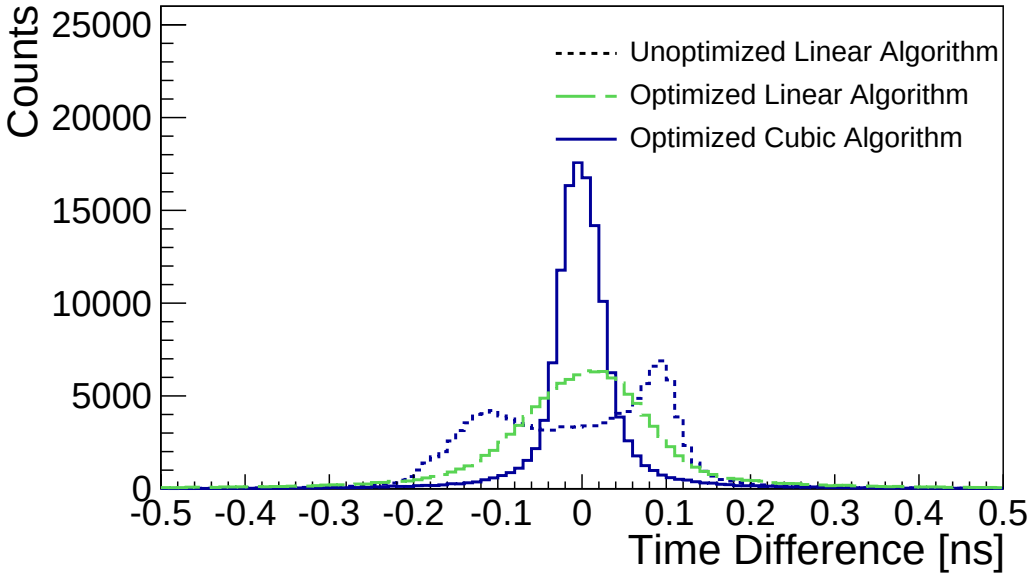

Figure 3.9: Time-difference spectra from a split-signal electronics test. The time differences from the 3 different timing algorithms have been shifted to zero for comparison.

Further improvements can be made through the use of a higher-order interpolation of the

CFD signal's zero crossing. Here the two points before the zero crossing and the two points after are used to calculate a third-order polynomial interpolating function. An example of this is shown in Fig. 3.8 as a thick red line. Given the clock ticks and corresponding ADC values, the coefficient for the interpolating function are found by inverting the following equation,

$$\begin{bmatrix} (x_1)^3 & (x_1)^2 & (x_1)^1 & (x_1)^0 \\ (x_2)^3 & (x_2)^2 & (x_2)^1 & (x_2)^0 \\ (x_3)^3 & (x_3)^2 & (x_3)^1 & (x_3)^0 \\ (x_4)^3 & (x_4)^2 & (x_4)^1 & (x_4)^0 \end{bmatrix} \begin{bmatrix} c_3 \\ c_2 \\ c_1 \\ c_0 \end{bmatrix} = \begin{bmatrix} y_1 \\ y_2 \\ y_3 \\ y_4 \end{bmatrix} \tag{3.7}$$

where $x_{1,2}$ and $y_{1,2}$ are the two points before the zero crossing and $x_{3,4}$ and $y_{3,4}$ are the two points after. The same optimization procedure as described above was used for this method (referred to as the *Cubic Algorithm*). The result of this optimization ($T_r = 2$, $T_g = 0$, $D = 4$, and $w = 1/8$) applied to the same data set as above is also shown in Fig. 3.9, labeled as "Optimized Cubic." It is clear that the resolution has improved substantially using the cubic interpolation scheme and any systematic biases in the time difference spectrum have been removed.

The intrinsic resolution results using the four points and a third-order polynomial were much better than the expected resolution of the detector (∼420 ps) Therefore, higher-order or more complicated interpolating schemes were not pursued.

Fig. 3.10 shows the full-width at half-maximum (FWHM) electronic timing resolution of DDAS from the same data shown in Fig. 3.9. The width of the time difference distribution is plotted as a function of pulse height for both the optimized cubic- and linear-interpolation algorithms. Figure 3.10 shows that the *Cubic Algorithm* performs significantly better at low pulse amplitudes, while both techniques provide electronic resolution well below the expected

performance of a LENDA bar at an appreciable fraction of the ADCs range.

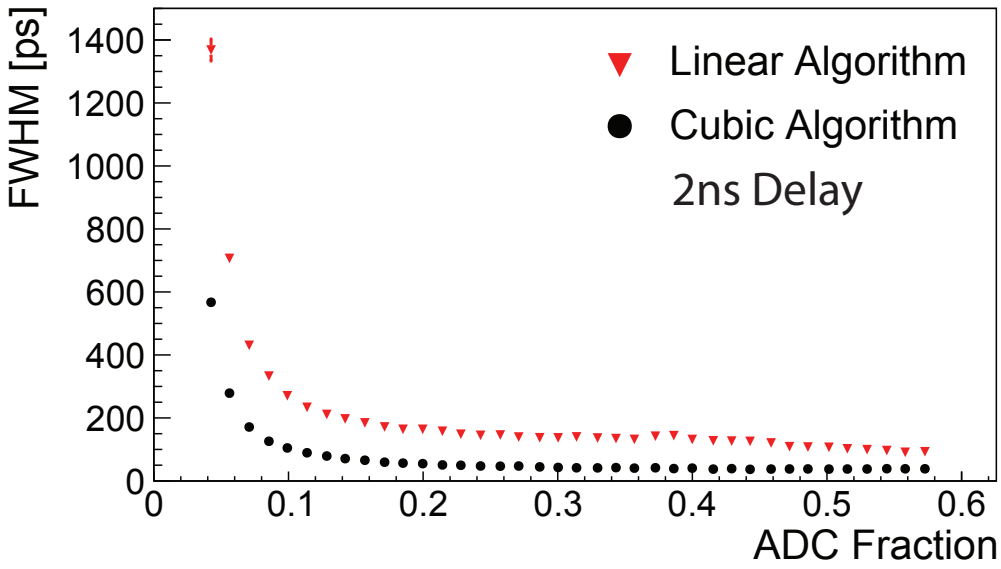

Figure 3.10: Electronic timing resolution of DDAS as measured with a split signal from a LENDA bar. The upside down triangles utilize a linear-interpolation method while the filled circles use a cubic-interpolation method. See text for details.

3.3.4 Timing Resolution of LENDA with DDAS

The timing resolution of LENDA with DDAS was measured using the two correlated 511 keV gamma rays generated after the positron decay of ^{22}Na. Two LENDA bars were placed on opposing sides of the ^{22}Na source at a distance of 1 m. Events were recorded in a 4-way coincidence between the PMTs of the two bars. The time difference between the two bars was calculated as:

$$T_{\text{diff}} = \frac{1}{2}(T_{1,\text{top}} + T_{1,\text{bottom}}) - \frac{1}{2}(T_{2,\text{top}} + T_{2,\text{bottom}}) \tag{3.8}$$

where the numerical subscripts refer to bar 1 and bar 2. The width of the T_{diff} distribution, corrected for walk and divided by $\sqrt{2}$, is taken as the timing resolution of a single LENDA

bar. In the same way described above, the parameters for this data set were optimized for the best resolution, yielding $T_r = 2$, $T_g = 2$, $D = 4$, and $w = 1/8$ for the linear algorithm and $T_r = 2$, $T_g = 0$, $D = 2$, and $w = 1/8$ for the cubic algorithm. Fig. 3.11 shows the measured timing resolution in FWHM of one LENDA bar as a function of pulse amplitude and energy in keVee for the linear and cubic timing algorithms discussed above. Unlike the data presented in Section 3.3.3, the signals in this measurement arrive randomly across all time differences, instead of always at a time difference of 2 ns. Because of the intrinsic resolution of the detector, the difference in achieved resolution between the cubic and linear algorithms is less than above. However, an improvement when using the cubic algorithm is still achieved, reaching about 400 ps at the highest energies. The saturation of the resolution at approximately 400 ps is a result of the intrinsic properties of the detector, and is not from the electronics.

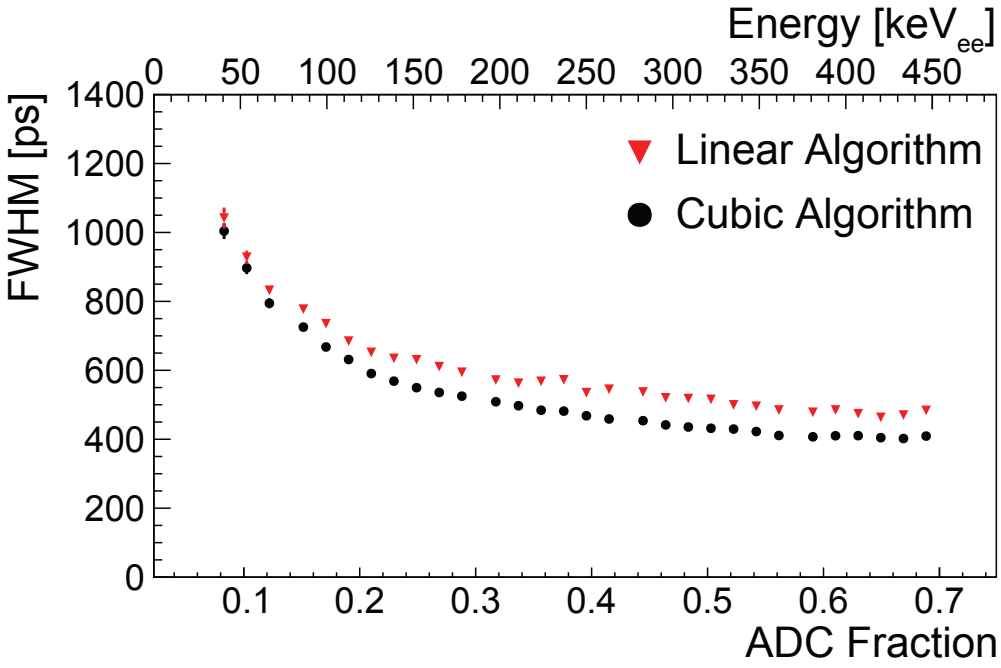

Figure 3.11: Measured timing resolution for LENDA readout with DDAS. Upside down triangles use a linear-interpolation method, while the filled circles use a cubic-interpolation method.

3.3.5 Energy Extraction Methods

There are many algorithms for extracting energy from digitized data, especially for high-precision spectroscopy (for example, see Ref. [108]). In the case of a plastic scintillator array, where signal-amplitude resolution is expected to be limited, relatively straightforward methods can be utilized. With the waveform saved, the energy of the event can be easily determined from the maximum trace value or, as is done for the e10003 analysis, by integrating the digitized pulse. In Fig. 3.12, a trace from one PMT in LENDA is shown, taken with a ^{22}Na source. The beginning 24 clock ticks of the trace is used to determine the average baseline of the signal, while a window around the maximum point in the trace is used to find the pulse's amplitude.

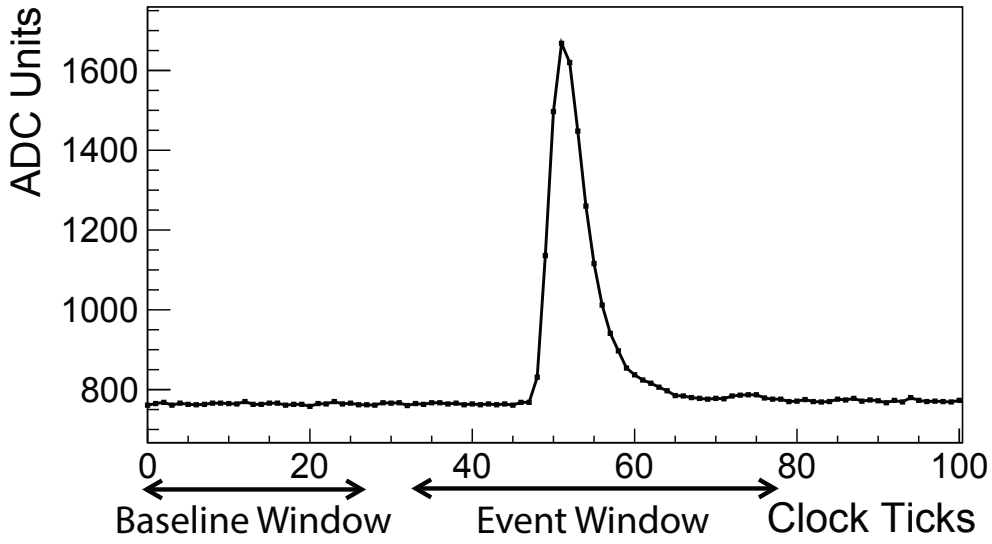

Figure 3.12: A trace from a PMT of LENDA from a ^{22}Na source. The first integration region is used to determine the average baseline of the signal, while the second integrates the pulse and determines the energy of the event.

To determine the resolution, an energy spectrum for ^{22}Na was measured using a LENDA bar. The source was placed in the center of the bar, and the energy of the event was taken

as the geometric average of the top and bottom PMT's pulse integration values,

$$E_{Bar} = \sqrt{E_T E_B}. \tag{3.9}$$

The top panel in Fig. 3.13 shows the calibrated energy spectrum in keVee obtained from this measurement. The two Compton edges from the 511 keV and 1274.5 keV gamma rays are seen at 341 and 1062 keVee, respectively. The Klein-Nishina formula convolved with a Gaussian [109] was used to fit the two Compton edges in order to extract a FWHM resolution of 23.5% at 341 keVee and 16% at 1062 keVee. Further, it was found that the position of the Compton edge was at 63.2 $\pm$ 1.9 % of the maximum yield of the Compton spectrum, where the error was determined from the fitting of the Compton edges.

The bottom panel in Fig. 3.13 shows an energy spectrum from a similar measurement using a ^{241}Am source. Here, the photo peaks from the low-energy x-rays at 26.3 and 59.5 keVee can be seen. The photo peaks were fit with Gaussians to obtain a FWHM energy resolution of approximately 42.3%.

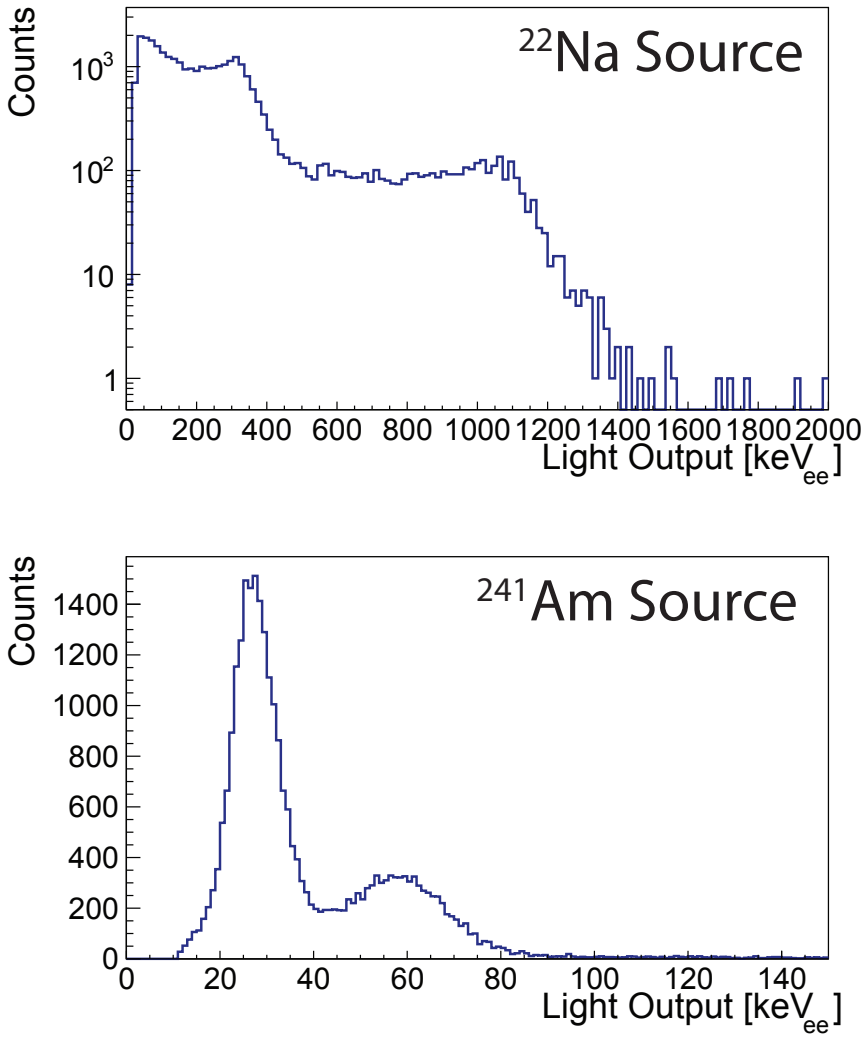

Figure 3.13: Top panel shows a calibrated energy spectrum from ^{22}Na seen in a LENDA bar. Bottom panel shows a calibrated energy spectrum from a ^{241}Am source.

3.3.6 KeVee to T_n

The correspondence between keVee and neutron kinetic energy in keV can be measured using a ^{252}Cf fission source. This measurement was performed with an EJ-301 liquid scintillator placed next to the ^{252}CF source, which was positioned 1 m from a LENDA bar. The liquid scintillator served as the start signal for a neutron time-of-flight (TOF) measurement with the LENDA bar, where a 3-way coincidence between the two PMTs of the LENDA bar and the PMT of the liquid scintillator was required. Fig. 3.14 shows a result of this measurement, where light output in keVee from neutrons in LENDA versus their kinetic energy determined from time-of-flight is presented.

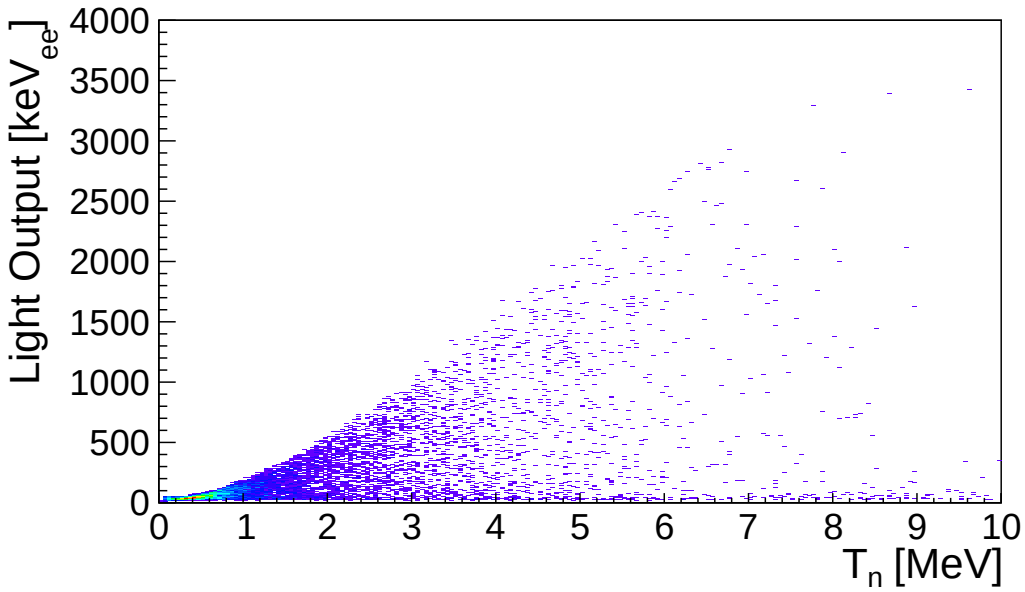

Figure 3.14: Scatter plot of light output against neutron energy from a ^{252}Cf source measured with LENDA and a EJ-301 liquid scintillator as the timing reference. The cuts on maximum light output are applied in this figure.

For high neutron energies (>3 MeV), the relationship between maximum light output (full energy of the neutron deposited in the bar) and kinetic energy is linear. The relationship

approximately follows,

$$L_{max}(E) = 518.1\ T_n - 499.5, \quad T_n > 3\ \text{MeV} \tag{3.10a}$$

where $L_{max}(E)$ is the maximum light output in keVee and T_n is the kinetic energy of the neutron in MeV. This relationship is non-linear at low neutron energies where it follows,

$$L_{max}(E) = 18.53 + 95.08\ T_n + 81.58\ T_n^2, \quad T_n < 3\ \text{MeV}. \tag{3.10b}$$

To remove background events, cuts on the light output of the neutron detectors following equations 3.10a and 3.10b were made in the analysis of e10003.

3.4 Implementation with the S800

Confident with the internal performance of DDAS, both LENDA and VANDLE were instrumented with the Pixie-16 250 MSPS modules for e10003. This section will discuss how the clock synchronization between the two systems was achieved and provide some details of the coincident trigger logic.

3.4.1 Clock Synchronization

A 50 MHz clock was taken from the backplane of the DDAS crate, downscaled to 12.5 MHz and sent into a JTEC XLM72 module in the VME crate of the S800's DAQ. Since this clock was from the backplane of the crate, it was a down-scaled version of the internal fast ADC clocks that perform the digitization of the detector signals and assign the events' time stamps. To achieve the synchronization two specialized DDAS modules were used. The first

was inserted in the front of the crate and served as a breakout module for the clock. It is shown in the bottom of Fig. 3.15, labeled as *clock breakout module*. The second was a clock extraction module connected to the backplane of the crate behind slot 2. Slot 2 contained the master Pixie module, which distributed the clock to other Pixie modules over the backplane. The clock extraction module connected to the *clock breakout module* with a Cat5 cable, as indicated in Fig. 3.15.

For each event, the scaler from the clock signal was latched and readout into the S800 data stream, allowing for a common time stamp between the two systems at a granularity of 12.5 MHz (80 ns intervals). This level of synchronization is only used for event correlation between the two systems, so it does not need the precision timing resolution achieved for the neutron TOF. Prior to the experiment, the setup was tested for stability and was found to remain synchronized for greater than 12 hours.

Under the firmware available at the time of the e10003 (March 2015), the internal clocks of each channel would pick up a random 1 clock tick phase each time they were reset (the default of the readout system at the beginning of each run). Further, reseting the clocks in DDAS would mean that the clock in the S800 would have to be cleared and the two systems synchronized again. These issues motivated finding a way to reset these clocks as infrequently as possible. As will be discussed in Section 3.4.2, this complicated the setup.

3.4.2 Operation Infinity Clock

The goal of Operation Infinity Clock was to allow the internal clocks of each DDAS channel to count continuously during the whole length of the experiment, without a reset at the beginning of each run. To achieve this, the DDAS readout program was edited such that the firmware call to reset the modules was only called once when the first run was started. The

S800 DAQ software was also modified to allow the scaler which keeps track of the DDAS clock, to remain uncleared between runs. Therefore, the clocks had to be reset only once at the beginning of the experiment and any time the DAQ crashed (which unfortunately occurred several times, requiring new timing offsets to be calculated for every channel).

When the DDAS system was reset, it would take approximately 10 seconds before the clocks were cleared and the system entered a running state. During this time, it was necessary to ensure that the S800 system did not receive any triggers or clock cycles, so that only when the DDAS system reset would the S800 begin processing timestamps and events. This was accomplished using a specialized module that output a constant signal when DDAS was in a running state. This module is labeled "*DDAS State Module*" in the diagram show in Fig. 3.15. This module was connected to the master DDAS module in slot 2 of the crate by a cat5 cable. This signal was used as a veto for:

1. The clock signal from DDAS (which is output continuously)
2. The LENDA/VANDLE master trigger to the S800
3. The S800 DAQ

When starting the first run, the veto of the clock was necessary since the S800 could not start counting the clock signals until DDAS reset its internal clocks and switched to a running state. The veto of the LENDA triggers and the S800 DAQ were necessary to ensure that no events happened in the S800 DAQ before the clock signal was ready. Reseting the two systems in this way synchronized the clocks and ensured that no events were triggered until both systems were ready.

However, since the clocks needed to be free running after they were synchronized in the first run, the veto for the clock signal needed to be removed during the first run. This way,

the veto is not reapplied when the DDAS system stops taking data at the end of the run, and the two systems remain synchronized. To accomplish this, the veto cable for the clock was patched to the data-U and then back down to the experimental setup. This way, during the first run, the cable could be unplugged, thereby sending the clock signal to the S800 DAQ regardless of what state the DDAS crate was in. Experimental shift takers were given detailed instructions about the role of this "magic veto cable" to ensure the clock remained synchronized during the experiment.

3.4.3 Trigger Logic

In order to select charge-exchange events from the ^{16}C(p,n)^{16}N reaction, both a neutron and a fast ejectile needed to be detected. To achieve this, the DAQ trigger logic was constructed to only record coincidence events between the two systems. For LENDA and VANDLE, the definition of a good trigger occurred whenever any bar had a signal in both the top and bottom PMT, within a 24-ns coincidence window. This initial check was conveniently performed internally by the FPGAs on the Pixie boards. The 24-ns coincidence window was chosen because it was the smallest value where the behavior of internal coincidence was reliable (at 8 and 16 ns, some coincidences would miss validation). The *OR* of all of the top-bottom coincidence in a given Pixie module was output from the Pixie breakout modules (this happend on the channel labeled *o7*). The breakout modules have lemo connectors for the available trigger inputs and outputs of the Pixie boards and are labeled as *PIXIE 16 Breakout modules* in Fig. 3.15. The outputs (*o7*) of all 8 Pixie modules were or-ed together to form the LENDA and VANDLE master trigger.

This master trigger was sent up to the S800 DAQ where it was input as the secondary trigger to the S800 trigger box. If a coincidence was found, the S800 DAQ would send a

live trigger signal back down to LENDA and VANDLE. During the time that the initial neutron master trigger went up to the S800 DAQ and back down, the Pixie boards buffered the detector signals (the delay was approximately 1.2 μs). The *live trigger* was sent back into the boards external validation input (*i4*) on the breakout modules, which triggered an internal validation window of 700 ns. The size of this window was chosen to be long enough to validate low-energy neutron events, while short enough to keep the rate of random coincidence from overwhelming the DAQ system. Under these conditions, a raw coincident event rate of approximately 500 per second was written to disk. The S800 singles rate was approximately 10k.

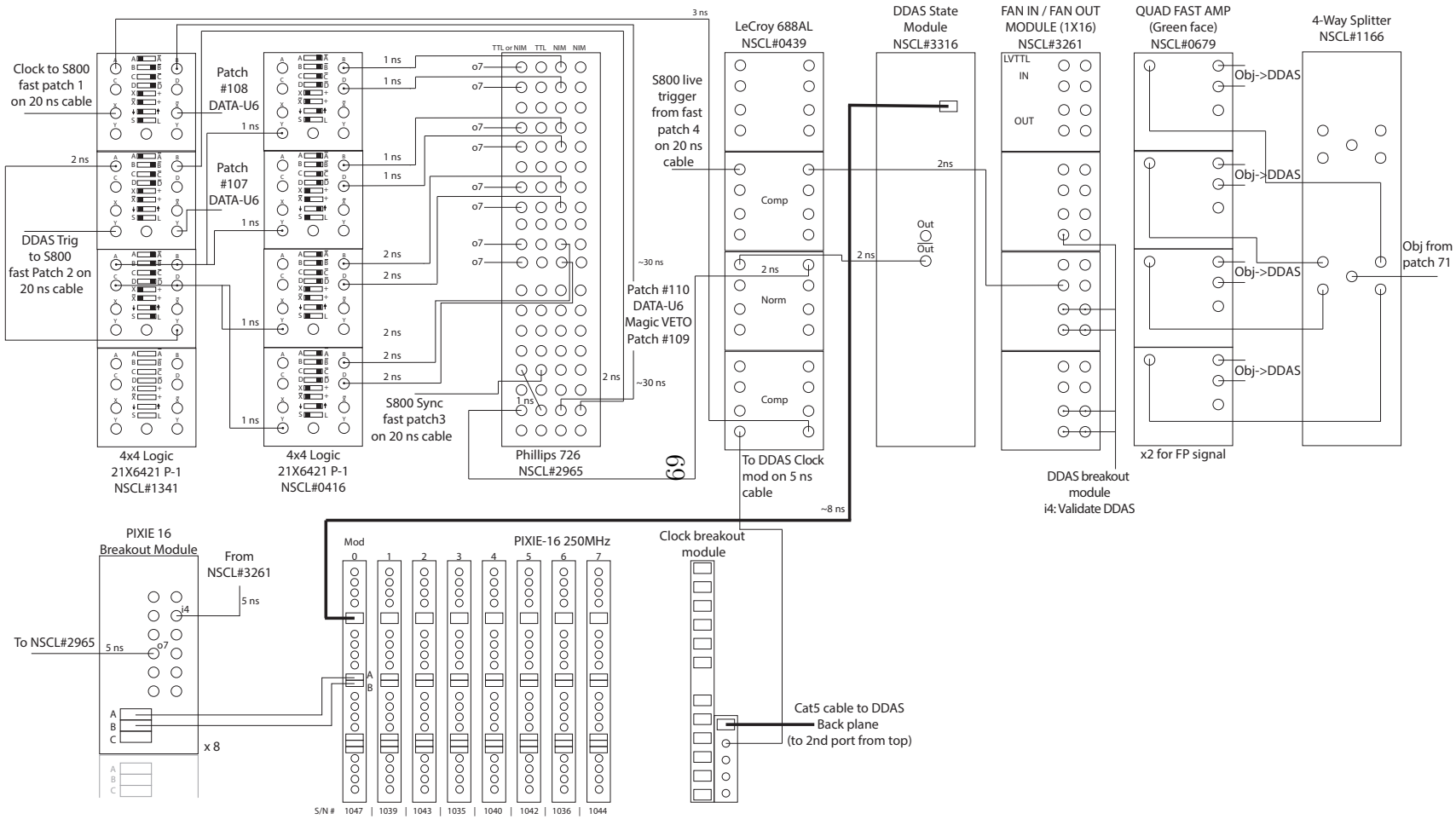

Figure 3.15: Detailed diagram of the electronics setup in experiment e10003. The NSCL numbers refer to the NSCL E-Pool number for the module depicted. Care has been taken to draw the modules with enough detail to make them easily recognizable. The positions of the switches depicted in the first two modules on the left correspond to their actual setting in the experiment.

Chapter 4

Data Analysis

Have you tried looking at the traces?

Remco Zegers

The purpose of this chapter is to discuss how the raw data from e10003 was processed and filtered to arrive at differential cross sections ($\frac{d\sigma}{d\Omega}$). To accomplish this, a ROOT based analysis package was developed to unpack, build, and analyze the experimental data. Throughout the data, analysis the different "reaction channels" are discussed. This language refers to the different final ejectile particles that are possible in the ^{16}C(p,n)^{16}N reaction (see Table 3.1). In some of the reaction channels, there is more than one rigidity setting of the S800 spectrograph used in the analysis of that channel. These parts of the data are referred to as "settings" or "rigidity settings".

4.1 Calibration

This section describes the details of the calibrations procedures used in e10003 for the neutron detectors and the focal plane detectors of the S800 spectrograph.

4.1.1 Neutron Detector Timing Calibrations

Since the basis of the (p,n) measurement is the TOF of the neutrons, the calibration of the timing signals from the neutron detectors is crucial. The first step in the calibration

procedure is to choose a start time for the neutron TOF. With the digital system, each signal in the setup has an absolute timestamp, which allows any signal to be chosen as the reference time for the TOF after the data taking. Originally, the in-beam scintillator located in the S800 object box was going to be used for this purpose. However, as the analysis progressed it became clear that this detector suffered significant radiation damage due to the high incident beam rate. This deteriorated the detector's timing properties beyond what was acceptable to achieve the physics goals of the measurement.

Instead, the timing of the beam-like ion measured by the E1 scintillator at the S800 focal plane was used as the reference time for the neutron TOF. This has the advantage of significantly lowering the incident particle rate (thousands instead of millions per second), preventing any radiation damage. However, using the S800 E1 scintillator introduces dependence of the neutron TOF on the dispersive angle and position in the focal plane.

Figures 4.1 shows the correlation between neutron TOF, and the dispersive angle and the dispersive position. These events come from the experimental data, where ^{15}N has been selected in the S800 focal plane (see Section 4.1.3 for details about the particle identification). The dependencies can be corrected by looking at the events from the γ flash seen prominently in both figures. Since the γ events must all occur at the same time, the correlation can be fit and removed. After these corrections are performed the position of the γ flash is used to calibrate this time difference to reflect the actual TOF from the target to the neutron detectors. Since the distance from the center of the target to the bars is known to be 1 m, the time that the γ flash should appear can be easily calculated (1m/c=3.33-ns).

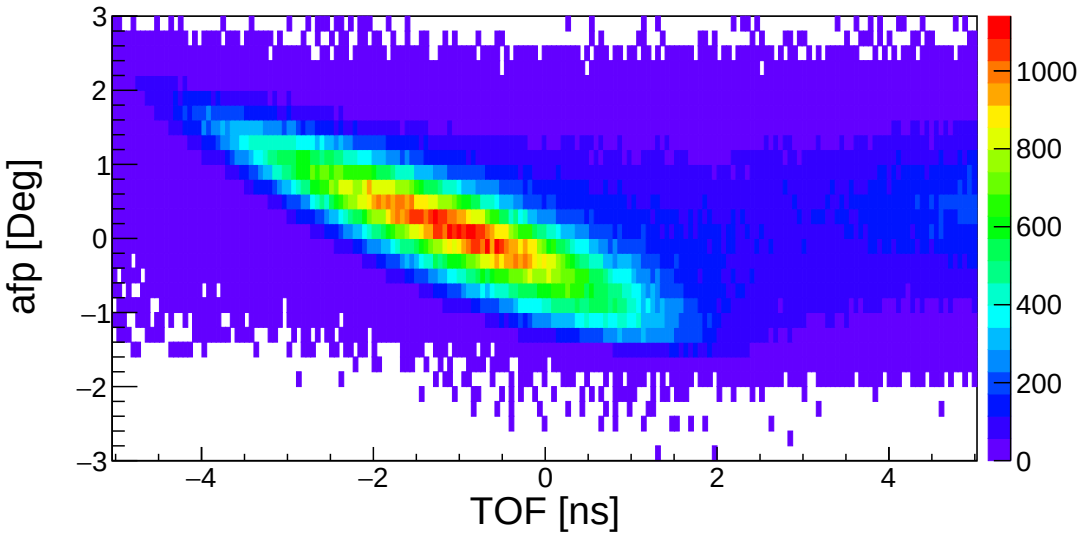

(a)

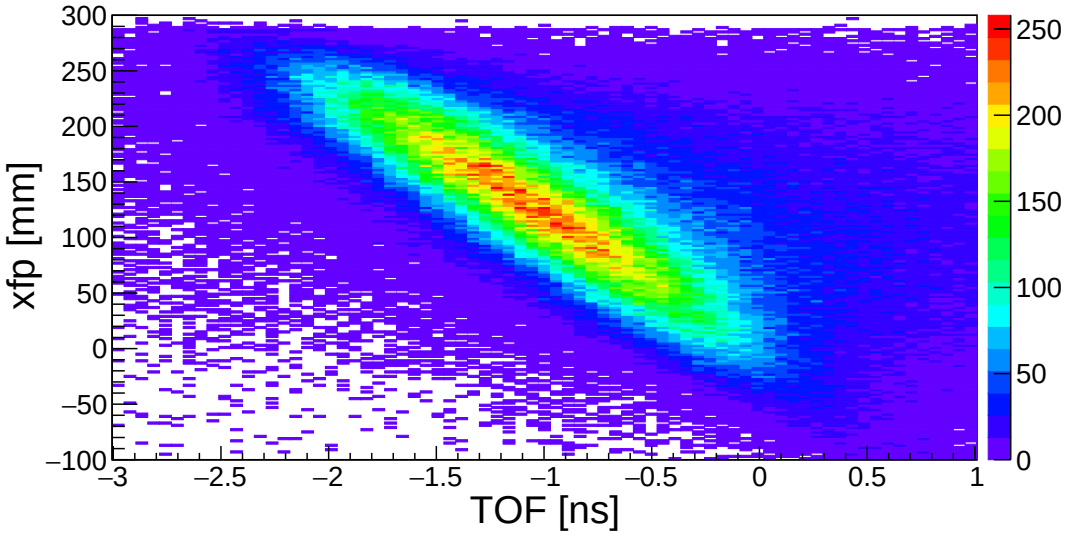

(b)

Figure 4.1: Two dimensional histogram showing the correlation between the neutron TOF, and dispersive angle (a) and position (b) in the S800 focal plane. The γ flash is seen prominently in the figures. The neutron events are to the right, but are cut off to clearly show the γ flash.

In addition to the corrections for the focal-plane parameters, the neutron TOF must also be corrected for any walk (dependance of the TOF on the signal height in LENDA or VANDLE). Fig. 4.2 shows this dependence for events where ^{15}N has been selected in the S800 focal plane.

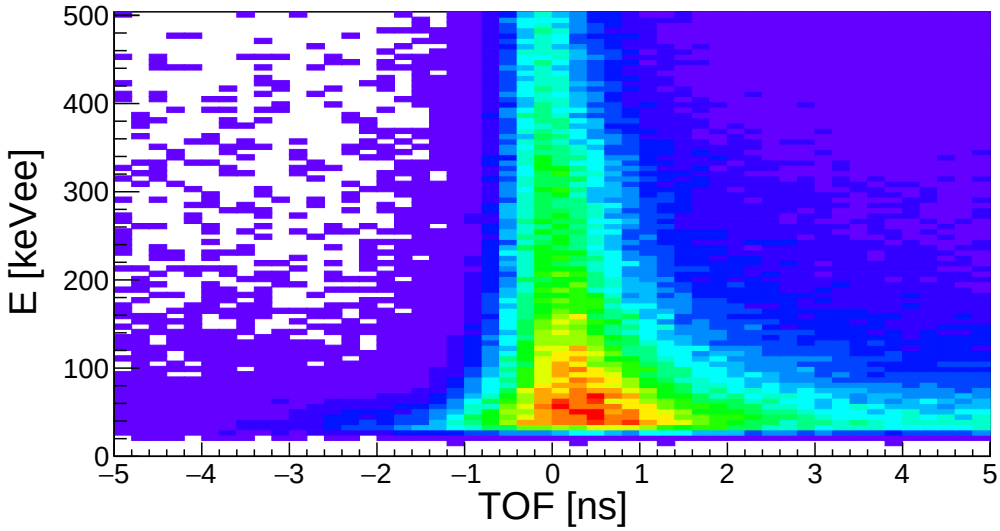

Figure 4.2: Neutron TOF plotted against the calibrated light output from the neutron detectors. The γ flash can be seen centered around 0. At low energies, a small correlation can be seen for the γ events.

Combining all of these effects provides the following expression for the neutron TOF,

$$TOF = T_n - T_{E1} - a(afp) - b(xfp) - \frac{c}{L_o} - T_{offset}, \tag{4.1}$$

where T_n is the timestamp from LENDA or VANDLE, T_{E1} is the timestamp from the top PMT of the S800 focal-plane scintillator, afp is the dispersive angle in the focal plane, xfp is the dispersive position in the focal plane, L_o is the light output seen in LENDA or VANDLE in keVee, and a, b and c are correction coefficients.

Fig. 4.3 shows the fully corrected TOF spectrum for the ^{15}N data. The γ events are seen

cleanly separated from the neutron events by TOF. A FWHM timing resolution of ∼700-ps is achieved in the experimental data. Similar calibration procedures were used for the other channels of interest ^{14}N, ^{15}C, ^{14}C, ^{16}N. Their TOF spectra are shown in Fig. 4.4.

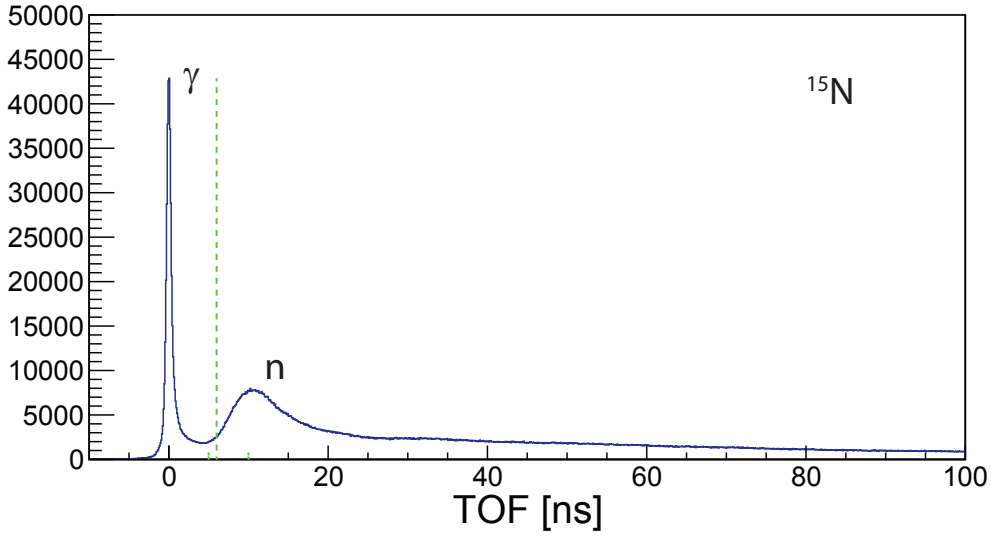

Figure 4.3: Fully Corrected neutron time of flight spectrum for the N15 data (3.1325 Tm setting). The dashed green line indicates the TOF cut between γ and neutron events. It corresponds to a neutron kinetic energy of ∼67 MeV, which is far above the energies used in the analysis.

As can be seen in the Fig. 4.4, the γ flash for the ^{15}C channel has a long tail and what appears to be poor resolution. Since the target material is hydrogen, the γ rays must come from some excited state in the ejectile. However, below the neutron emission threshold, ^{15}C has only 1 known state at 740-keV. Since this state has a long lifetime of 2.61 ns, the γ flash appears smeared out. The ^{15}C can emit the γ ray later along its flight path, increasing the total distance it must travel to the neutron detectors. This effect was simulated and included in the timing calibration of the ^{15}C data.

Fig. 4.4 also shows a sharp peak to the right of the γ flash in the ^{15}C and ^{14}C TOF spectra. These peaks come from a strong neutron-knockout background that dominates at

forward lab angles. Details of this background and its subtraction are given in Section 4.4.

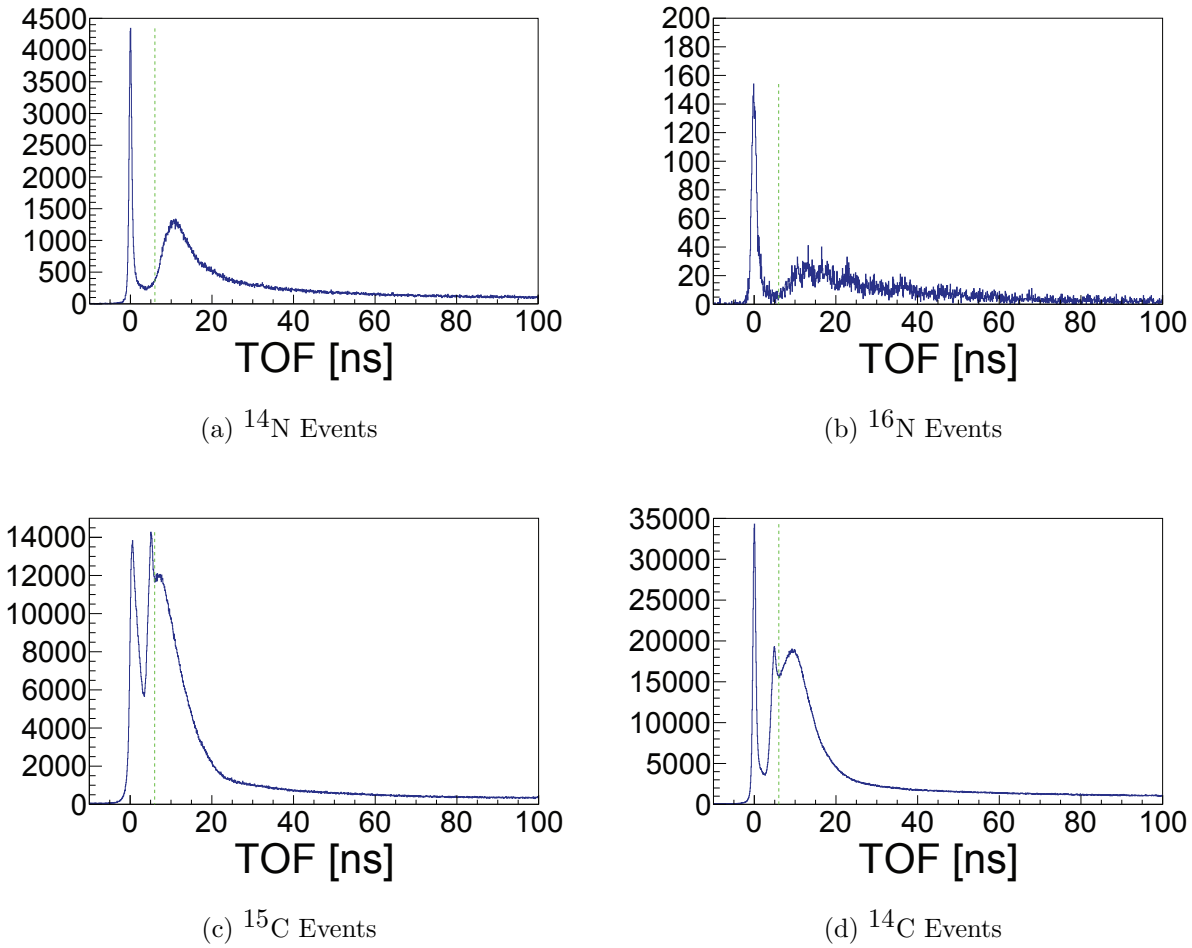

(a) ^{14}N Events

(b) ^{16}N Events

(c) ^{15}C Events

(d) ^{14}C Events

Figure 4.4: Corrected neutron TOF spectra for the ^{14}N (2.9 Tm) (a), ^{16}N (3.38 Tm) (b), ^{15}C (3.6565 Tm) (c), and ^{14}C (3.38 Tm) (d) channels. The ^{15}C and ^{14}C data from the 3.52 Tm and 3.2828 Tm settings are not shown, but have similar TOF spectra.

4.1.2 LENDA and VANDLE Gain Calibrations

Though the light output from the neutron detectors is not directly used in the determination of the excitation energy and COM scattering angle, it is necessary for setting the neutron detection threshold. The threshold affects the neutron detection efficiency and therefore the differential cross section. To accomplish this the light output for each bar is calibrated into

keVee using γ sources ^{241}Am, ^{22}Na and ^{137}Cs. The specific gamma rays used and their specifications are summarized in the Table 4.1.

Source	E_γ	Type	$E_\gamma^{\text{Reduced}}$
^{22}Na	1274.5	CE	1061.7
^{22}Na	511	CE	340.7
^{137}Cs	661.7	CE	477.4
^{241}Am	59.5	Ph	59.5
^{241}Am	26.3	Ph	26.3

Table 4.1: Table of the γ-ray calibration sources used for the neutron detector gain calibration. See text for details.

E_γ is the true energy of the emitted gamma ray, CE refers to compton edge, Ph refers to photo-absorption and $E_\gamma^{\text{Reduced}}$ is the expected energy of the gamma ray in the neutron detectors. For photo-absorption the expected energy is unchanged, but for compton edges the energy is reduced (see Appendix B for more details).

The gain for the top and bottom PMT of each bar were matched in software using the compton edge of ^{137}Cs. The total energy of the bar was then defined as,

$$E = \sqrt{E_T E_B}, \tag{4.2}$$

where $E_{T,B}$ are the gain matched energies for the top and bottom PMTs. The energy for the bar was then calibrated into keVee using the compton edges from ^{22}Na and the photo-peaks from ^{241}Am,

$$E^{Cal} = g \cdot E + Th, \tag{4.3}$$

where g is the gain and Th is the threshold from the fit.

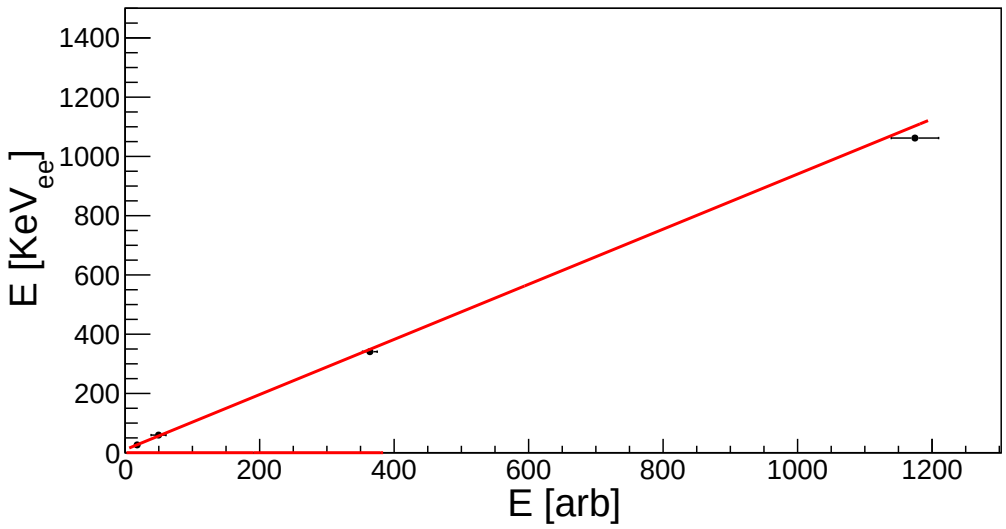

Figure 4.5: Example light output calibration for south LENDA bar 2. The data points are described in Table 4.1. The red line is a linear fit to the data.

Fig. 4.5 shows an example of the calibration curve from a LENDA bar (south LENDA 2) using the 4 points from ^{241}Am and ^{22}Na. The neutron detection threshold is set using this calibrated energy for each bar. The uncertainty in the calibrated energy from fitting uncertainties and drifts in the gain during the experiment are included in the final systematic error for the differential cross section.

4.1.3 Particle Identification

Though the experimental conditions are tuned to explore charge-exchange reactions, many other processes can trigger the DAQ by producing a neutron and an ejectile in the ^{16}C + p reaction. To filter away the events from these processes the timing and energy loss information from the E1 scintillator and the ion chamber in the S800 are used to make a particle identification plot. This allows only the ejectile of interest (^{16}N, ^{15}N, ^{14}N, ^{15}C, ^{14}C)

to be included in the data analysis. Fig. 4.6 shows an uncalibrated particle identification plot for the 3.1325 Tm rigidity setting (the main setting for ^{15}N), where the TOF of the ion to the S800 focal has been shifted to near zero for convenience.

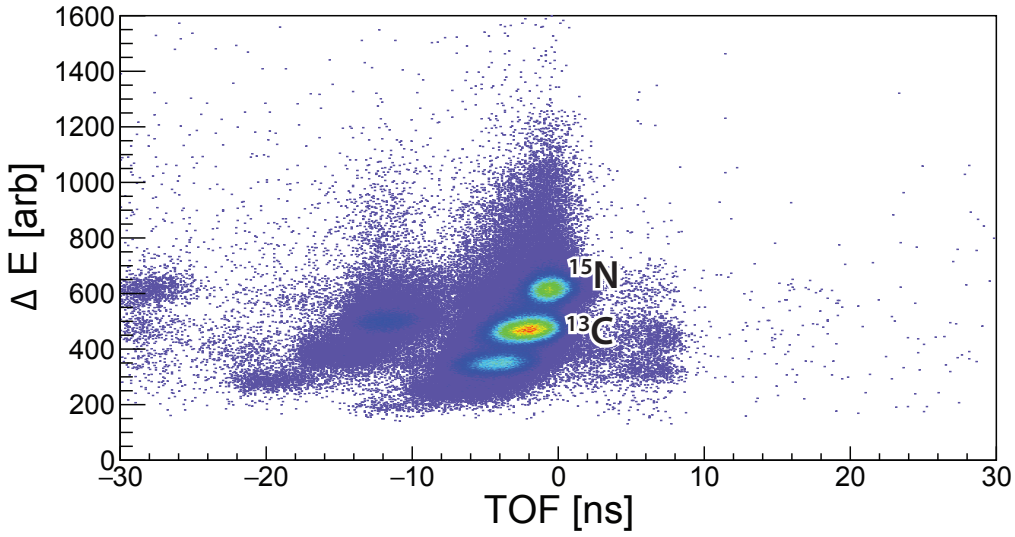

Figure 4.6: Uncalibrated Particle Identification for the 3.1325 Tm setting.

While even at this level separation between different particles can be seen, the resolution of both the TOF and energy loss signals can be improved by correcting for the dependence on dispersive position and angle in the focal plane. Fig. 4.7 shows these dependencies for the TOF when the ^{15}N events are selected in the uncalibrated PID spectrum shown in Fig. 4.6. Similar correlations and corrections exist for the energy loss measured in the ion chamber.

After applying these corrections a particle identification plot is constructed for each rigidity setting. Fig. 4.8 shows a corrected PID spectrum from 4 of the rigidity settings measured in the experiment, each of which highlights an exit channel of interest. Elliptical gates are made on each particle extending out to 2 sigma in TOF and ΔE. The good events cut away in this process are included in the final normalization of the differential cross section. These gates are shown as black ellipses in Fig. 4.8.

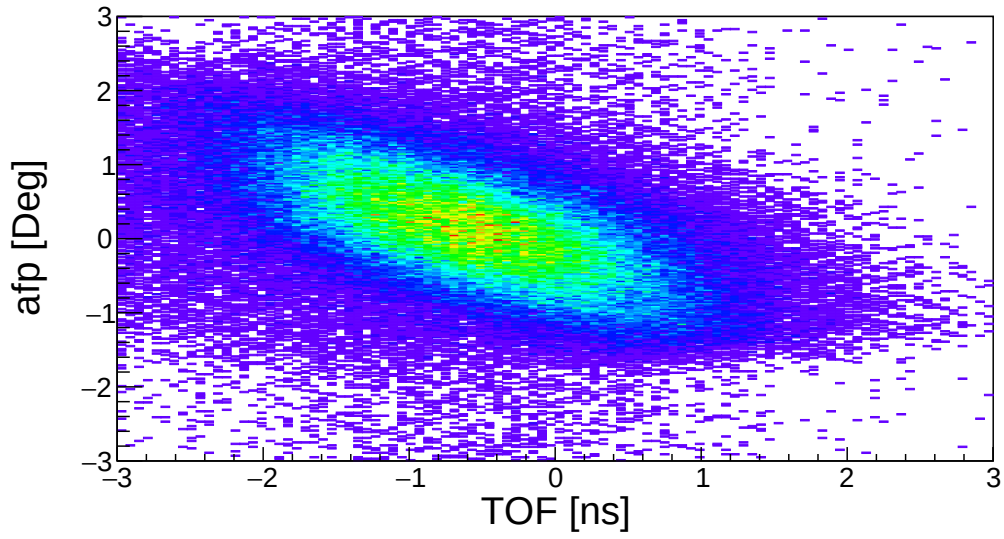

(a)

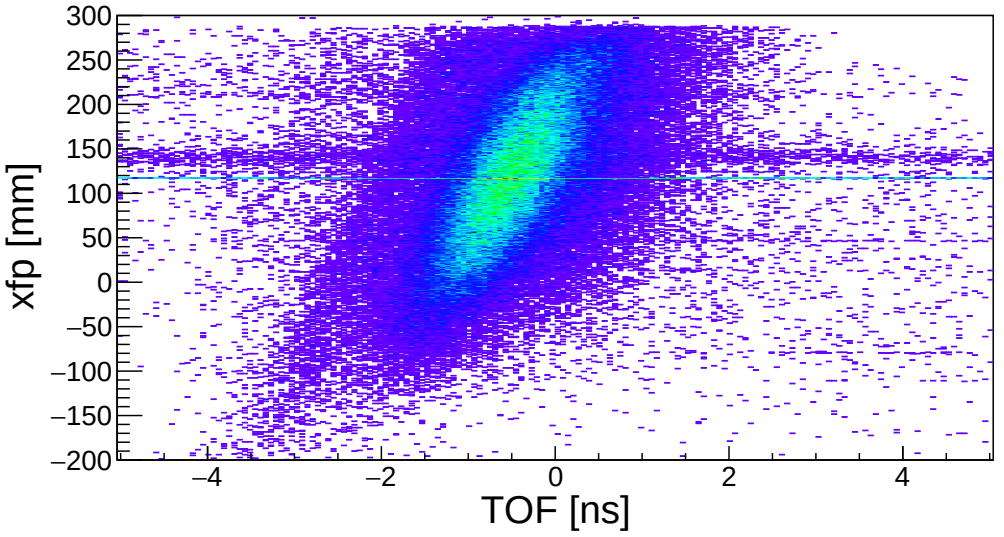

(b)

Figure 4.7: Correlation between the ejectile TOF and the dispersive angle (a) and position (b) in the S800 focal plane for ^{15}N events. The artifacts seen in (b) are the result of bad events in the CRDCs, which are removed in subsequent steps of the analysis.

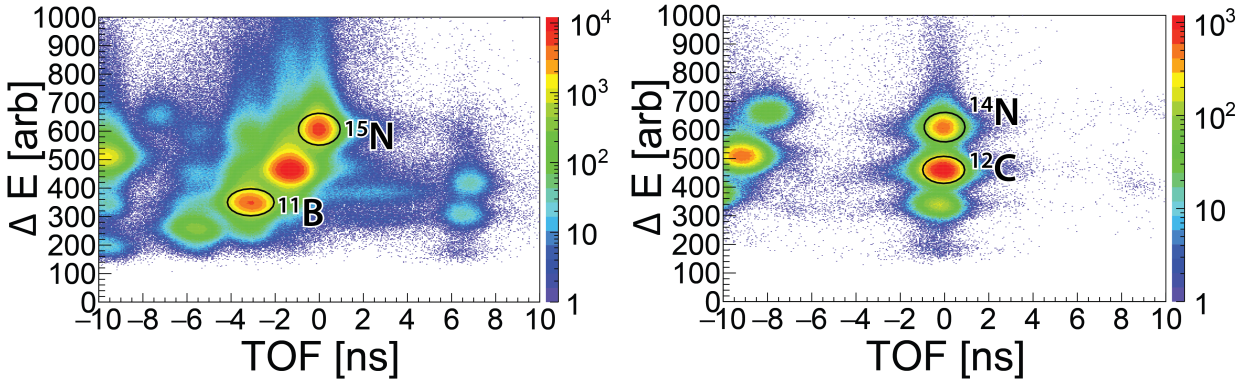

(a)

(b)

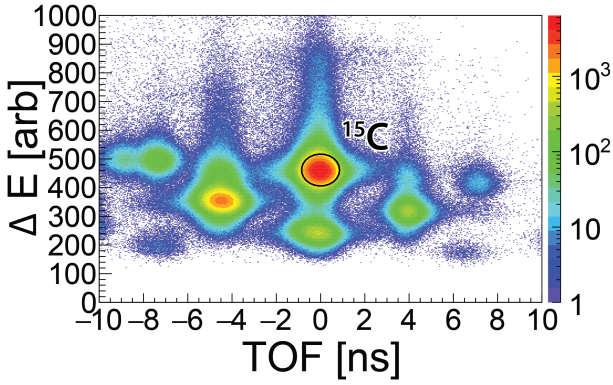

(c)

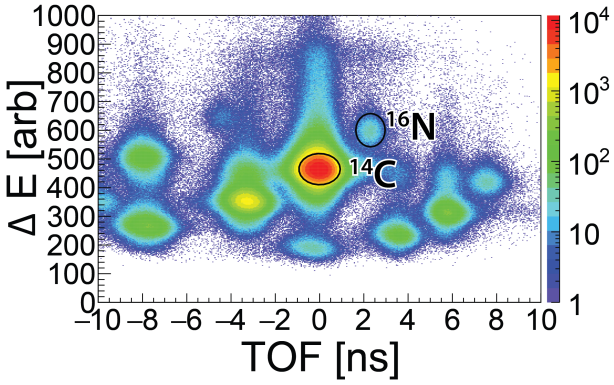

(d)

Figure 4.8: Corrected PID spectra from the 3.1325 Tm (a), 2.9 Tm (b), 3.6565 Tm (c), and 3.38 Tm (d) settings. The main particles of interest in each setting are indicated. The remaining two settings 3.52 Tm and 3.2828 Tm are not shown, but are similar to the 3.6565 Tm and 3.38 Tm settings.

4.1.4 CRDC Calibration

In order to find the particle's position and angle from the pad distribution and electron drift time measured by the CRDCs, the detectors must be calibrated. To accomplish this a metal plate (a "mask") with a series of known holes and strips is placed 8 cm upstream of each CRDC for a calibration measurement. The result of these calibration runs are shown in Fig. 4.9, where the mask hole and strip pattern is clearly visible. Taking the measured drift time and pad position of several of these holes a linear calibration of the form,

$$X_{1,2}(mm) = s^x_{1,2}(mm/pad) \cdot X(pad) + c^x_{1,2}(mm) \tag{4.4}$$

$$Y_{1,2}(mm) = s^y_{1,2}(mm/ns) \cdot Y(ns) + c^y_{1,2}(mm), \tag{4.5}$$

can be fit to the data. The $s^{x,y}_{1,2}$ coefficients refer to the slope of the calibration for x and y of CRDCs 1 and 2. Similarly $C^{x,y}_{1,2}$ are the offsets from these calibrations. Since the x measurement comes from discrete PADs, the slope for that calibration is just the width of the pads, 2.54 mm/pad. The constant offset can be found by using any of the holes seen in Fig. 4.9. For the Y direction, 3 vertical points in the center of the mask pattern were used in the fit.

To accurately determine the x position from the PAD distribution, the gains of the PADs must be matched and the resulting distribution fit on an event-by-event basis. If the gains of some PADs are substantially larger than the others, the fits can be biased towards those PADs, creating artifacts in the spectrum. Fig. 4.10 shows the effect of this calibration step for CRDC 1.

Once the positions for both CRDCs are fully calibrated, the dispersive and non-dispersive

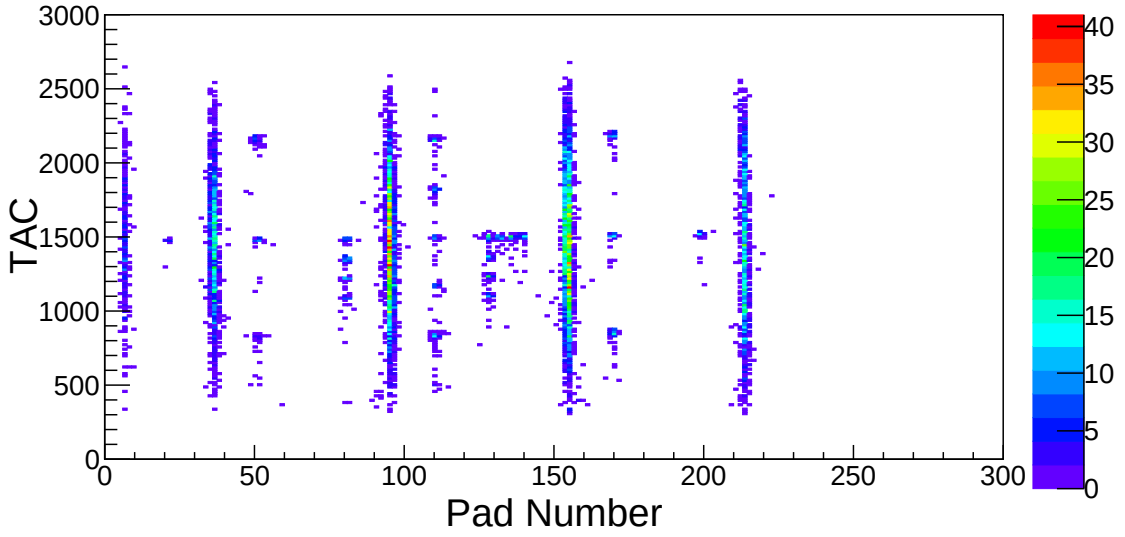

(a) CRDC 1

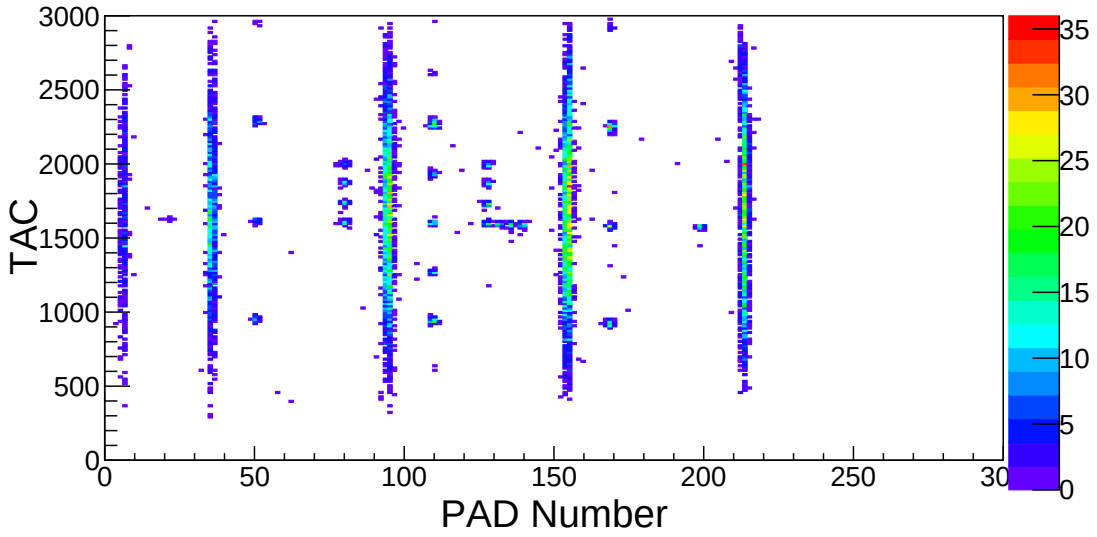

(b) CRDC 2

Figure 4.9: The uncalibrated position (x-axis) and time (y-axis) measured by the CRDCs during the mask runs.

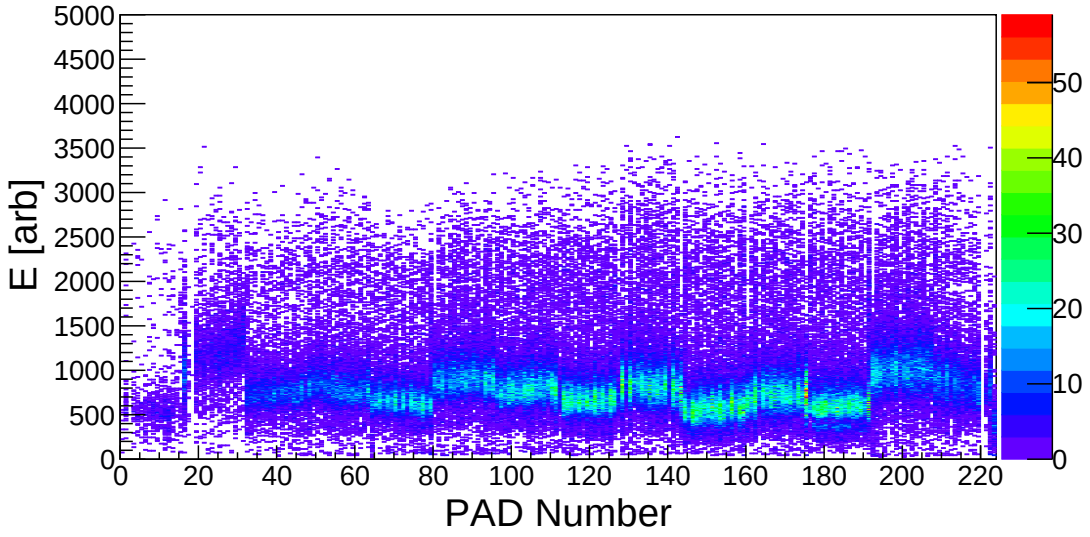

(a)

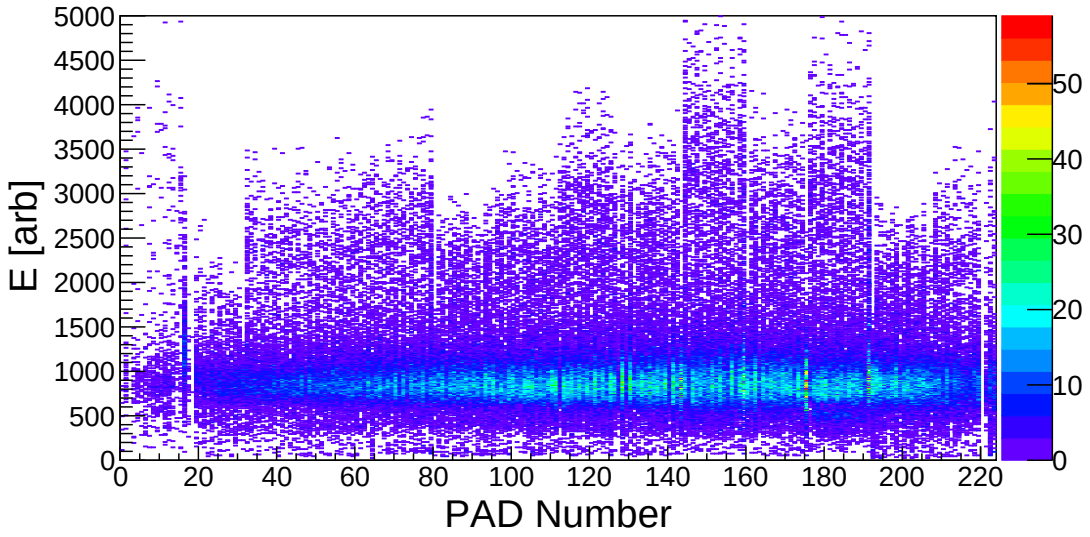

(b)

Figure 4.10: The pad distribution for CRDC 1 before (a) and after (b) the pad-by-pad gain matching. The data is from one experimental run of the 3.1325 Tm rigidity setting.

angles can be calculated,

$$afp = atan((X_2 - X_1)/1073.0) \tag{4.6}$$

$$bfp = atan((Y_2 - Y_1)/1073.0), \tag{4.7}$$

where 1073.0 is the distance between the CRDCs in mm. This defines 4 parameters for the particle's track in the focal plane.

However, determining the particle's properties at the target position is often a more critical piece of information. Specifically for this measurement, the ejectiles momentum distribution is needed so that the cross section can be corrected for the momentum acceptance of the spectrometer, and the different rigidity settings can be stitched together. To accomplish this the transfer map of the spectrograph is calculated using the ion optics code COSY infinity [110]. With the inverse map (M^{-1}) calculated by COSY the target parameters can be derived,

$$\begin{bmatrix} ata \\ yta \\ bta \\ dta \end{bmatrix} = M^{-1} \begin{bmatrix} xfp \\ afp \\ yfp \\ bfp \end{bmatrix}. \tag{4.8}$$

The "ta" (as opposed to "fp") designation is a common convention to indicate that these are the values at the target position. Similar to the focal plane parameters *ata* (*bta*) is the dispersive (non-dispersive) angle at the target, *yta* is the non-dispersive position, and *dta* is the deviation of the particles' energy relative to the energy of the center track through the spectrometer (E_0). The kinetic energy of the ejectile can be determined from *dta* easily through,

$$E = E_0(1 + dta). \tag{4.9}$$

From the energy and angles, the momentum vector $\vec{p}$ can be determined. The ejectiles kinetic energy is used to investigate the acceptance of the spectrometer (see Section 4.5.2 for more information).

With the above calibrations completed, we have the ingredients necessary to calculate the COM scattering angle and excitation energy for each event. The following sections go through the major analysis steps needed to extract absolute differential cross sections from the data.

4.2 Experimental Yield

In order to calculate the COM differential cross section as a function of excitation energy in ^{16}N, the lab measurements must be transformed into the correct variables. For the (p,n) reaction in inverse kinematics this is done with missing-mass spectroscopy, where the excitation energy of ^{16}N can be found with,

$$E_x = \sqrt{(M_p + M_{16_C} + T_{16_C} - M_n - T_n)^2 - (P_{16_C}^2 + P_n^2 - 2P_nP_{16_C}Cos(\theta_n))} - M_{16_N}. \tag{4.10}$$

M_x, T_x and P_x refer to the rest mass, kinetic energy and momentum of particle x in the lab frame respectively. θ_n is the lab scattering angle of the neutron. The momentum of the neutron and ^{16}C are given by,

$$P_x = \sqrt{2M_xT_x + T_x^2}. \tag{4.11}$$

To find the center of mass scattering angle the following relation is used,

$$\Theta_{cm} = Sin^{-1}\left(\frac{P_n^{lab}}{P_n^{cm}} Sin(\theta_n)\right), \tag{4.12}$$

where the P_n^{cm} is found by Lorentz boosting the neutron lab momentum vector into the COM frame.

The above relations were used to find the excitation energy and COM scattering angle for each event. The yields in the lab and COM are presented in Fig. 4.11. The plots on the left show a two dimensional histogram of lab neutron kinetic energy (y-axis) and neutron scattering angle (x-axis) for the different decay channels. The figures on the right show the corresponding two dimensional histogram of COM scattering angle (y-axis) and excitation energy in ^{16}N (x-axis). On the left, the expected kinematic relationships for the ^{16}N, ^{15}N, and ^{14}N channels are clearly visible. However, for the ^{15}C and ^{14}C channels there is little apparent structure. Instead the spectra are overwhelmed with forward peaking background events. These events come from neutron-knockout reactions that have the same outgoing particles as true charge-exchange reactions. The neutrons from these events scatter off the downstream quadrapole magnet and hit the neutron detectors, creating false coincidences. Section 4.4 will discuss this background in more detail.

The data were separated into two-degree bins in COM scattering angle and the excitation energy histogramed to form the experimental yield. As an illustrative example, Fig. 4.12 shows the experimental yield in the $\Theta_{cm} = 4 - 6^\circ$ bin for the ^{15}N channel. The acceptance of the neutron detectors is clearly visible in the spectrum, where it creates artificial peak-like structures. Also evident in the spectrum are background events that need to be subtracted. The following sections will discuss the neutron acceptance corrections and the background

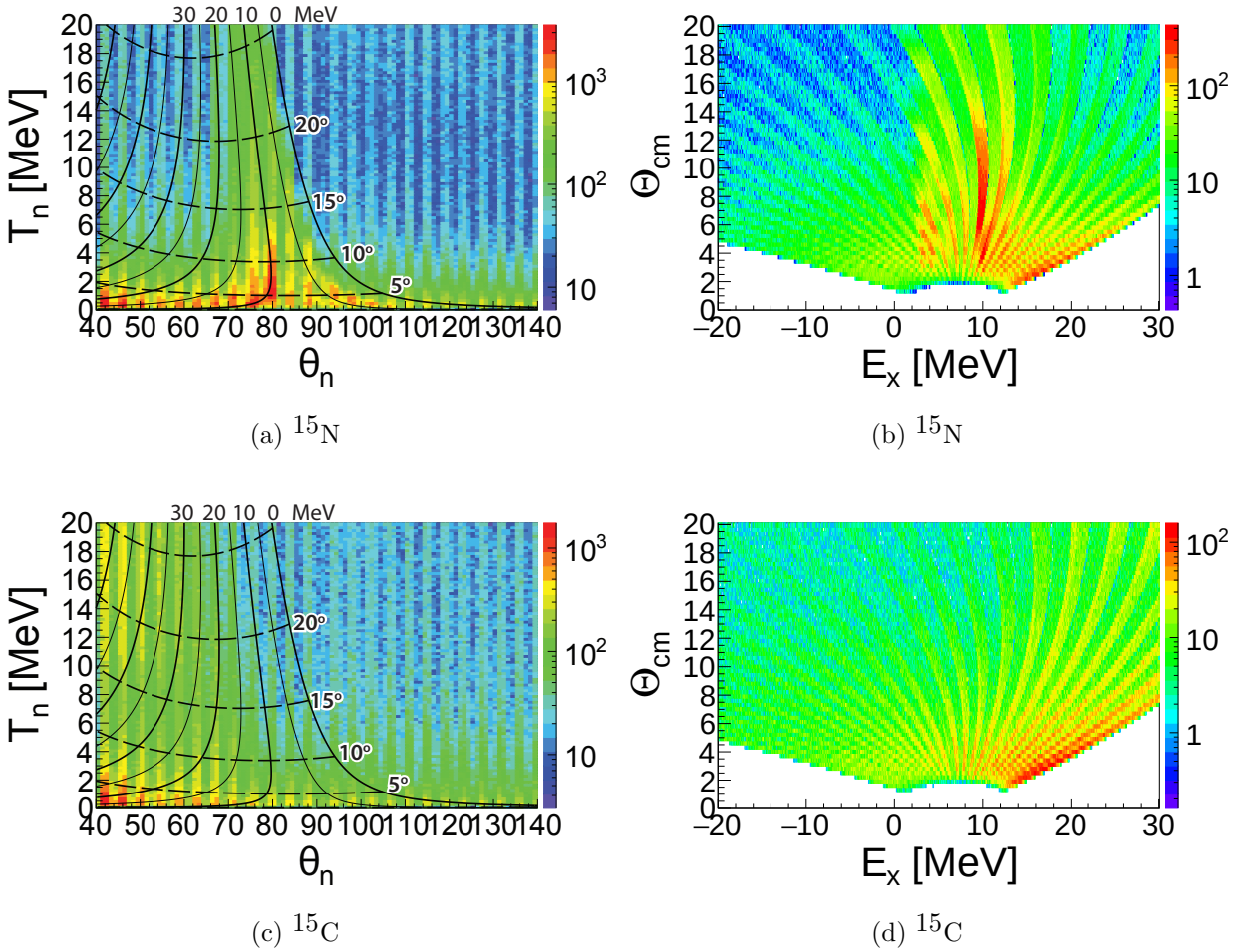

(a) ^{15}N

(b) ^{15}N

(c) ^{15}C

(d) ^{15}C

Figure 4.11: Two dimensional histogram of lab neutron angle and kinetic energy measurements (a,c,e,g,i), and reconstructed excitation energy in ^{16}N and COM scattering angle (b,d,f,h,j). In (a,c,e,g,i) the solid lines indicate excitation energy in ^{16}N and the dashed lines indicate the COM scattering angle.

Figure 4.11: cont'd

(e) ^{14}C

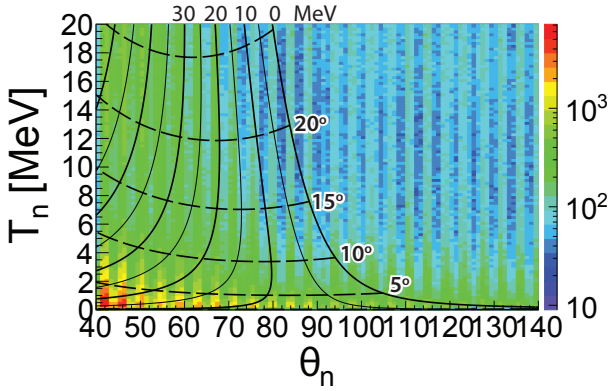

(f) ^{14}C

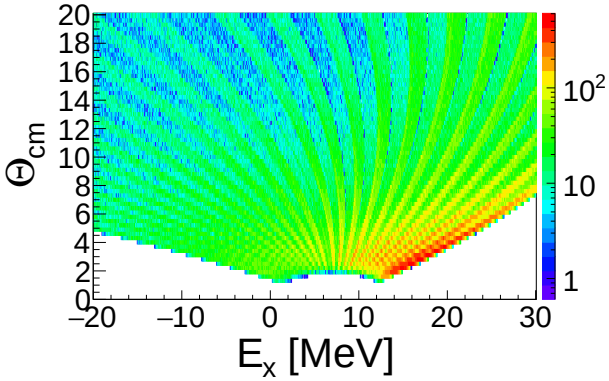

(g) ^{16}N

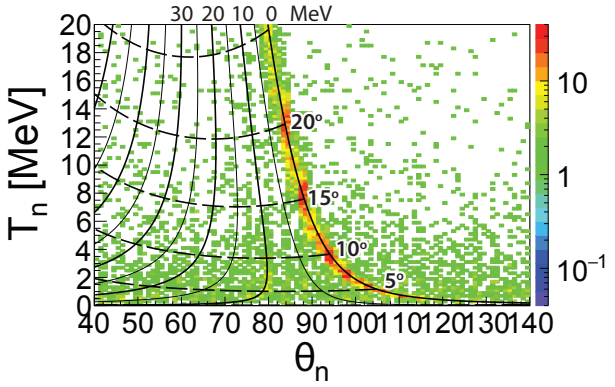

(h) ^{16}N

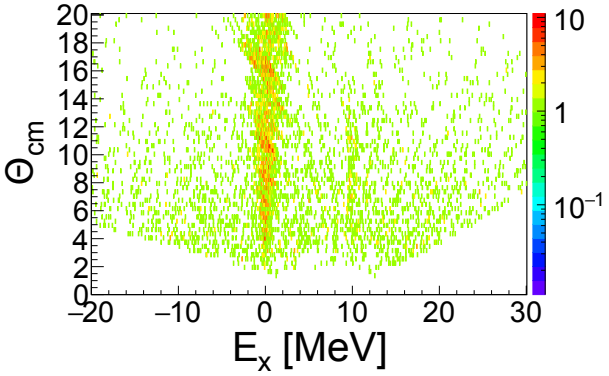

(i) ^{14}N

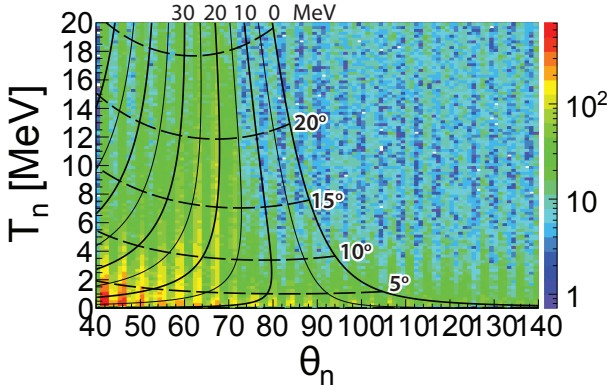

(j) ^{14}N

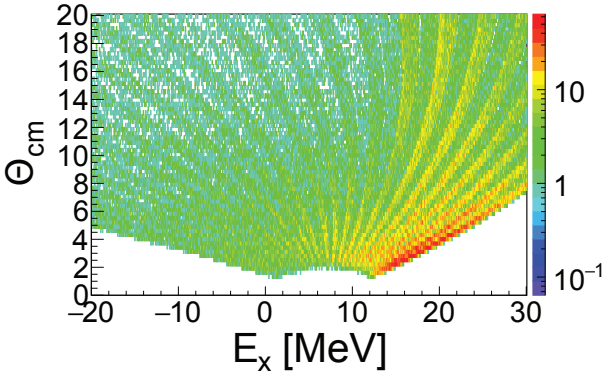

subtraction methods used for the different channels.

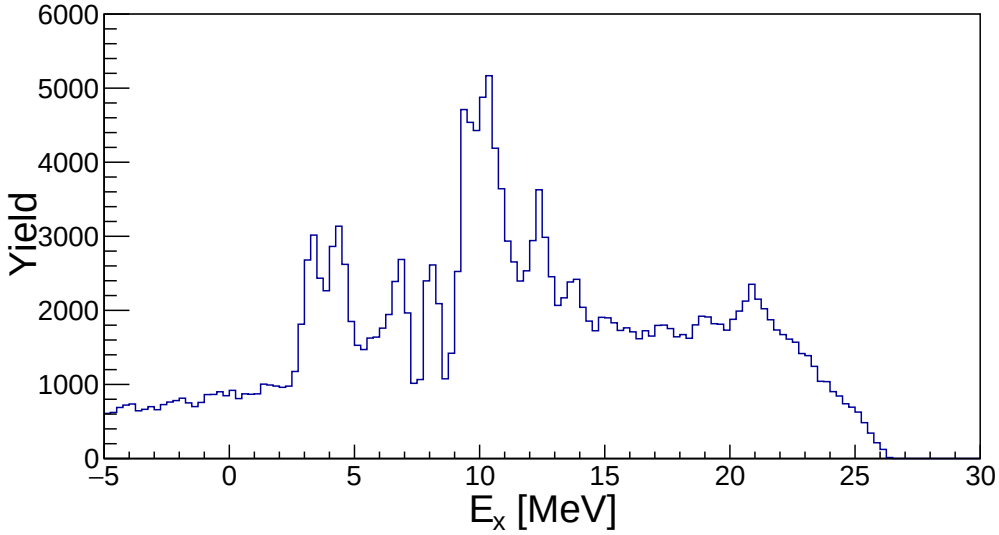

Figure 4.12: Experimental yield for the ^{15}N channel (3.1325 Tm) in the $\Theta_{cm} = 4 - 6^{\circ}$ bin.

4.3 Neutron Detector Efficiency and Acceptance

Of significant importance to determining the absolute cross section for the ^{16}C(p,n)^{16}N reaction is the intrinsic neutron detector efficiency and geometrical acceptance of the LENDA and VANDLE bars. As was done in previous work with LENDA, the efficiency for each bar is determined through a Monte Carlo simulation that has been validated against experimental measurement [63, 64]. For e10003 this was done using the GEANT4 simulation toolkit [111] and its associated high-precision neutron physics library [112]. This is the same approach used by the VANDLE collaboration [93] and the European Low Energy Neutron Spectrometer (ELENS) [113].

In order to be detected by LENDA or VANDLE the neutron must first interact with the hydrogen or the carbon nuclei in the plastic scintillator. A cartoon of this process is

show in Fig. 4.13. In principle the neutron can interact with any combination of hydrogen and carbon nuclei, however the light output from interactions with the carbon is highly quenched [113, 93]. These carbon reactions can therefore contribute only a small amount to the detector's response in the neutron energy region of interest (< 20 MeV). The elastic scattering on hydrogen dominates the spectrum.

Fig. 4.14 shows the light output for plastic scintillator in keVee for protons, ^{12}C, and ^{4}He as a function of incident particle energy (adapted from [114]). The quenching of the carbon's light output can be clearly seen–a 1 MeV proton will result in a 177.7 keVee of light output but a 1 MeV ^{12}C will make only 6.6 keVee. This effect pushes the carbon interactions below the light-output threshold for all but the most energetic carbon scatterings. The low-energy tail of the light-output function for protons was modified to better reproduce the measured neutron response from the ^{252}Cf data presented in Fig. 3.14. This is shown as the dotted blue line in Fig. 4.14. These light-output curves were used in the simulation of the neutron detection efficiency.

Fig. 4.15 shows the result of the Geant4 simulation, where neutrons between 0 and 20 MeV were impinged on a single LENDA bar from a point like source. The light output was determined in the simulation by taking the energy loss from each simulation step inside the LENDA bar and converting it to a light output using the functions shown in Fig. 4.14. The light output of all the steps are added together to arrive at a total light output for the simulated event.

In the previous work with LENDA [63, 64], MCNP was successfully used to simulate the response of the neutron detectors. Using Geant4 has allowed all aspects of the simulation to be done in one framework. Within the simulation the beam profile, the bulging of the target windows, the energy loss of the beam in the target, and the neutron detector response are

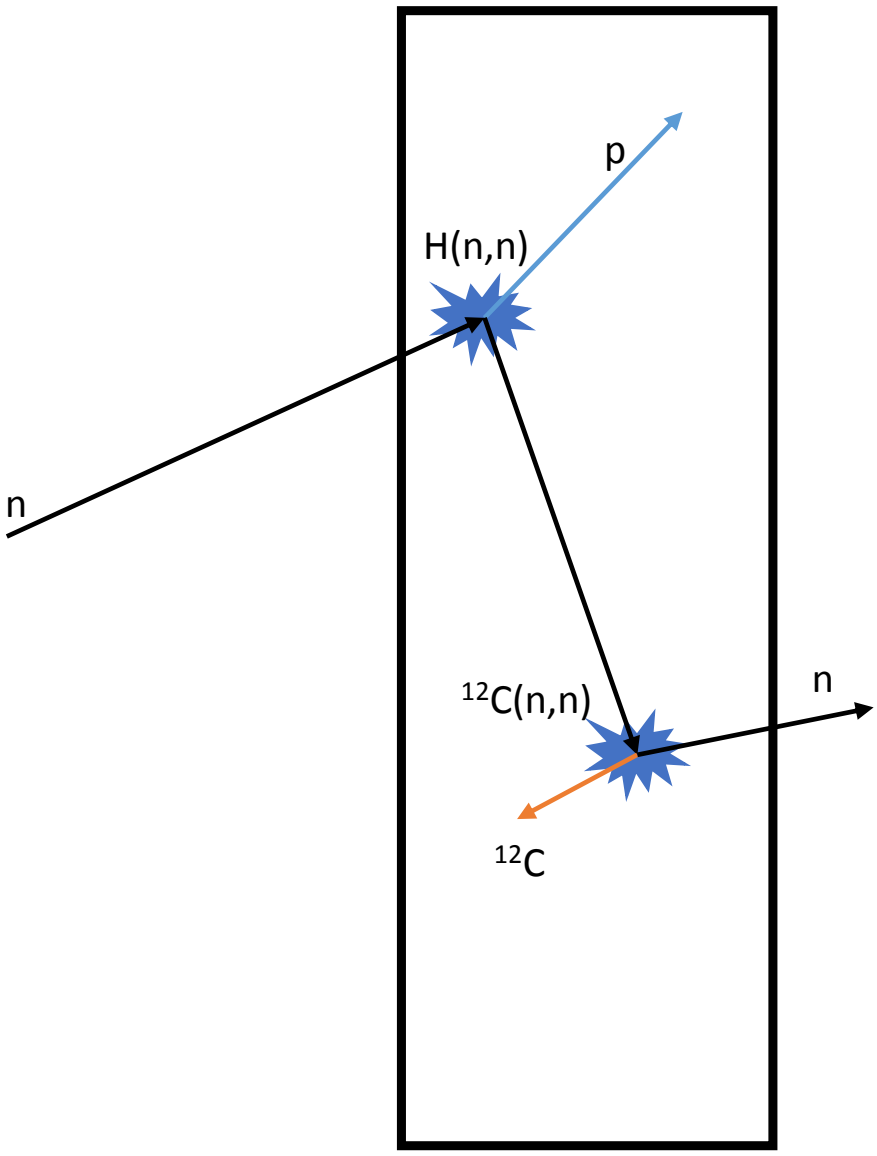

Figure 4.13: A cartoon depicting the interactions of neutrons in a plastic scintillating material. In order for the neutron to be detected it must undergo a nuclear reaction with the hydrogen or carbon nuclei in the material. The angles of the scattering are exaggerated for artistic purposes. The dominate elastic scattering on hydrogen is shown at the top of the figure. Elastic (shown at the bottom of the figure) and inelastic (not shown) scattering on ^{12}C are also possible but highly quenched. See text for details.

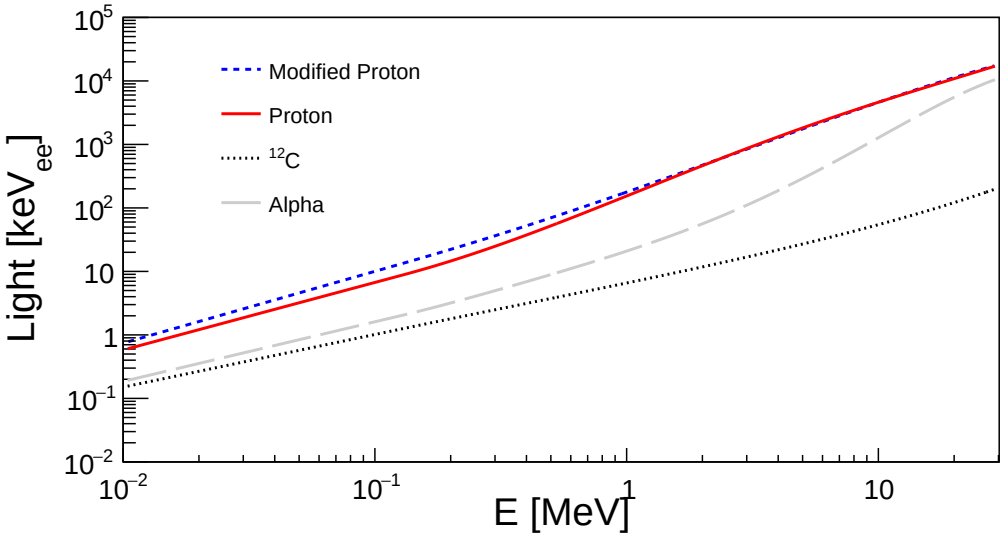

Figure 4.14: Light output curves for BC-400 plastic scintillator. Each line shows the expected light output as a function of incident particle energy. Adapted from [114] see text for details.

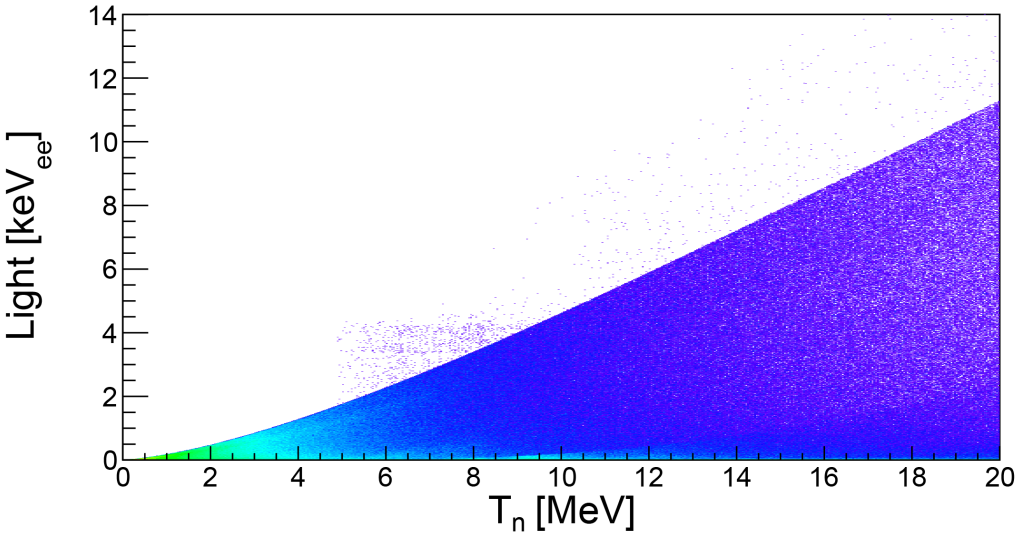

Figure 4.15: Two dimensional histogram of light output and incident neutron energy from the Geant4 simulation. Contributions from elastic scattering on hydrogen and ^{12}C are included in the simulation. Inelastic channels for carbon scattering are also included and create the few events above the elastic scattering trend line. These events amount to a tiny portion of the data (<0.05%).

all included at the same time.

To obtain at a simulated efficiency for the LENDA bar, a light output threshold must be applied in the simulation to match the data. The threshold for the data was set at 30 keVee as determined for each bar following the calibration procedure outlined in Section 4.1.2. An effective threshold of 25 keV_{ee} and a scaling factor of 0.92 was applied to the simulation since it better reproduced the measured efficiency at low neutron energies. Fig. 4.16 shows the result of the Geant4 simulation with the measured efficiency overlaid at a threshold of 30 keVee. This efficiency was measured using a ^{252}Cf fission source as described in Ref. [90].

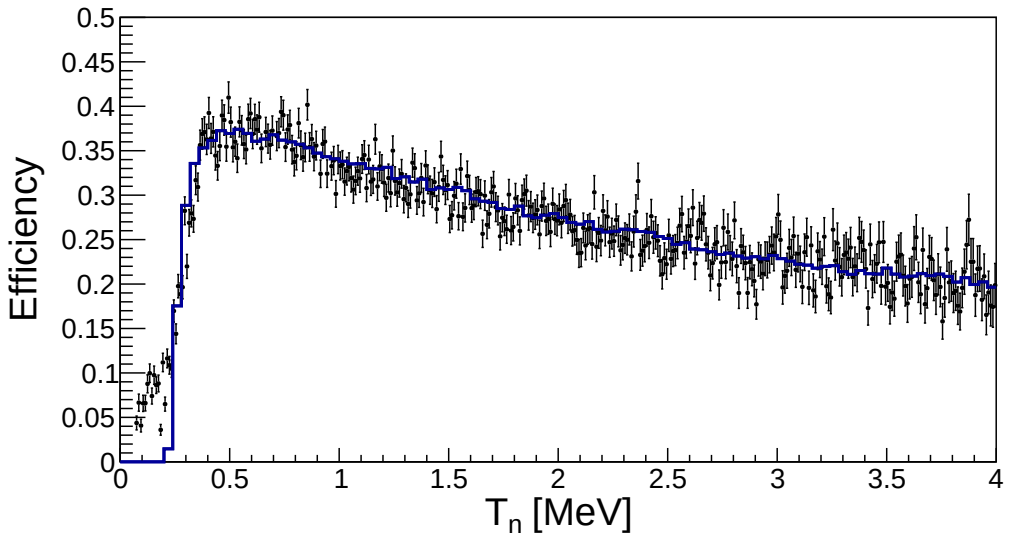

Figure 4.16: The black points show the measured intrinsic neutron detection efficiency for a single LENDA bar at a light output threshold of 30 keVee. The blue line is the result of the Geant4 simulation of the efficiency. Good agreement is seen.

Confident with the simulations ability to reproduce the intrinsic neutron detector efficiency, the simulation was used to calculate the total neutron acceptance as a function of COM scattering angle and excitation energy for the full experimental setup. The beam was simulated through the bulged liquid hydrogen target, where it underwent a charge-exchange reaction. When the scattered neutron hit one of the detectors, the event was recorded. The

result of this simulation is shown in Fig. 4.17, where the neutron energy and angle have smeared to match the experimental resolution and transformed into the COM frame.

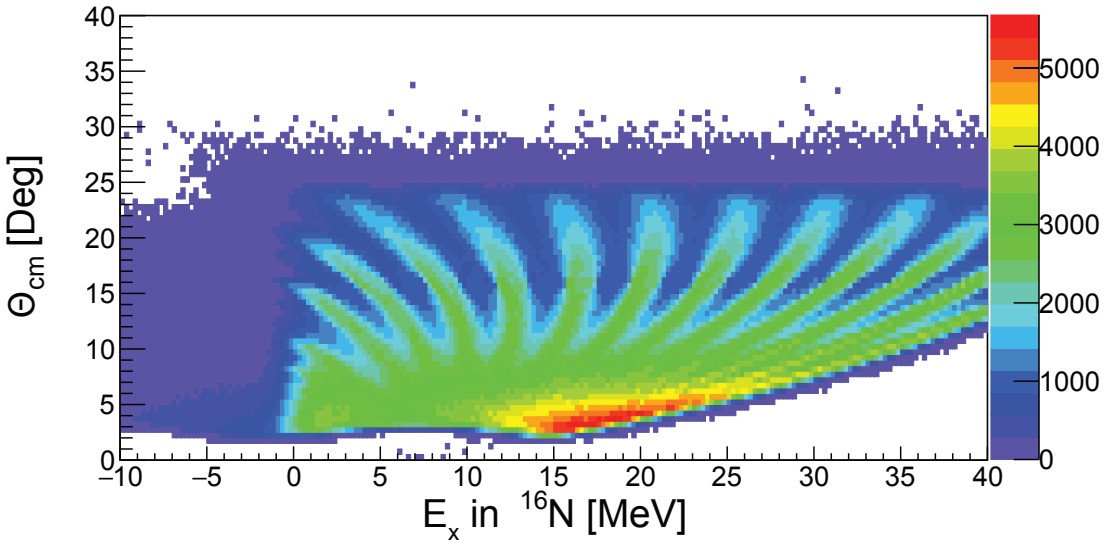

Figure 4.17: Two dimensional histogram of Θ_{cm} and E_x in ^{16}N from the Geant4 simulation of the e10003 setup.

The total detection efficiency as a function of COM scattering angle and excitation energy is obtained by taking projections of Fig. 4.17 onto the x-axis in the same COM scattering angle binning used in the analysis and dividing by the total number of events simulated in that bin. Figs. 4.18 shows the simulated efficiency for the most forward (Θ_{cm}=4-6°) and most backward (Θ_{cm}=14-16°) angles used in the analysis. The sharp, periodic features seen in both figures are the result of measuring the lab scattering angle with discrete bars of differing geometrical acceptance–the VANDLE bars cover approximately twice the solid angle as the LENDA bars. These simulated curves were used to correct the experimental yields for the acceptance in each COM scattering angle bin used in the analysis.

The simulation was also used to determine the experimental excitation-energy resolution of the full setup. This was done by simulating the response of the neutron detectors to

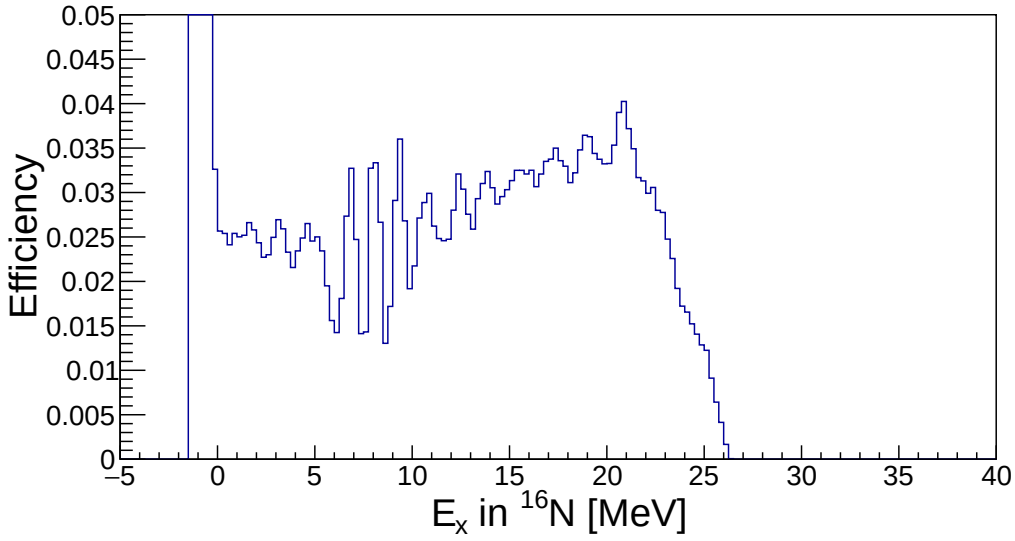

(a)

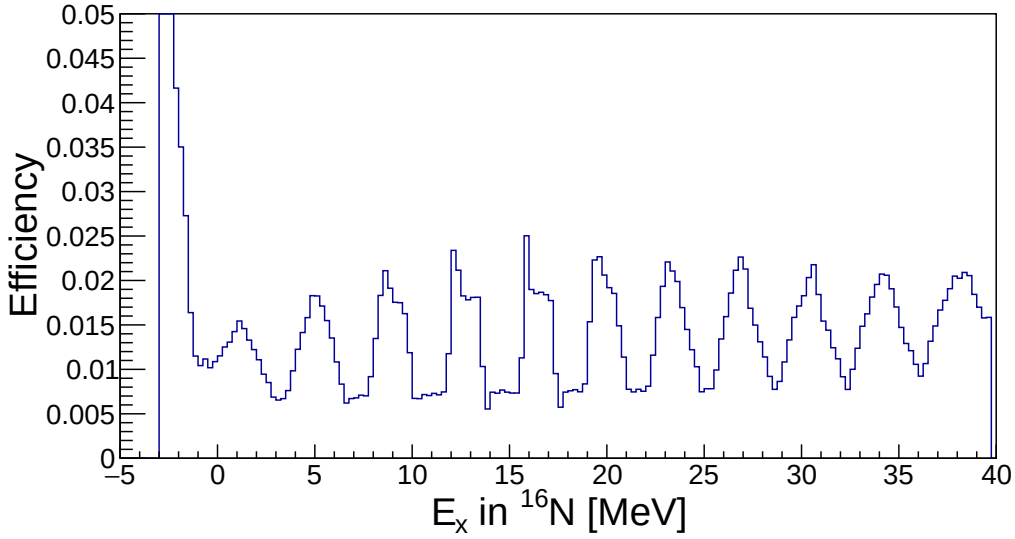

(b)

Figure 4.18: Simulated neutron acceptance and efficiency in the Θ_{cm}=4-6 ° (a) and Θ_{cm}=14-16° (b) bin for the e10003 setup.

events with discrete excitation energies. As was seen in Ref. [64], the resolution worsened at large COM scattering angles. The resolution varied from $\sigma(5^\circ)_{\mathrm{FWHM}} \approx 750$ keV to $\sigma(15^\circ)_{\mathrm{FWHM}} \approx 2$ MeV. The following section describes the background subtraction used in the analysis.

4.4 Background Subtraction

There are various possible background sources that can contribute to the charge-exchange spectrum. They can be categorized as:

- Foil background. There may be reactions off of the non-hydrogen nuclei in the Kapton foils that surround the liquid-hydrogen target.
- Random background. The TOF spectrum may have random coincidences between neutrons and uncorrelated beam bunches.
- Beam-induced background. Reactions on the hydrogen other than charge exchange that produce the correct ejectile of interest and a neutron.

The foil induced background was studied by taking data with the empty target at the conclusion of the experiment. This was done in all of the rigidity settings used in the experiments. The contribution from these events was found to be vanishingly small ($< \%0.5$) and could not be determined accurately with the statistic of the background runs. Instead the thickness of the target was increased to include the hydrogen nuclei in the Kapton foils and a systematic uncertainty of 0.5% was included. The random background was inspected by looking at events that occurred at negative TOFs. The rate of random coincidences was also found to be very small ($< 1\%$). Similar to the foil background, the random background

shape could not be accurately determined and was included as a systematic error. The choice to use the S800 E1 scintillator for the neutron TOF made the random rate far less than in previous experiments when an in beam scintillator was used [63]. See Section 4.7 for a breakdown of the systematic errors.

The vast majority of the background events came from knockout or fragmentation reactions on the hydrogen in the target that produced the correct ejectile and a neutron. These reaction types are associated with fast neutron emission at forward scattering angles. These neutrons can scatter off the surrounding materials and hit a LENDA or VANDLE bar, sometimes creating a false coincidence. In this circumstance the TOF of the neutron is not related to its energy and creates a complex background. Since modeling the different background processes and the scattering of the neutrons from different materials in the experimental vault was a difficult task, a background model built off the experimental data was used.

Different techniques were used for the different reaction channels since the background shapes and intensity were different. For the ^{15}N and ^{14}N channels, a background model was based on events that created ^{11}B in the spectrometer. Events that create ^{11}B cannot be from charge-exchange reactions in the excitation energy range of interest of 0-20 MeV (the ^{11}B channel would open at 42 MeV). Therefore they should give a good representation of the neutrons from the possible background processes. A similar technique was used in the first LENDA (p,n) experiment [63, 64]. Fig. 4.19 shows the two dimensional histogram of neutron energy and scattering angle for ^{15}N gated events and ^{11}B gated events. Even at the preliminary level the shape of the ^{11}B spectrum seems to reproduce the shape of the background seen in the ^{15}N data.

A more detailed look at the ^{11}B model for the background reveals that some rescaling is needed to characterize the background at higher excitation energy. Fig. 4.20 shows the

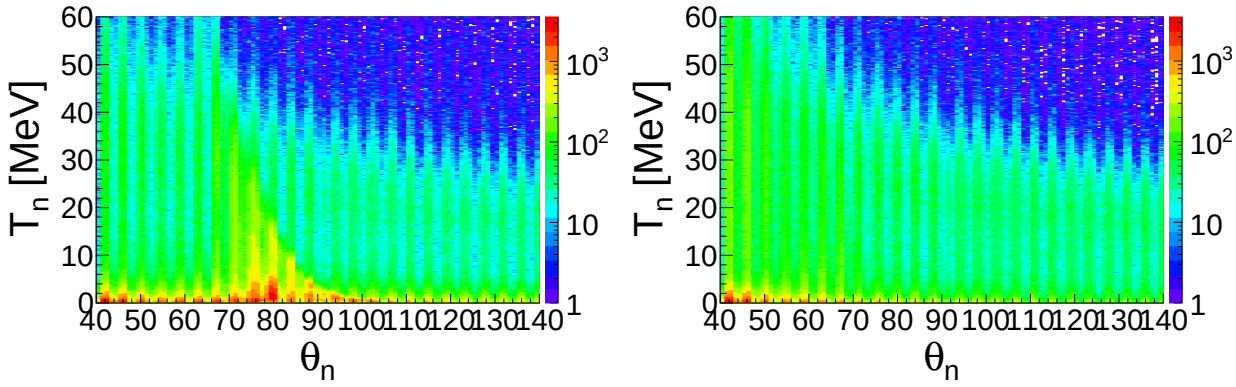

(a) ^{15}N (b) ^{11}B

Figure 4.19: Two dimensional histogram of lab neutron scattering angle and neutron kinetic energy for ^{15}N (a) and ^{11}B (b) gated events. The events from ^{11}B are used to model the background seen in the ^{15}N channels.

ratio of the ^{15}N and ^{11}B data integrated between neutron kinetic energy of 40 and 60 MeV as a function of lab scattering angle. The blue points show the region of θ_n that contains charge-exchange events, while the black points contain only background. A linear function was fit to the black points to yield a rescaling function that models the background seen in the ^{15}N channel.

Using this model yields the background shape in Fig. 4.21, where the forward ($\Theta_{cm} = 4-6^{\circ}$) and backward ($\Theta_{cm} = 14-16^{\circ}$) most angles are shown. The background is normalized to the data in the unphysical region below the channel's threshold (2.5 MeV for ^{15}N). The data presented in Fig. 4.21 still contains the jagged acceptance of the neutron detectors and so contains periodic structures. Building the background model from the experimental data reduces systematic error because mistakes in the acceptance of the bars are the same between the data and the background model. A similar procedure was performed for the ^{14}N data. The ^{11}B data was again used as the background model, but with a different rescaling function.

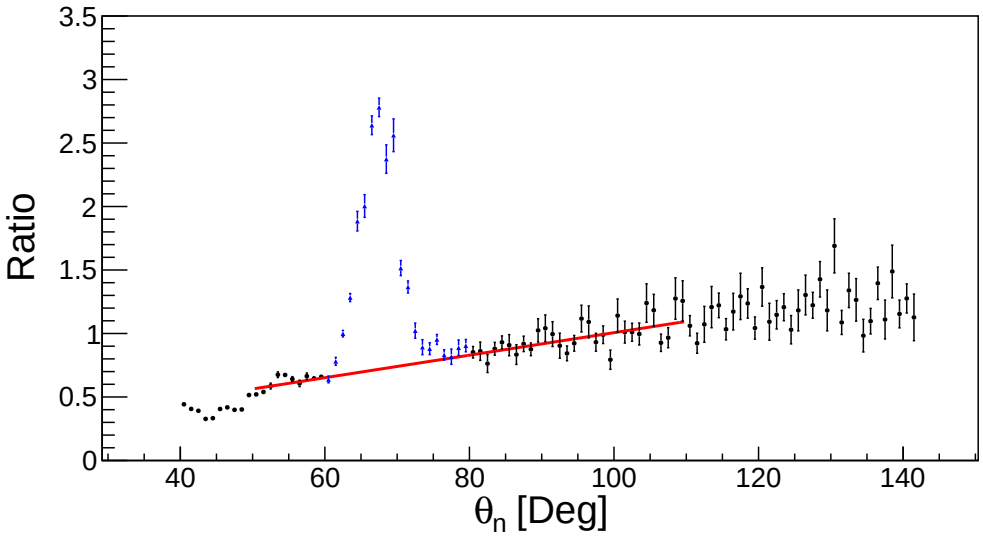

Figure 4.20: Ratio of the ^{15}N and ^{11}B gated events integrated from 40 to 60 MeV in neutron kinetic energy as a function of the lab neutron scattering angle. The blue points show the region of charge-exchange reactions, while the black points indicate regions with only background. The red line is a linear fit to the black points in the range shown.

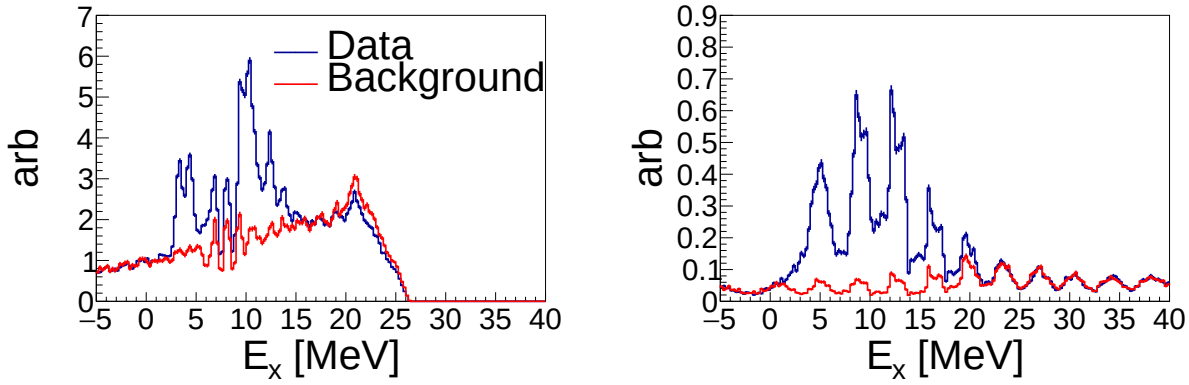

(a) ^{15}N at Θ_{cm}=4-6°

(b) ^{15}N at Θ_{cm}=14-16°

Figure 4.21: Experimental yields with overlaid background shape from the ^{11}B models. The most forward (Θ_{cm}=4-6°) and backward (Θ_{cm}=14-16°) COM angles are shown.

Characterizing the background for the ^{15}C and ^{14}C channels proved to be difficult due to the large amount of neutron-knockout and fragmentation reactions. After many iterations, events from the low-energy tail of the ejectiles kinetic energy distribution was used to estimate the shape of the background. Fig. 4.22 shows the kinetic energy distribution for the ^{15}C channel. The full distribution is reconstructed from two rigidity settings: 3.52 and 3.6565 Tm. The gray line represent the full distribution after combining the two settings with corrections for incomplete acceptance. The spectrum contains both charge-exchange and background events. However, charge-exchange events up to 20 MeV of excitation energy cannot create the events seen in the low-energy tail of the distribution. This makes these events a good candidate for a background model.

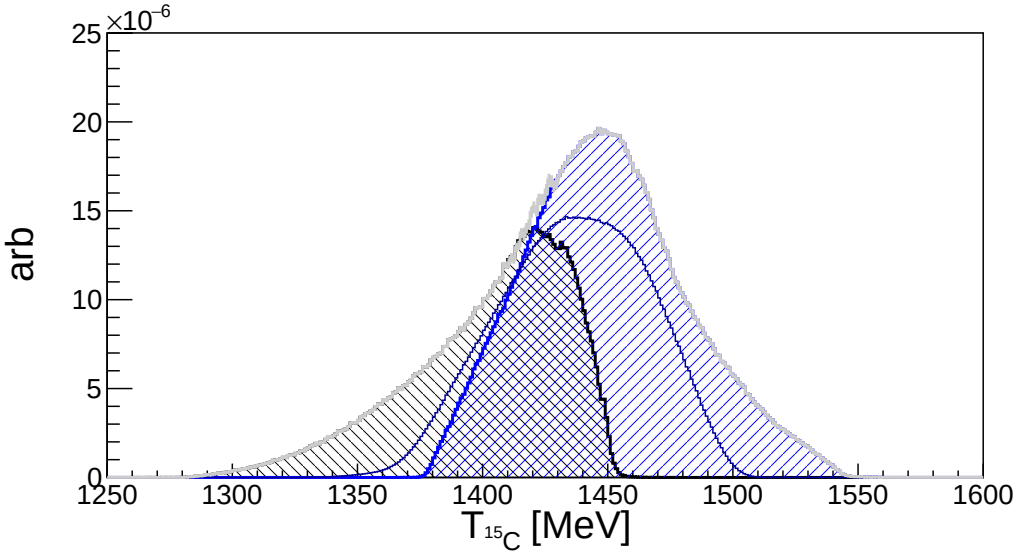

Figure 4.22: The kinetic energy spectrum of ^{15}C events detected in the S800 Spectrograph. The black (blue) hashed region comes from the 3.52 (3.6565) Tm rigidity setting. The gray line is the full distribution constructed from the two settings. The thin blue line shows the simulated distribution from charge-exchange reactions. The low-energy tail of the distribution is energetically inaccessible to charge-exchange reactions and so must come from background processes.

Fig. 4.23 shows the data and the above background model for the forward and backward

most scattering angles gated on the ^{15}C and ^{14}C channels. In both cases, the signal to background is clearly much lower than the ^{15}N case. Both channels have limited yield for the $\Theta_{cm} = 4 - 6^{\circ}$ bin with increased strength appearing at backwards angles. The statistics for the ^{15}C background model are clearly limited. However, this technique was the best compromise between statistical and systematic error for this channel.

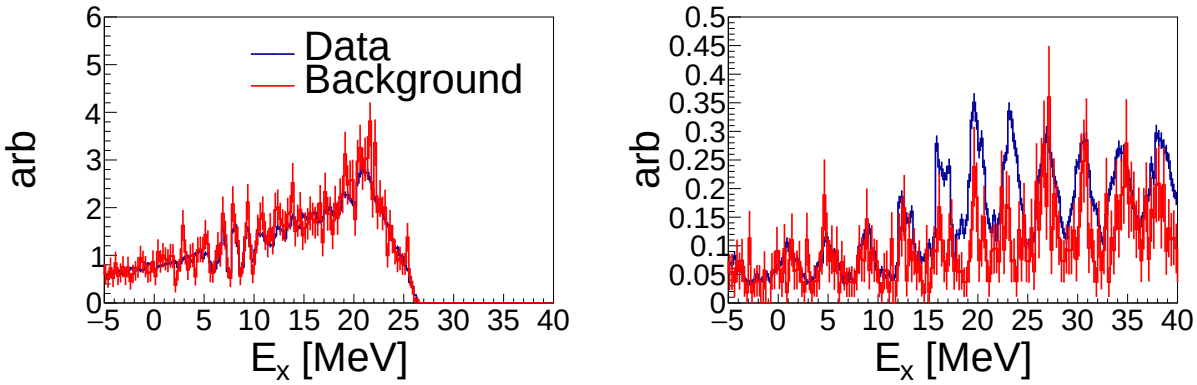

(a) ^{15}C $\Theta_{cm} = 4 - 6^{\circ}$

(b) ^{15}C $\Theta_{cm} = 14 - 16^{\circ}$

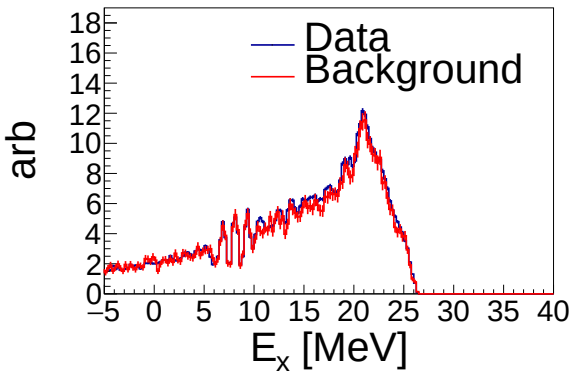

(c) ^{14}C $\Theta_{cm} = 4 - 6^{\circ}$

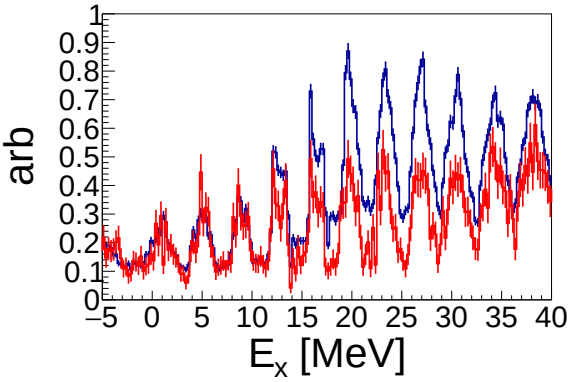

(d) ^{14}C $\Theta_{cm} = 14 - 16^{\circ}$

Figure 4.23: Experimental yield and background models for the ^{15}C and ^{14}C channels. The data comes from the 3.6565 Tm and 3.38 Tm rigidity settings respectively. Yield is primarily seen at backward angles.

The ^{16}N channel does not suffer from a complex background because the PID cut on ^{16}N ensures that no breakup or fragmentation reaction occurred. A flat background subtraction

was done based on a linear fit to the data at higher excitation energies where there is no strength in the ^{16}N channel.

4.5 Absolute Normalization Corrections

The goal of e10003 was to measure absolute cross sections in the ^{16}C(p,n)^{16}N reaction. This meant measuring the beam rate incident on the liquid-hydrogen target and determining the efficiencies and acceptances of each detector and analysis step. The neutron acceptance and efficiency calculation has already been discussed in its own section (see Section 4.3). This section discusses some of the remaining corrections that were used in final cross-section normalization.

4.5.1 Incident-Beam Measurement

The scaler readout of the object scintillator was used to monitor in the incoming beam. The measured rate varied between 2 and 3 MHz throughout the experiment. To determine the total number of particles incident on the scintillator in each run, the averaged measured rates were averaged together and multiplied by the length of the run. This gave a run-by-run tracking of the number of incident beam particles during the experiment. To check the reliability of this measure, the correlation between the object scintillator rate and primary beam rate monitors like the A1900 Faraday bar were confirmed.

However, at rates that are an appreciable fraction of the cyclotron's RF frequency, the measured rate will diverge from the true incident rate. This occurs because the probability of finding more than 1 particle in a beam bunch becomes significant. If there are 2 or more beam particles in a beam bunch the object scintillator's scaler will only count once and the

measurement will be incorrect. The measured rate by the object scintillator needs to be corrected for this effect. Appendix C gives a detailed derivation of this correction, which can be given as a linear function,

$$R_{cor} = 5.6 \cdot 10^{-8} R_{object} + 0.99, \tag{4.13}$$

where R_{object} is the raw scaler measurement. This effect was corrected on a run-by-run basis and increased the rate by approximately 10-15%.

The energy loss spectrum (ΔE) in the object scintillator was also measured. This is shown in Fig. 4.24, where events with 1 and 2 particles in the beam bunch can be seen. With the clear separation between these two cases, a separate determination of the incident rate can be made. As Appendix C shows the average incident beam rate (r) is related to the ratio of single hits (S_1) and multi hits ($S_{>1}$), and the RF rate (n),

$$\frac{S_{>1}}{S_1} = \frac{r}{n}. \tag{4.14}$$

This technique confirmed the scaler measurement with the above correction to within 3%.

4.5.2 S800 Acceptance

The S800 Spectrograph has a finite acceptance in both momentum and angle. To extract a properly normalized cross section this acceptance must be taken into account. Further, since the measurement of the cross section was broken across different, partially overlapping rigidity settings these acceptances are key to understanding how to merge the settings together. Here, the case of ^{14}C, where the largest correction is required, is discussed. The full

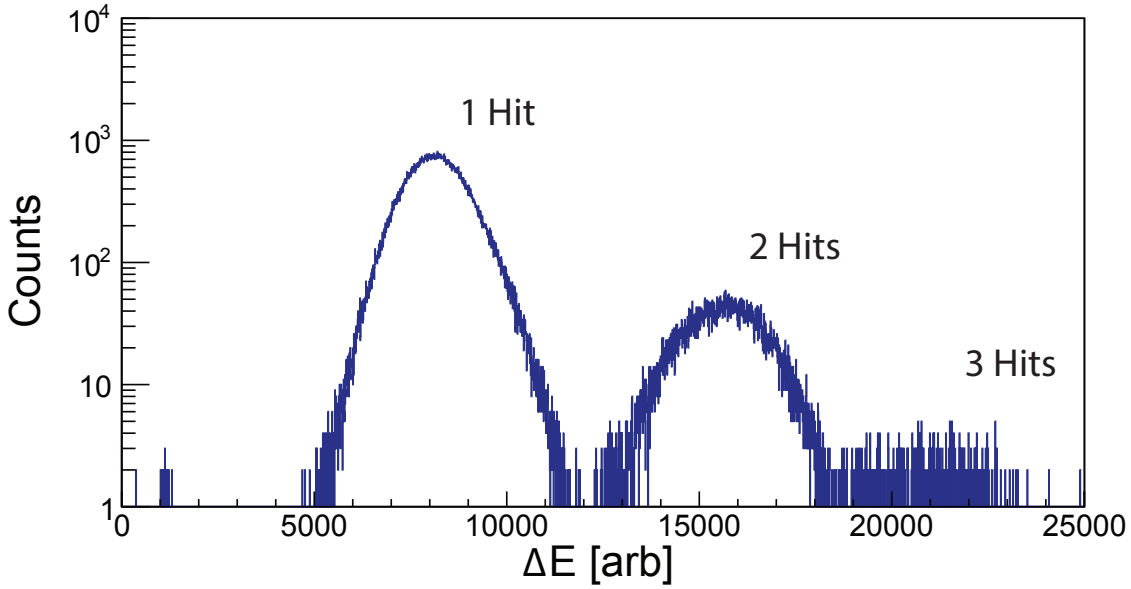

Figure 4.24: Histogram of the energy deposited in the object scintillator in the first run of the experiment. The peaks correspond to to single- and multi-particle hits in the scintillator.

kinetic energy distribution of ^{14}C is spread across 4 rigidity settings: 3.1325 Tm, 3.2828 Tm, 3.28 Tm, and 3.52 Tm. Fig. 4.25 shows a two-dimensional histogram of the kinetic energy of the ^{14}C ejectiles and the dispersive angle at the target from the 3.2828 Tm setting. The acceptance cut of the S800 is clearly visible. There is complete acceptance in the center of the distribution, but the reduced acceptance in the dispersive angle removes events on both ends of the distribution. No acceptance cuts were seen in the non-dispersive direction. To correct for these acceptance effects, the full distribution for ^{14}C was reconstructed.

Fig. 4.26 shows the full kinetic energy distribution of ^{14}C. The distribution from the 3.52 Tm setting was extended into the area of partial acceptance ($<$ 1420 MeV) by correcting for the evens cut off due to the finite angular acceptance. The same procedure was applied to the low energy side of the 3.2828 Tm setting. These regions are shown in Fig. 4.26 with vertical line shading. Between the central two rigidity settings (3.2828 and 3.38 Tm), no correction for partial acceptance was needed because the areas of full acceptance in the two

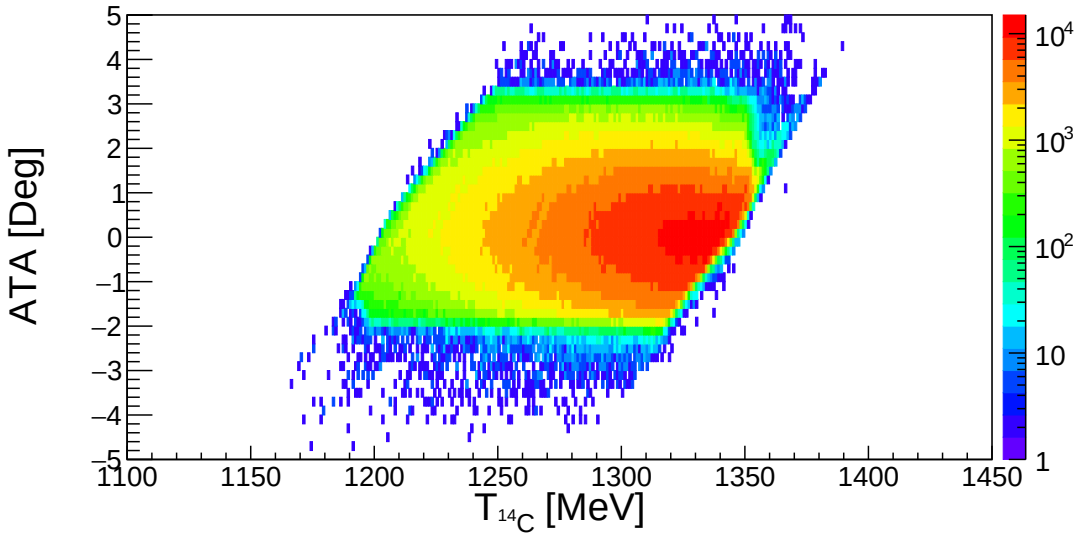

Figure 4.25: A two-dimensional histogram of the kinetic energy and dispersive angle at the target for the ^{14}C channel as measured in the 3.2828 Tm rigidity setting.

settings overlapped.

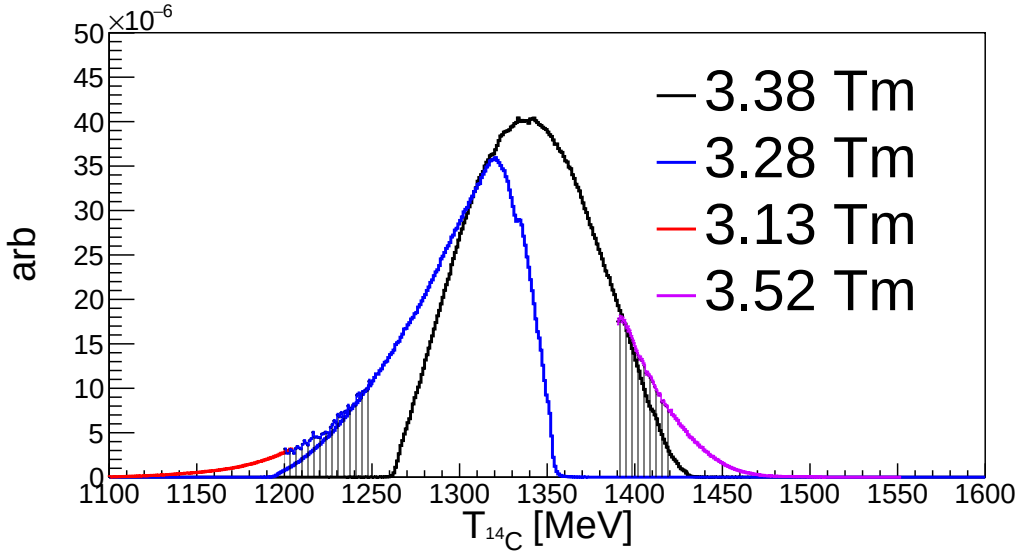

Figure 4.26: Full kinetic energy distribution for ^{14}C ejectiles reconstructed from 4 rigidity settings. The vertical line shaded regions indicate areas of incomplete acceptance. See text for details.

With the full distribution reconstructed, acceptance curves can be constructed from the data by dividing the uncorrected distribution in each setting by the total. This gives the

acceptance of the S800 as a function of kinetic energy of the ejectile. For the ^{14}C channel only the two central settings (3.2828 and 3.38 Tm) were used to extract charge-exchange information. Fig. 4.27 shows the acceptance curve for the 3.2828 Tm setting obtained in this way. The acceptance on the low-energy side of the distribution has significant statistical fluctuations since it comes from an area of incomplete acceptance.

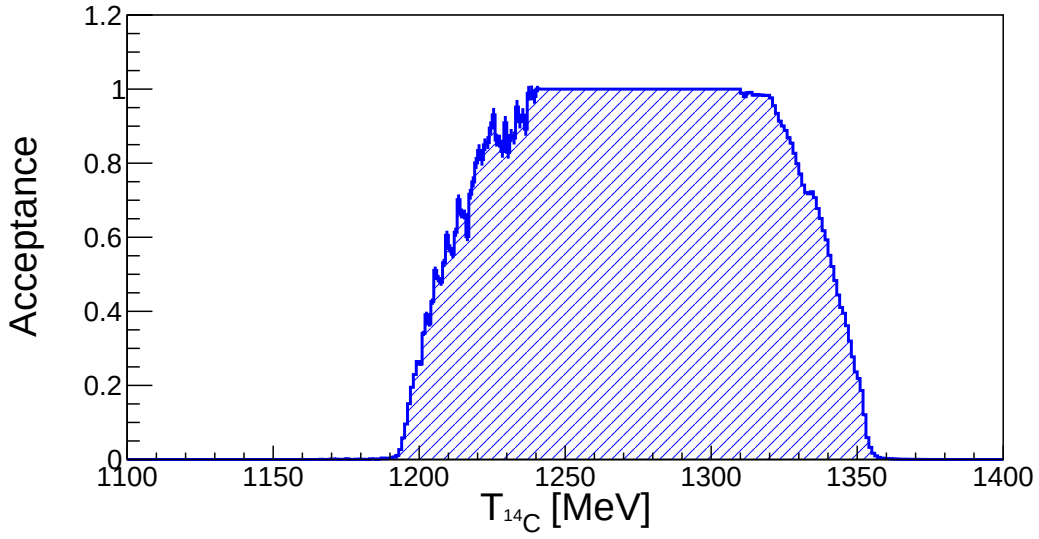

Figure 4.27: Experimentally determined acceptance curve for ^{14}C in the 3.2828 Tm setting.

The width of the ejectile's kinetic energy distribution from charge-exchange reactions is a function of excitation energy in ^{16}N. The higher the excitation energy, the more energy is available for the decaying nucleon(s) to carry away—widening the ejectile's kinetic energy distribution. To study this effect, the distribution from charge-exchange reactions needs to be known, but Fig. 4.26 gives the the distribution for background plus charge-exchange reactions. For the ^{15}N and ^{14}N channels, the charge-exchange distribution was estimated by gating around the kinematic relationships seen in Fig. 4.11. From the measured distribution a model for the neutron decay scheme was built into the Geant4 simulation to calculate excitation energy dependent acceptances for each channel. For the ^{15}C and ^{14}C channels this

was not possible since there were no clear kinematic relationships seen in the two channels. For these cases a decay scheme to the evenly spaced levels in the final nucleus was assumed. The systematic error associated with this procedure is discussed below.

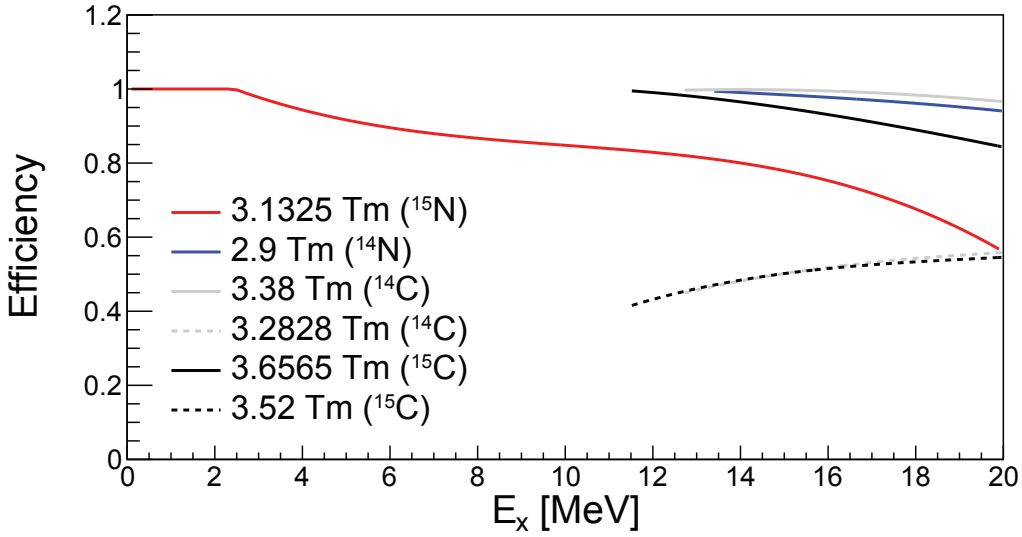

Figure 4.28: Efficiency curves from the finite S800 acceptance for each rigidity setting used in the analysis. Lines of common color show settings centered around the same detected particle in the CE reaction.

The results of these simulations are shown in Fig. 4.28, where the efficiency from the finite S800 acceptance is shown for each rigidity setting used in the analysis. The start of the lines for the higher lying channels indicates the threshold energy. Only for the ^{15}C and ^{14}C channels were there two different settings used in the analysis. For these channels the cross section was determined for each setting separately, then averaged together to form a final cross section.

As Fig. 4.28 shows, the acceptance for most of the rigidity settings was quite high in the excitation-energy regime of interest. Therefore uncertainties in the procedure to determine these corrections will have a small effect on the final cross section. The exceptions to this were the corrections for the 3.2828 and 3.52 Tm settings for ^{14}C and ^{15}C respectively. Both

of these settings corresponded to the low-energy tail of their respective channels where it was clear that there was less charge-exchange reactions below 20 MeV of excitation energy. Since this approach corrects each setting into a total cross section, the two results can be checked against one another for consistency as a measure of the systematic error of the procedure. In both cases the results were statistically equivalent, and the systematic error was deemed smaller than the statistical error.

4.5.3 Target Thickness

When filled, the windows of the liquid-hydrogen target bulged beyond the nominal 7 cm thickness of the frame. This bulging needs to be taken into account in the determination of target thickness so that the cross section can be properly determined. Originally the thickness was going to be estimated by looking at the energy loss of the ^{16}C beam going through the full and empty target into the S800 focal plane. This requires changing the rigidity of the spectrometer. However, during the analysis it became clear that the high rigidity of the 100 MeV/u ^{16}C beam put the spectrometer too close to its maximum operational rigidity and saturated the magnets (Bρ=3.94 (empty) and 3.9 (filled) Tm out of a maximum of 4 Tm). It became impossible to very accurately determine the momenta from the runs with different Bρ. To alleviate this issue the target thickness was determined by looking at the energy loss difference between the ^{16}C and the containment ^{14}B. With this approach the systematic error between the two settings from the saturation of the magnets was reduced.

Fig. 4.29 shows the raw PID spectrum from the run where the beam was tunned through the spectrometer to the focal plane. Selecting events for ^{16}C and ^{14}B and reconstructing their energy yields Fig. 4.30, where the measured kinetic energy of the two particles after traveling through the target is shown. This gives an energy loss difference of 311.7$\pm$ 0.3

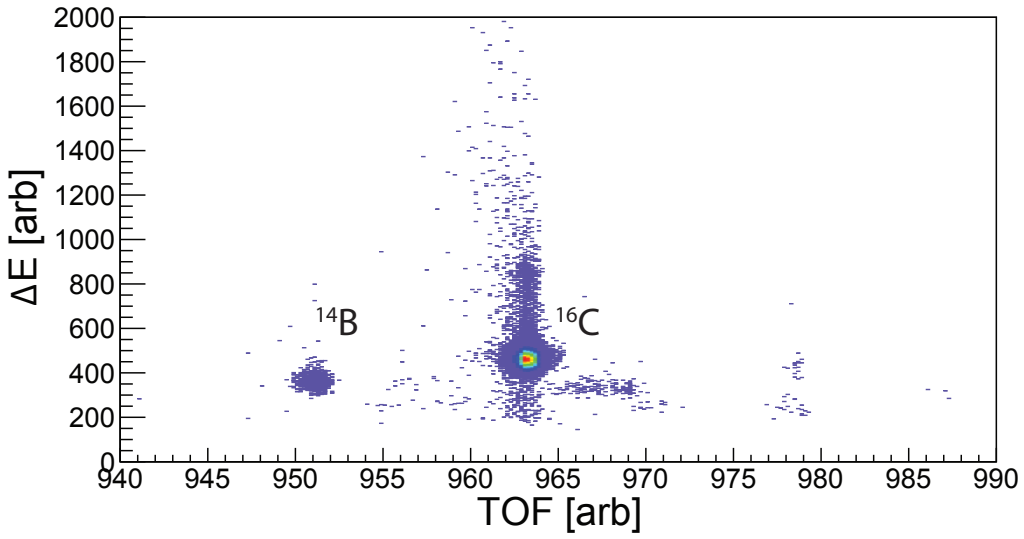

Figure 4.29: PID spectrum from the run where the ^{16}C was tuned into the focal plane of the S800. The beam consisted of ^{16}C and a small containment of ^{14}B.

MeV.

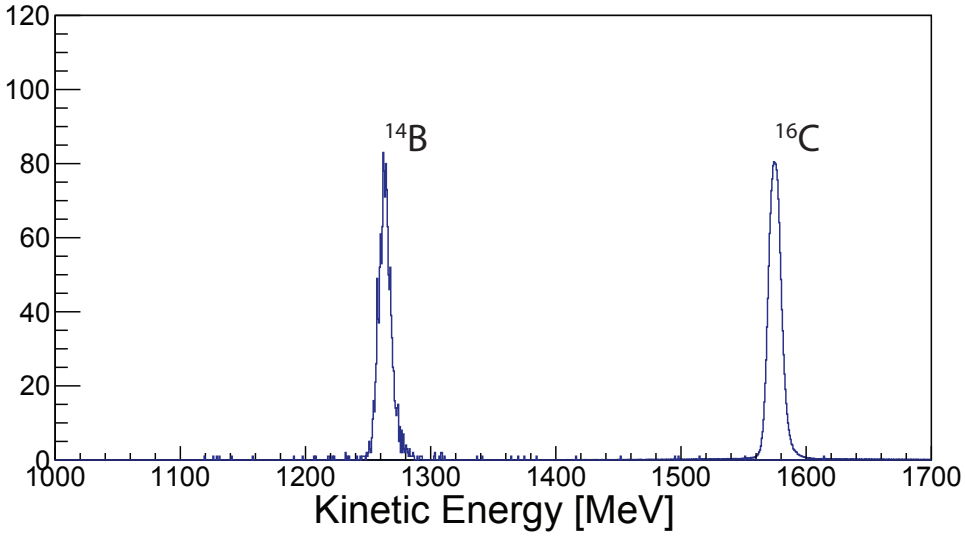

Figure 4.30: Kinetic energy measured by the s800 Spectrograph for the two beam particles. The peak from ^{16}C has been scaled down for easy comparison with ^{14}B.

With the measured energy loss difference through the target between ^{16}C and ^{14}B, the Geant4 simulation was used to determine a relationship between the target thickness and

energy loss difference. This was done with the full simulation including the bulged surface of the target and the realistic beam profile determined from the data. A different simulation was run for both particles for a range of target bulge values. The result of these simulations is shown in Fig. 4.31, where a clear linear relationship is seen. From this relationship a half bulge amount of ∼1.0 mm was found, giving a total target thickness of 9.1 ± 0.3 mm.

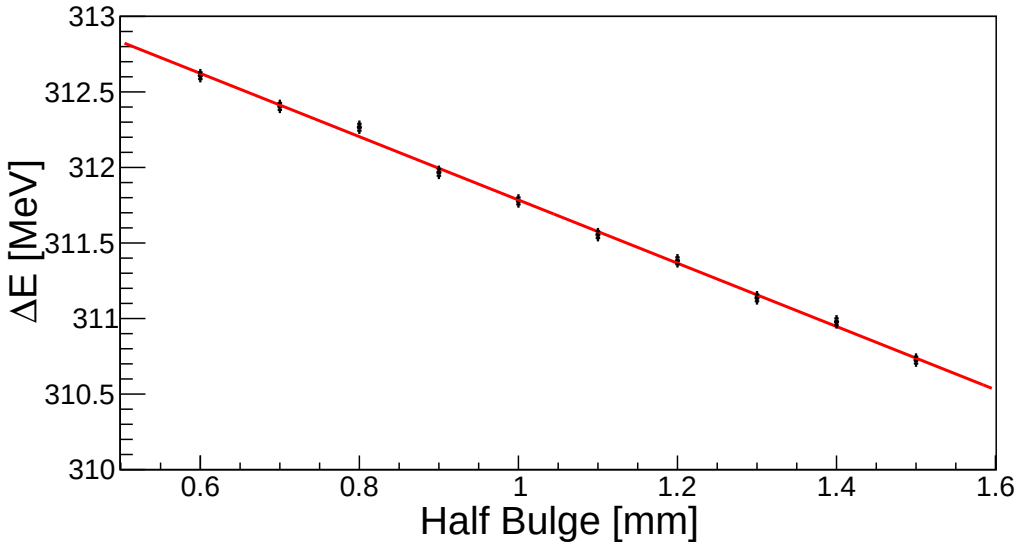

Figure 4.31: Relationship between energy loss difference and liquid hydrogen target thickness determined from simulation. The points are simulated values and the red line is a linear fit.

The curved surface of the target and the finite extent of the beam spot must also be taken into account. An average thickness over the width of the beam spot (∼3.9 mm FWHM) was calculated from the amount of bulging and the size of the beam. This reduced the effective target thickness by an amount substantially less than the 0.3 mm error bar. This corresponds to an aerial density of 65.8 ± 2.2 mg/cm^2.

4.5.4 Target Density Variations

The temperature and pressure of the liquid hydrogen target were monitored throughout the experiment so that any changes in the density could be taken into account in the final cross section normalization. The density was determined from the temperature according to the following expression,

$$\rho^{H}_{for LH_2} = -0.0008T^4 + 0.0672T^3 - 2.1467T^2 + 29.219T - 65.934, \tag{4.15}$$

where T is the temperature in Kelvin [104]. Fig. 4.32 shows the density measurements averaged over each experimental run. The fluctuations are small ($< 0.5\%$) and are corrected on a run-by-rub basis.

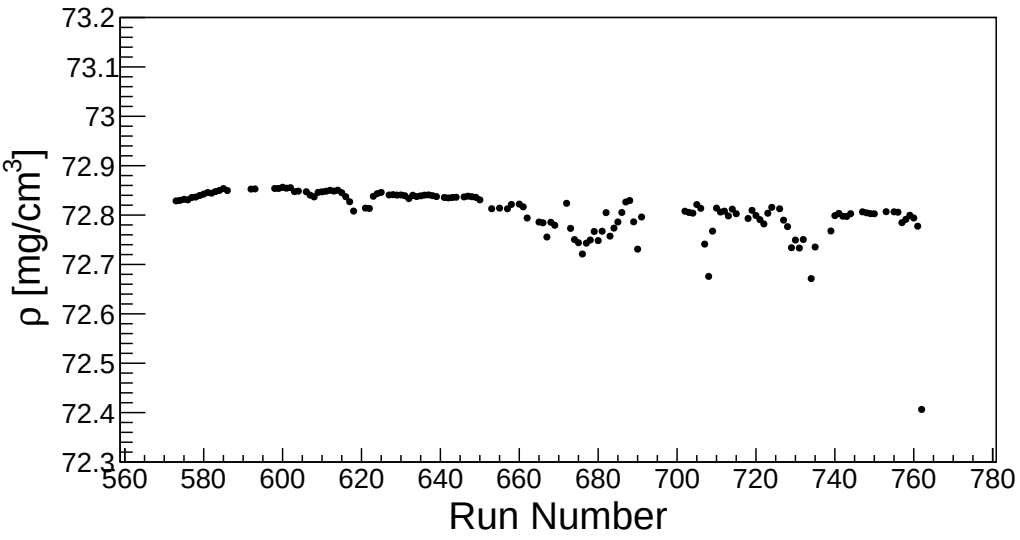

Figure 4.32: The density derived from the temperature measurement of the liquid hydrogen target for each experimental run.

4.6 Cross Section Calculation

In addition to the corrections discussed in the above sections, there are other run-by-run corrections for various detectors and other overall normalization corrections. These factors are shown in Equation 4.16 and summarized in Table 4.2. With these many effects, the absolute differential cross section can be extracted. For e10003 the full definition for the differential cross section, containing all efficiency factors and corrections is,

$$\frac{d\sigma}{d\Omega} = \frac{N_s(1+\alpha)}{\Delta\Omega 10^{-24}\rho^* \epsilon_{daq}\epsilon_{ndectors}\epsilon_{tof}\epsilon_{pid}\epsilon_{crdc}\epsilon_{IC}\epsilon_{nhit}\epsilon_{s800}T_{run}\epsilon_{trans}R_{cor}N_T}[b/sr], \quad (4.16)$$

where N_s is the number of scattered particles from charge-exchange reactions in a given COM scattering angle bin, $\Delta\Omega$ (sr) is the solid angle coverage of that bin, T_{run} (s) is the length of the run, $\epsilon_{ndetectors}$ is the neutron detection efficiency, and R_{cor} $(1/s)$ is the corrected incident beam rate described in Section 4.5.1. N_T $(1/cm^2)$ is the number of target nuclei from the liquid hydrogen and the small contribution from the hydrogen in the cell's Kapton foils given by,

$$N_T = \left(\frac{\rho^H_{LH_2} t_{cell} N_A}{MM_H} + \frac{\rho^H_{kapton} t_{foil} N_A}{MM_H} \right), \quad (4.17)$$

where t_{cell} is the target thickness, t_{foil} is the thickness of the Kapton foils (250 μm), N_A is Avogadro's number, MM_H is the molar mass of hydrogen, and ρ^H_x is the density of hydrogen in either liquid hydrogen or kapton. The remaining factors, their descriptions, and their approximate values are summarized in Table 4.2. The following paragraph gives a brief explanation of how each of these corrections was obtained.

The DAQ live time (ϵ_{daq}) was determined from the ratio of the S800's live and raw clocks. Though the singles rate in the S800 focal plane was high (∼10k), the coincidence

condition with the neutron detectors brought live trigger rate down substantially—decreasing the overall dead time of the system. The PID TOF efficiency (ϵ_{tof}) adjusted for the number of events when the correct beam bucket could not be found in the digitized waveform of the object scintillator signal. This timing signal was needed for the PID, so events lacking the signal were discarded. The PID gate efficiency (ϵ_{pid}) was the 2σ radius of the PID gates. The CRDC efficiency (ϵ_{crdc}) was determined by comparing the number of hits in the IC to hits in the CRDCs for a given run. The IC pile up efficiency (ϵ_{IC}) was found by inspecting the number of events in the high-energy tail of the IC distribution for a given particle. It was found to be constant across different runs and detected particles. The single neutron hit efficiency (ϵ_{nhit}) was found by examining the neutron multiplicity spectrum. Only events in which 1 neutron was detected could be used in the analysis so higher multiplicities were discarded. The correction was found to be constant across the different rigidity settings. The beam transmission (ϵ_{trans}) from the object scintillator to the target position was measured at the beginning (77.5%) and end (82.3%) of the experiment by tuning the beam into the S800 focal plane. The increased transmission seen in the second measurement was applied to runs 631 and above. A jump in the cross section measurement was observed at run 631, motivating the use of the second transmission measurement. The object pile-up correction (α) was found by counting the number of multi-hit events in the object scintillator. Only events that deposited energy consistent with 1 particle in the object scintillator were used in the analysis. The timing resolution for the multi-particle hits was poor and so were discarded.

Factor	Description	Value
ϵ_{daq}	DAQ live time	90-96%
ϵ_{tof}	PID TOF efficiency	90-95%
ϵ_{pid}	PID gate efficiency	95%
ϵ_{crdc}	CRDC efficiency	50-70%
ϵ_{IC}	IC pileup efficiency	98%
ϵ_{nhit}	Single neutron hit efficiency	93%
ϵ_{trans}	Beam transmission to target	77.5,82.3%
α	Object pileup correction	8-40%
ρ^*	Target Density Correction	¡0.5%

Table 4.2: Summary of corrections to the cross sections. Parameters with a range in values indicate that a run-by-run correction was performed. See text for details on how each correction was determined.

Fig. 4.33 shows charge-exchange differential cross section calculated from Equation 4.16. The cross section is shown for the $\Theta_{cm} = 4-6^{\circ}$ and $\Theta_{cm} = 14-16^{\circ}$ bins, with the contribution from each decay channel shown. From the higher-resolution spectrum at forward angles, it is clear that the (p,n) reaction in inverse kinematics can give detailed structure information. The two known states from β decay at 3.3 and 4.3 MeV are resolved and can be identified. Alongside the low-lying structure information the response up to high excitation energy is mapped out. The error in the total cross section for excitation energies above $\sim$12 MeV increases with the opening of the other decay channels, where the statistical and systematic uncertainties are increased.

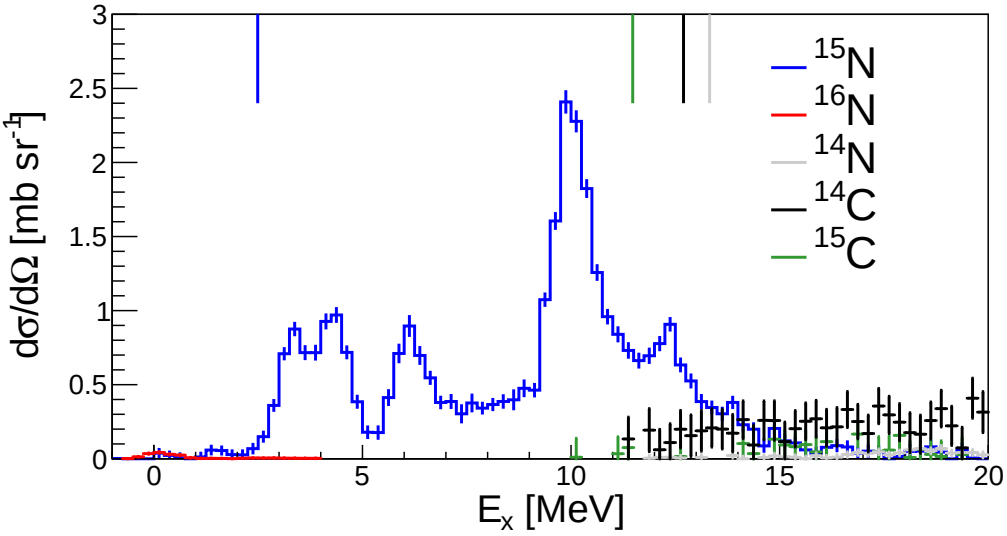

(a) Θ_{cm} =4-6°

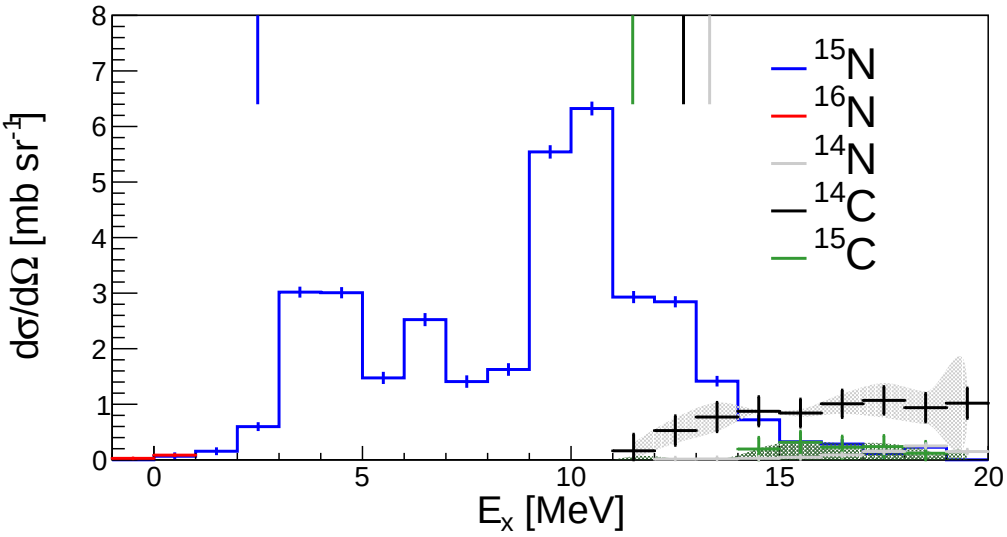

(b) Θ_{cm} =4-6°

Figure 4.33: Differential cross section for the ^{16}C(p,n)^{16}N reaction showing the contributions from each reaction channel. Panel (a) shows the cross section at forward angles in 250 keV bins. In (b) the same angle is shown with a coarser binning to highlight the channels at higher excitation energy, where the statistics is low. The most backward angle, with the poorest resolution, is presented in (c). The shaded bans in (b) and (c) indicate the systematic error estimation from the background subtraction for the ^{15}C and ^{14}C channels. The small vertical lines on the top of each figure indicate the threshold energies for the ^{15}N, ^{15}C, ^{14}C and ^{14}N channels. The color of the line matches the color of the data to indicate the channel.

Figure 4.33: cont'd

(c) Θ_{cm} =14-16°

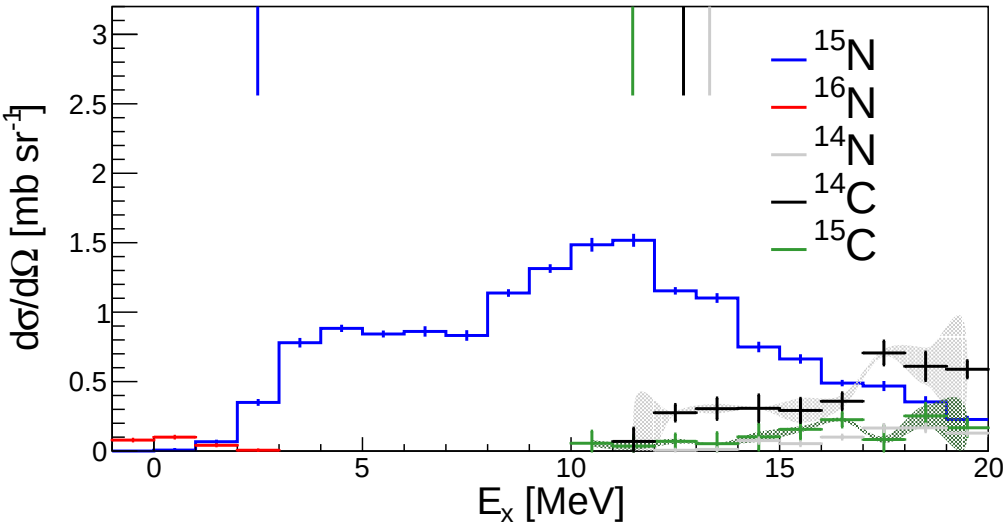

Fig. 4.34 presents the total cross section for the $\Theta_{cm} = 4 - 6°$ and $\Theta_{cm} = 14 - 16°$ bins. The systematic error from the background subtraction and uncertainty in the neutron acceptance is shown as a green band. Section 4.7 gives more details about the systematic error estimation.

4.7 Systematic Error

No absolute cross-section measurement is complete without an estimate of the systematic errors. Table 4.3 gives a breakdown of the major systematic errors in experiment e10003. Systematic error in the extracted differential cross section can either give an overall uncertainty in the normalization, or create a more complex uncertainty, like in the case of the background subtraction. The systematic error from the background subtraction is not included in Table 4.3 since it is treated as a function of COM scattering angle and excitation

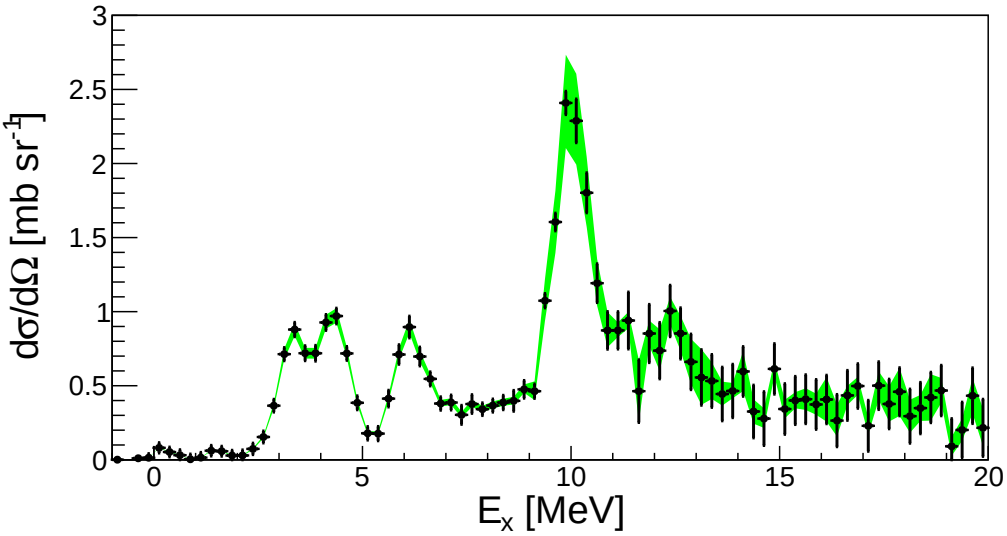

(a) Θ_{cm} =4-6˚

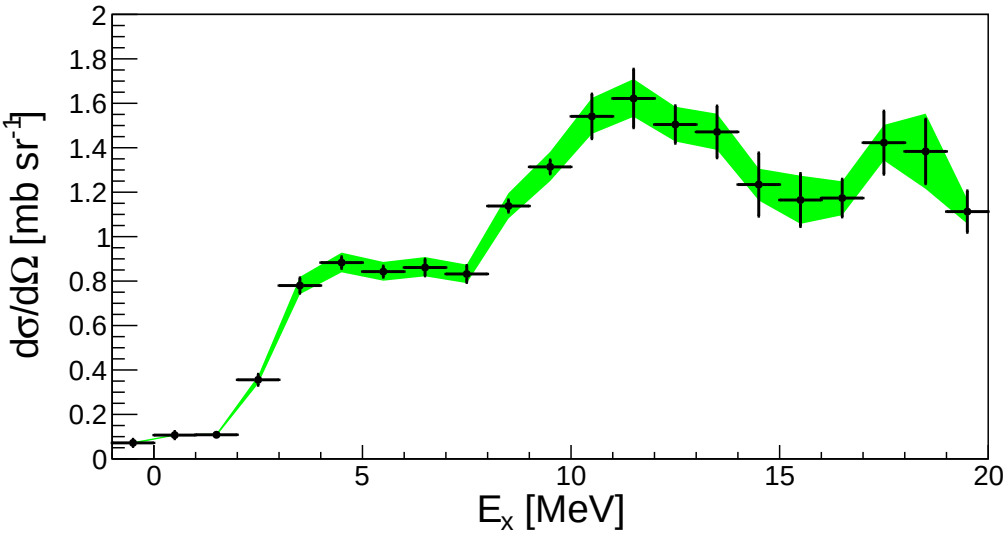

(b) Θ_{cm} =14-16˚

Figure 4.34: Total differential cross section from all decay channels in the ^{16}C(p,n)^{16}N reaction. The green band shows the systematic error including the systematic error from the background subtractions in the different channels and the systematic error in the neutron acceptance determination.

energy. Details of the estimation technique for each of the systematic errors are given in the following paragraphs.

Source	Estimate
Incident rate determination	15.6%
Background subtraction	See text
Neutron Acceptance	5%
Target Thickness	3.3%
Neutron Energy Threshold	1.8%
Random Background	$< 1\%$
Empty cell induced background	$< 0.5\%$
Total	16.8%

Table 4.3: Summary of the source and estimated size of the major systematic uncertainties in the ^{16}C(p,n)^{16}N measurement. See text for details on each source of systematic uncertainty

The largest systematic error was in the incident beam rate normalization procedure. This error was estimated by looking at the total charge-exchange cross section from 0-20 MeV for each ^{15}N experimental run. If the normalization was perfect, each run should give statistically equivalent values. Therefore, the spread seen between the runs will give an estimate of the uncertainty in the incident beam rate measurement. These integrated cross sections are shown in Fig. 4.35. The rigidity setting appropriate for detecting ^{15}N (3.1325 Tm) was measured three times during the experiment, so the large gaps between the points correspond to the runs when the other rigidity settings were measured. From this plot a FWHM systematic error of 15.6% for the normalization procedure was estimated.

Unlike the beam normalization, the background subtraction affects the shape of the extracted cross section. To estimate the uncertainty in the subtraction, the background

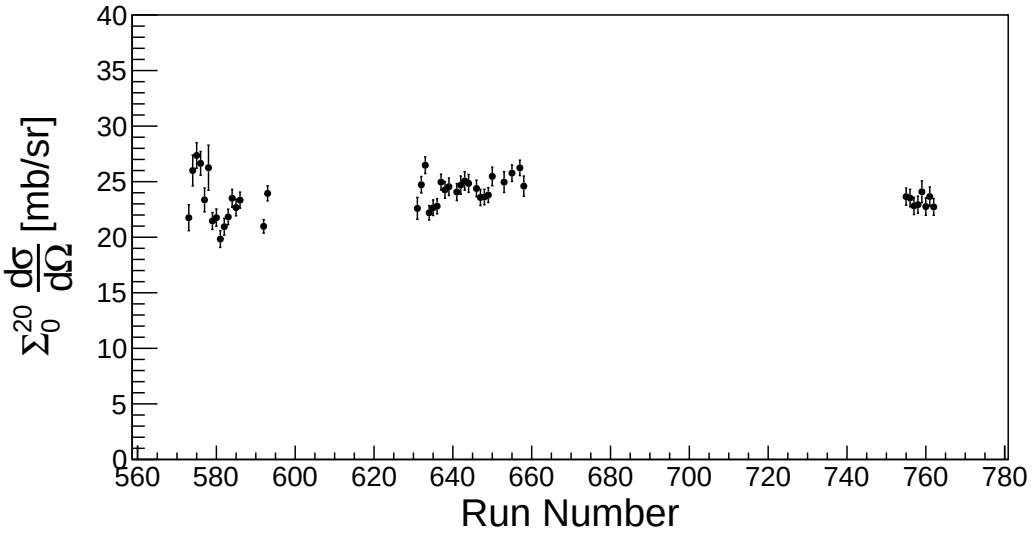

Figure 4.35: The total charge-exchange cross section from 0-20 MeV for each experimental run for the ^{15}N channel. The spread in the points gives an estimate of the uncertainty in the beam normalization.

model was varied for each rigidity setting—giving a bin-by-bin estimate of the uncertainty. For the neutron-decay channels (^{15}N and ^{14}N), this involved varying the integration ranges used to find the scaling functions shown in Fig. 4.20. This indicated that the error from the background subtraction in the regions of interest was small ($\sim 4\%$). For the proton-decay channels (^{15}C and ^{14}C), the uncertainty was higher. A similar procedure was followed to estimate the uncertainty where the different background models were compared. For ^{15}C the portion of the low-energy tail of ejectile kinetic energy distribution that was used to model the background was varied. For ^{14}C a separate background model using events that created ^{12}C was compared with the technique used above. This gave an uncertainty that varied from 10-30% depending on angle and excitation energy.

The error in neutron acceptance comes from uncertainty in the exact positions of the neutron detectors. As Fig. 4.18 showed, the neutron acceptance is not a smooth function, so small changes to the angles of the neutron detectors can change the acceptance significantly.

During the analysis process small adjustments were made to the positions of the neutron bars to correct for any unphysical discontinuities seen in the excitation energy spectrum. The size of these adjustments gave a scale to vary the angles in the estimation of this systematic error. The Geant4 simulation was used to propagate the variations in detector angle to the simulated yield in each COM bin. This gave a relatively flat change of 5%, except for the bins in excitation energy from 9-11 MeV at forward angles. There the spectrum is particularly sensitive to the position of the bars because of the steepness of the kinematic lines. An additional 8% systematic error was added to these bins.

The error in the target thickness determination was already discussed in Section 4.5.3. The error comes from the uncertainty in the energy loss difference between ^{16}C and ^{14}B. This error was estimated by comparing the shape of the measured distribution for the two nuclei.

The error due to uncertainties in the neutron detection threshold were estimated in a similar way using the Geant4 simulation. The error in the threshold was determined by comparing the neutron detector gain calibrations before and after the experiment. The gain at the end of the experiment had decreased by approximately 9%, lowering the yield. This error was combined with any fitting uncertainties in the gain calibration and propagated through the full Geant4 simulation of the setup. This showed a 1.8% change to the neutron yield.

The systematic error associated with the random and cell backgrounds were already discussed in Section 4.4 and are placed in Table 4.3 for convenience. As indicated in Table 4.3 these systematic errors combined to give a total systematic error of 16.8%. The final systematic error bands presented in chapter 5 are a combination of the systematic error from the background subtraction and the 16.8% error in the overall normalization.

Chapter 5

Results

The trick is to just look at the question and write down the answer.

Works every time

This chapter gives the results of the ^{16}C(p,n)^{16}N reaction at 100 MeV/u. The differential cross section is used to form angular distributions, needed to perform a multiple decomposition analysis (MDA). The MDA isolates the different ΔL components of charge-exchange cross section so that GT strength and dipole cross sections can be extracted.

5.1 Angular Distributions

Angular distributions (differential cross section ($\frac{d\sigma}{d\Omega}$) as a function of COM scattering angle) are formed from the experimental cross section data. To make these distributions for each excitation energy bin, the cross-section data was separated into 2 degree angular bins from 4 to 16 degrees in the COM. The bin from 0-2 degrees was below the neutron detection threshold. The bin from 2-4 degrees was excluded due to the large amount of low energy neutron background, which could not be subtracted reliably. Angles beyond 16 degrees in the COM were not used in the analysis.

As discussed in Section 4.3, the excitation-energy resolution worsens at larger scattering angles. To correctly form angular distributions, the data at forward scattering angles must

be smeared to match the excitation-energy resolution at the most backward scattering angle used in the analysis. Fig. 5.1 shows an example of this smearing procedure. The figure shows the same data at $\Theta_{cm} = 4 - 6$ ° as Fig. 4.34, but with additional smearing to match the excitation energy resolution for the Θ_{cm} =14-16° bin.

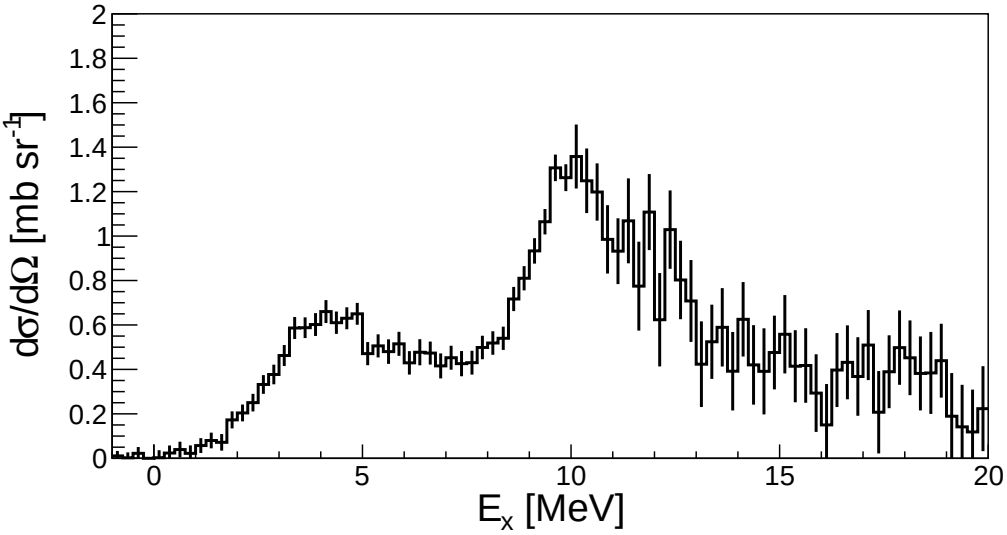

Figure 5.1: Differential cross section for the ^{16}C(p,n)^{16}N reaction as a function of excitation energy. Data is from Θ_{cm} =4-6° but smeared to match the resolution at Θ_{cm} =14-16°.

5.2 Multipole Decomposition Analysis

A multipole decomposition analysis is used to separate the different angular momentum transfer components of the cross section. The smeared angular distributions are fit with a linear combination of theoretical cross sections calculated in DWBA,

$$\left(\frac{d\sigma}{d\Omega}\right)_{total} = a\left(\frac{d\sigma}{d\Omega}\right)_{\Delta L=0} + b\left(\frac{d\sigma}{d\Omega}\right)_{\Delta L=1} + c\left(\frac{d\sigma}{d\Omega}\right)_{\Delta L=2}, \tag{5.1}$$

where a, b, and c are the fitting parameters. The fitting was done through χ^2 minimization, where the error bars in the angular points came from a combination of the statical error and the systematic uncertainty from the neutron detector acceptance. For each ΔL component, the shape of the angular distribution is represented by a characteristic DWBA calculation. Section 2.4 gives details on the cross-section calculations and presents the characteristic angular distributions used in the MDA. The result of the MDA is shown in Fig. 5.2. Angular distributions in 1 MeV bins of excitation energy were prepared from the smeared excitation energy distributions and fit according to Equation 5.1. Good agreement between the fits and the data is seen. Of specific interest is the success of the fits in first bin (0-1 MeV), where a reduced χ^2 of 1.09 is achieved. Between 0 and 1 MeV there are only expected to be 4 negative parity states at 0.0, 120, 298, and 397 keV. Starting from a ^{16}C ground state of 0^+, transitions to these states must all be ΔL=1. This is confirmed by the MDA. It is clear from the remaining fits that much of the data is strongly $\Delta L = 0$ in nature.

It is important to note that the ability of the MDA to distinguish between ΔL=1 and ΔL=2 is limited. Over the angular range used in the analysis the angular distributions for ΔL=1,2 transitions are similar. To explore this sensitivity, decompositions including only ΔL=0,1, and only ΔL=0,2 were compared with the full fit. In both cases, the portion of the distribution coming from GT type transitions did not change significantly. The fits without ΔL=1 were of a similar quality to the fits without $\Delta L = 2$, yet the full fit strongly prefers the ΔL=1 component. Given this, all three components were used in the final analysis, but with the understanding that differentiating ΔL=1 and 2 is difficult.

Fig. 5.3 shows the ΔL components of the cross section in each angular bin as determined by the MDA. As expected from the theoretical calculations, the dipole component peaks at the backward angles and appears at high excitation energy. In the 14-16° bin, there is

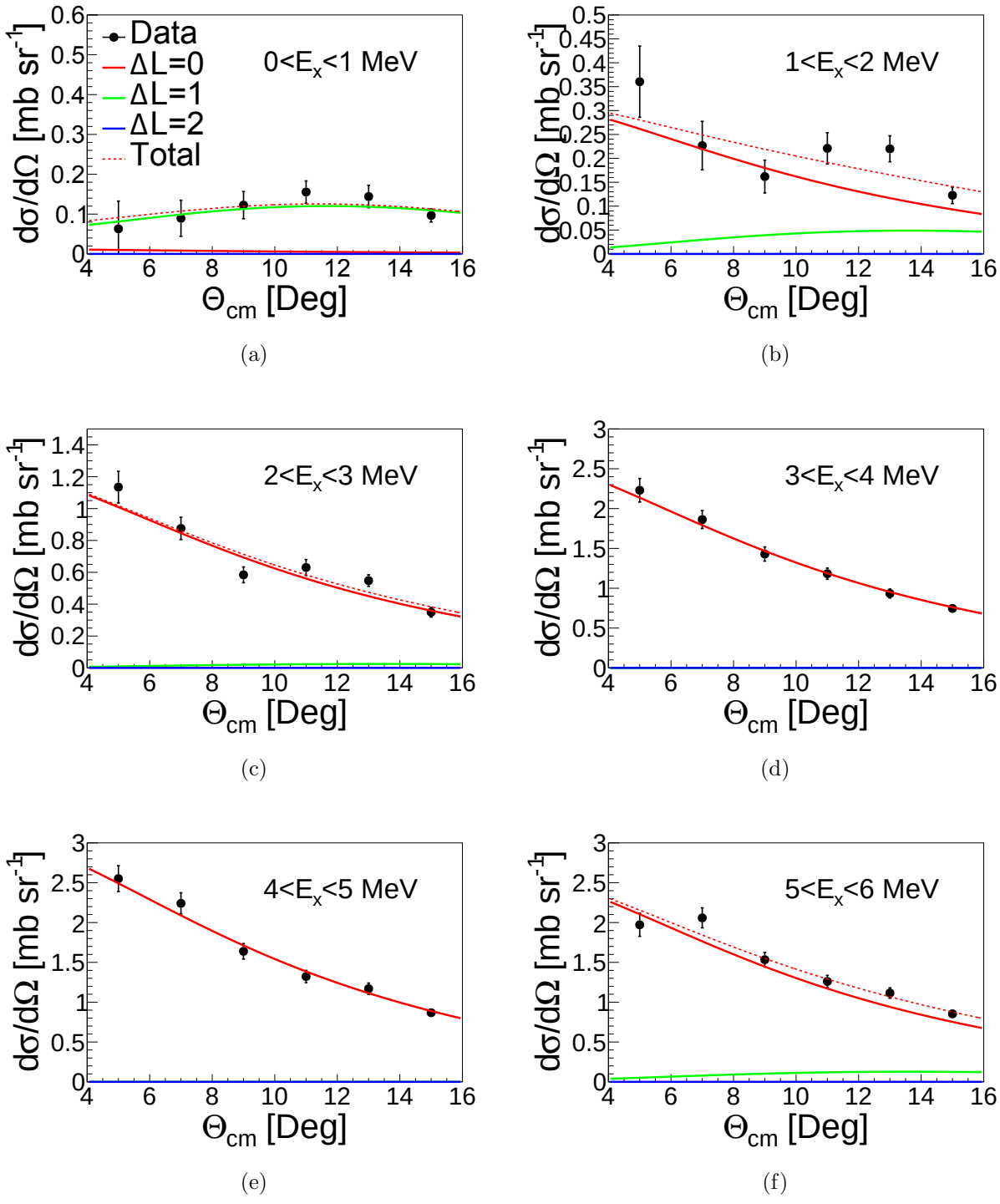

Figure 5.2: Measured COM angular distributions in 1 MeV bins from 0-20 MeV in ^{16}N. The black dots are the experimental data. The red, green, and blue lines are the ΔL=0,1,2 components of each fit determined from the MDA. The dotted line is the sum of the 3 MDA fit components.

Figure 5.2: cont'd

(g)

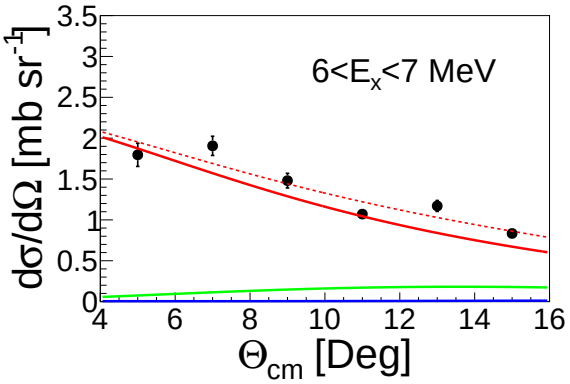

(h)

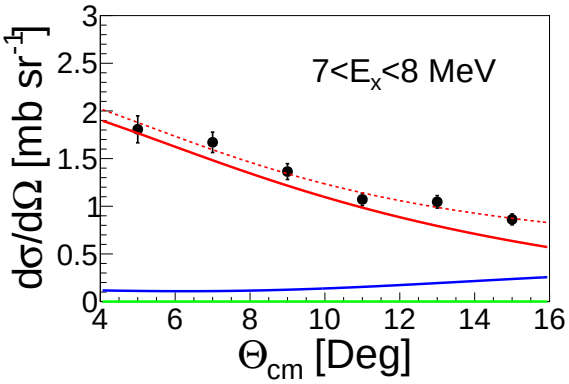

(i)

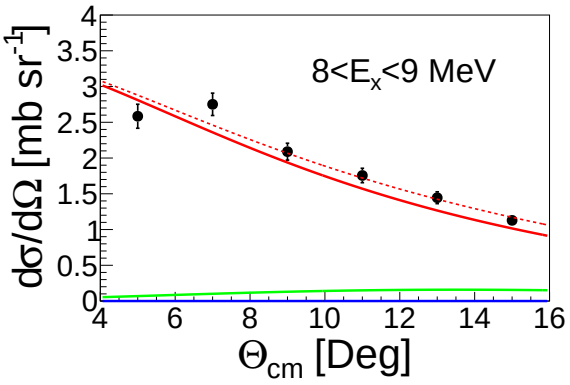

(j)

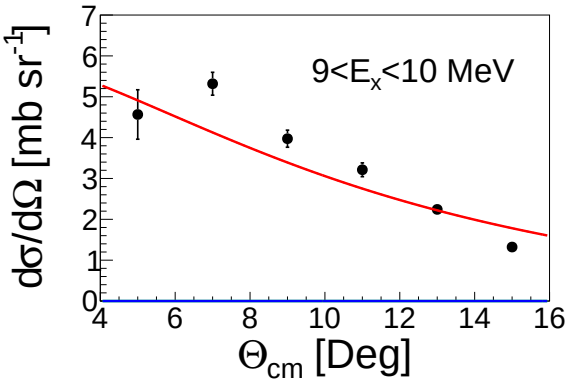

(k)

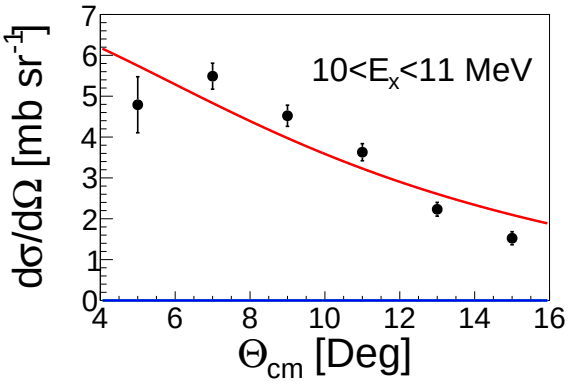

(l)

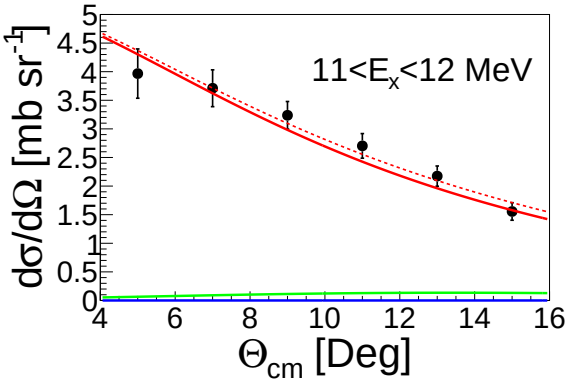

Figure 5.2: cont'd

(m)

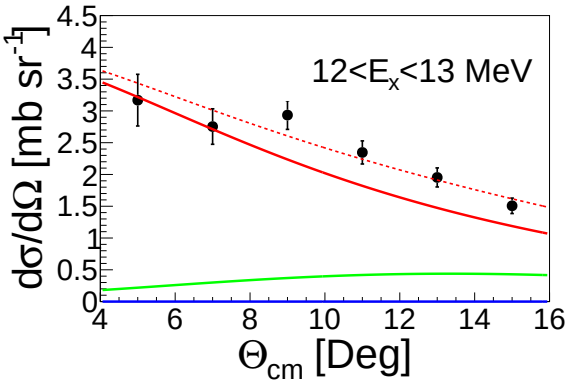

(n)

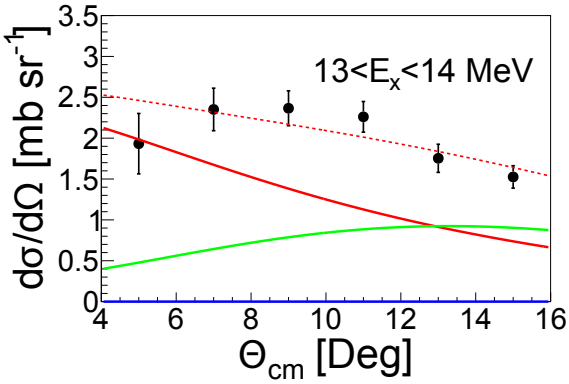

(o)

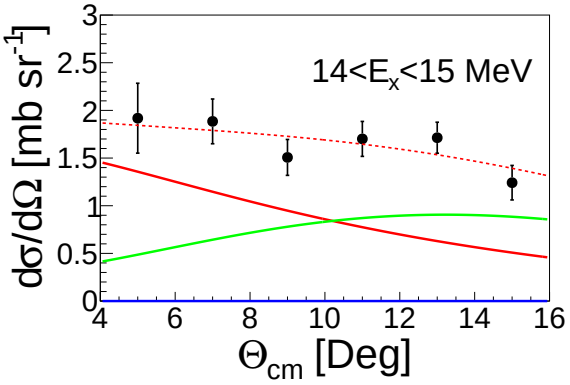

(p)

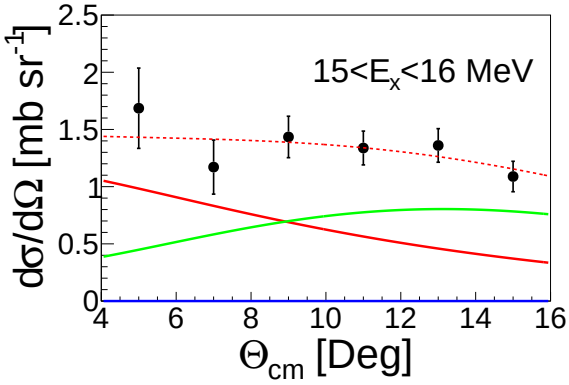

(q)

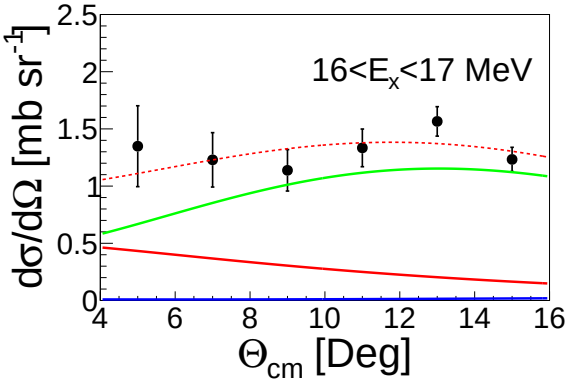

(r)

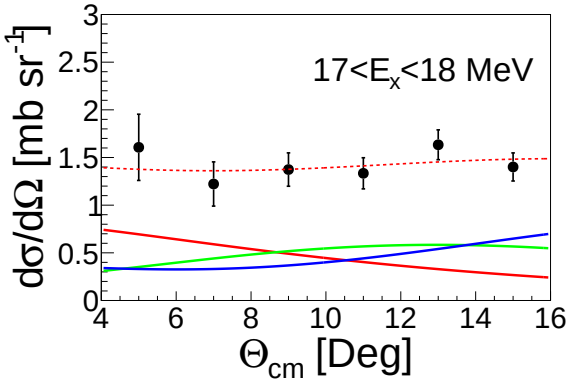

Figure 5.2: cont'd

(s) (t)

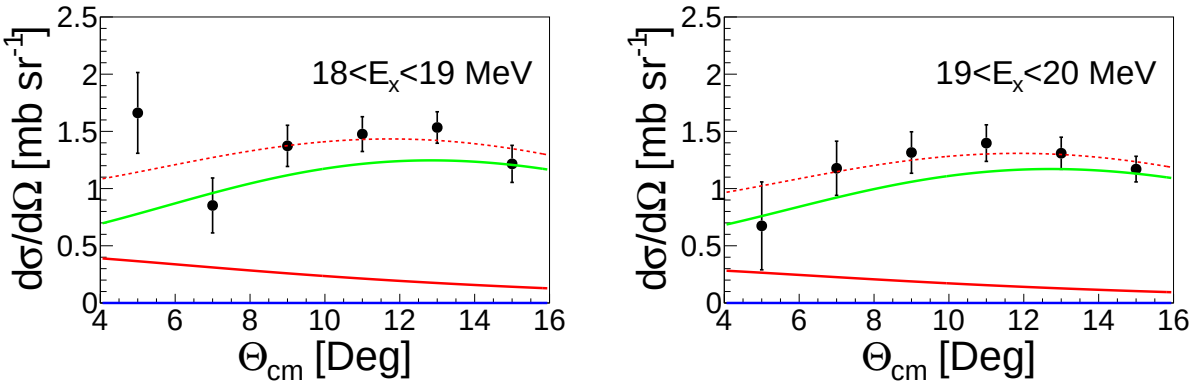

significant dipole strength above ∼12 MeV. Conversely, the 4-6° bin is dominated by ΔL=0 strength. This motivates directly using the cross section in the 4-6° bin, where the best excitation energy resolution is available to extract the B(GT) spectrum.

5.3 B(GT) Extraction

Knowing that the cross section is dominated by ΔL=0 transitions in the 4-6° bin, the B(GT) can be readily extracted. First the cross section must be extrapolated to zero linear momentum transfer ($q \rightarrow 0$). The MDA results are used to extrapolate the cross section to 0 degrees. Then DWBA calculations are used to extrapolate the Q value to 0 for each bin in excitation energy. With both $\Theta_{cm} \rightarrow 0$ and $Q \rightarrow 0$, the cross section is extrapolated to zero linear momentum transfer. Fig. 5.4 shows the ΔL=0 cross section after this extrapolation.

The blue histogram seen in Fig. 5.4 is a simulation of the IAS assuming full exhaustion of the Fermi sum rule. Within the ^{16}N exit channel a peak corresponding to the γ decay of the IAS was observed with a branching ratio of $0.6 \pm 0.2(stat)\%$. The peak location was determined from a calculation of the difference in coulomb energy yielding a value of

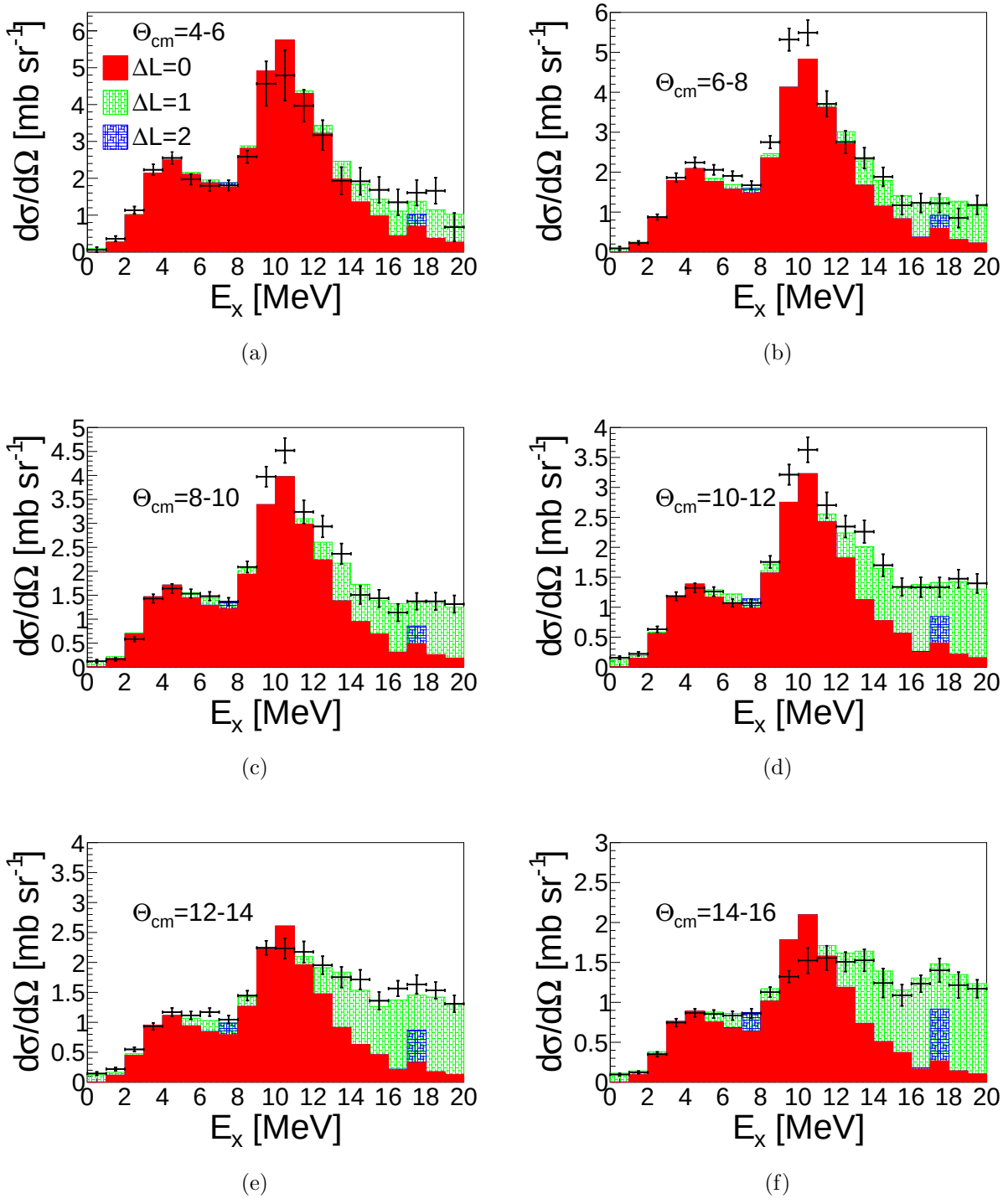

Figure 5.3: MDA results. The ΔL components of the cross section is shown as a function of excitation energy for each angular bin. At forward angles the spectrum is dominated by $\Delta L = 0$ transitions, while at backward angles $\Delta L = 1$ transitions appear at high excitation energies.

10.025 MeV. This value was consistent with the peak position seen in the ^{16}N exit channel. The detectors response to the IAS was determined in the full Geant4 simulation and was subtracted from the measured cross section.

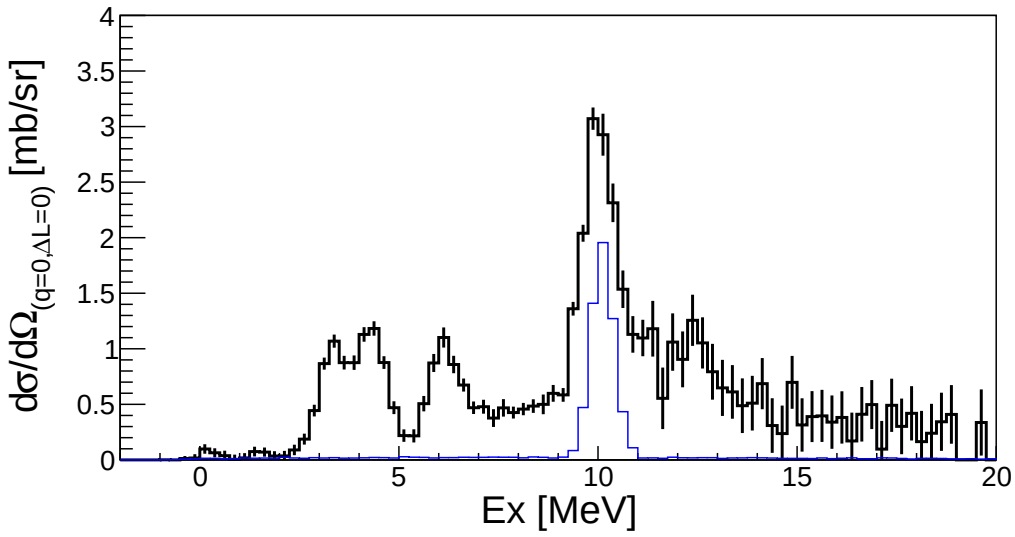

Figure 5.4: The differential cross section extrapolated to zero momentum transfer. The error bars show statistical errors. The blue peak shows the contribution from the IAS to the spectrum. See text for details.

In order to transform this into a B(GT) spectrum, a suitable $\hat{\sigma}_{GT}$ must be determined. This can be done by looking at a low-lying state that is accessible by β decay and using the known $log(ft)$ value and measured charge-exchange cross section to find $\hat{\sigma}_{GT}$. If β decay data is not available, $\hat{\sigma}_{GT}$ can be estimated from well-established mass-dependent systematics [56]. The β decay of ^{16}C has been measured previously [69, 70, 71], but as will be discussed in Chapter 6, the low-lying states have peculiar structural effects that break the proportionality. To avoid the uncertainty associated with the two low-lying states, the unit cross section was determined from nearby (p,n) measurements on ^{14}C [115, 56] and ^{18}O [116].

For the ^{14}C data, the $\hat{\sigma}_F$ was taken from two measurements at 80 and 120 MeV and

averaged to arrive to find $\hat{\sigma}_F$ at 100 MeV. It is well known that the $\hat{\sigma}_F$ varies with incident beam energy, while the $\hat{\sigma}_{GT}$ remains nearly constant [56]. From this, $\hat{\sigma}_{GT}$ was found using the empirical relationship between $\hat{\sigma}_{GT}$ and $\hat{\sigma}_F$,

$$\frac{\hat{\sigma}_{GT}}{\hat{\sigma}_F} = \frac{E_p}{55.0}, \tag{5.2}$$

where E_p is the incident proton energy [56]. This yielded $\hat{\sigma}_{GT}$=5.4 mb/sr. The ^{18}O data gave $\hat{\sigma}_{GT}$=4.2 mb/sr [116]. The average of these two measurements with a systematic error of 13% was used in the final analysis of ^{16}C: $\hat{\sigma}_{GT}$=4.82 $\pm$ 0.61 mb/sr.

Fig. 5.5 (a) shows the extracted Gamow-Teller strength distribution in ^{16}N compared with two shell model calculations using the WBT and WBP interactions in the *spsdpf* model space. The shell-model states have been smeared with the experimental resolution. States with T=1 and 2 are included in the figure. Fig. 5.5 (b) shows the corresponding sum spectrum for the data and shell model calculations. Chapter 6 will discuss this result in detail.

5.4 Dipole Strength

The data can also give some insight into dipole ($\Delta L = 1$) transitions. Dipole strength seen at this excitation energy and at this beam energy will predominately come from spin-flip transitions, so it should correspond to excitations of the isovector spin dipole giant resonance (SDR). Looking at the most backward angle (where the dipole strength is highest), the $\Delta L = 1$ component of the cross section was extracted from the MDA fits. These results are presented in Fig. 5.6. Unlike the GT strength, the spin-dipole (SD) strength does not have

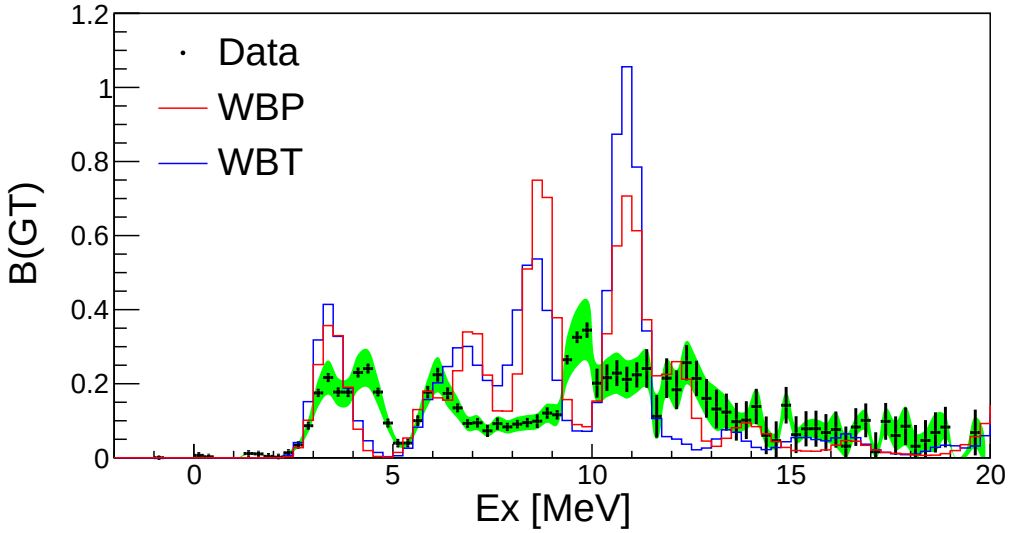

(a)

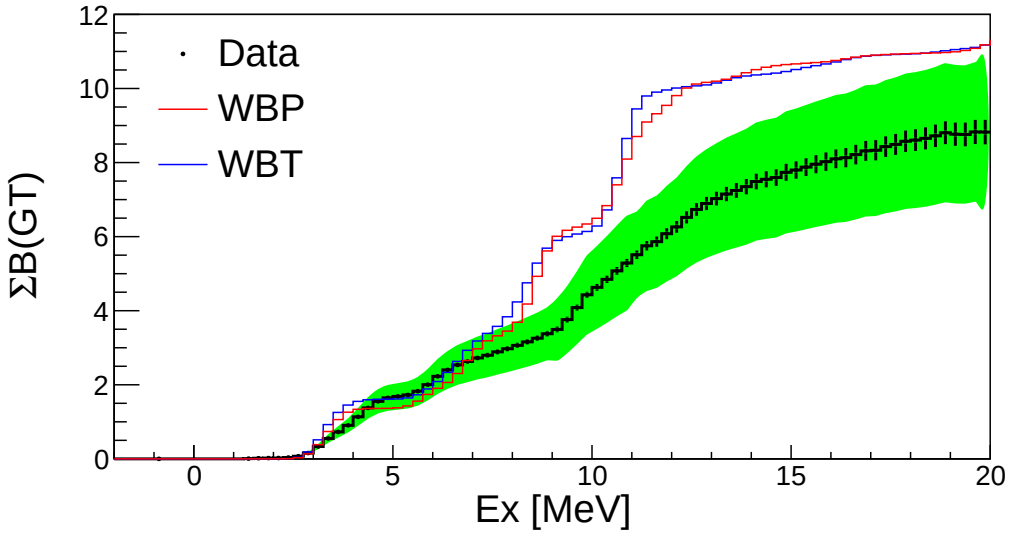

(b)

Figure 5.5: Extracted GT strength distribution (a) and summed strength (b) in ^{16}N up to E_x=20 MeV. The green band shows the total systematic error in both plots. The data is compared with two shell interactions WBT and WBP, both calculated in the *spsdpf* model space.

a well-established proportionality. Instead direct comparisons of measured cross section and DWBA based calculations are typically used. The black histogram in Fig. 5.6 shows the calculated cross section for all the dipole shell-model states discussed in Section 2.5. For each shell-model transition, the angular distribution is calculated with the program DW81 and the value at 15° is taken. These states are then smeared with the experimental resolution and histogramed.

As mentioned above, the sensitivity between $\Delta L = 1, 2$ of the MDA is limited. The significant error bars seen in the top panel of Fig. 5.6 are a result of this. The bottom panel shows the result of the MDA if ΔL=2 is excluded from the fits.

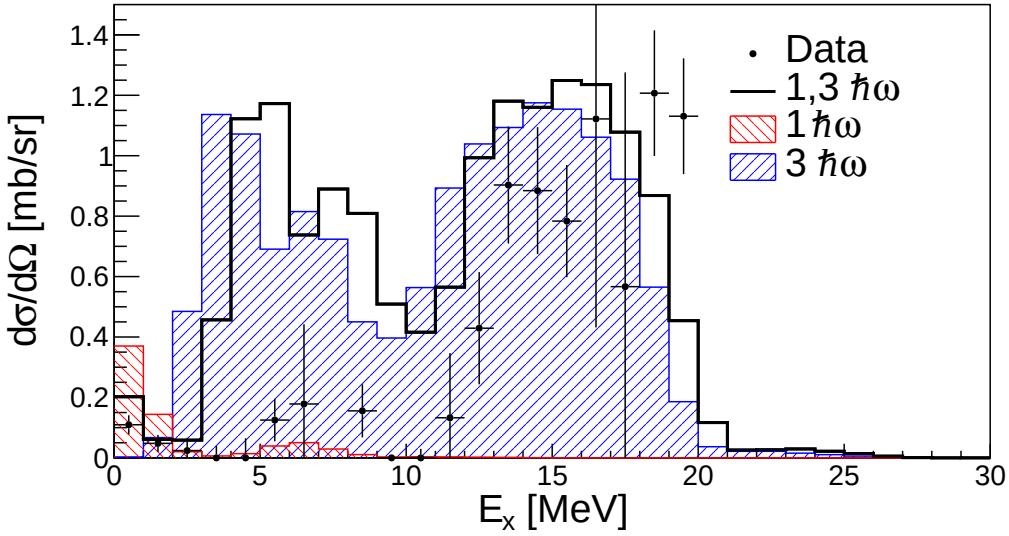

(a) Full fit

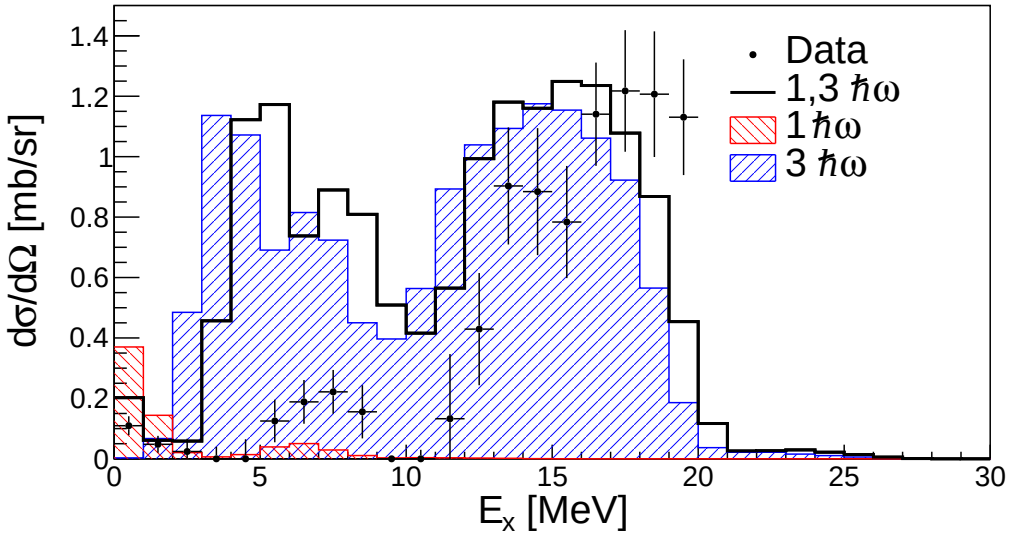

(b) ΔL=2 excluded.

Figure 5.6: The black points show the dipole ($\Delta L = 1$) differential cross section determined from the MDA at 15°. The error bars give the statistical uncertainty from the MDA fits. The black histogram gives the smeared, DWBA cross sections from the 1,3 $\hbar\omega$ shell-model calculation with the WBP interaction in the *spsdpf* model space. The blue and red histograms give the results of the calculations when pure 1 and 3 $\hbar\omega$ contributions are calculated separately. Panel (a) Shows the result when the full MDA fit is used, while (b) excludes the ΔL=2 component. The 7-8 MeV bin was excluded from (a) since its error bar was too large to be meaningful and was consistent with zero.

Chapter 6

Discussion

Everything works, Nothing is Broken

Samuel Lipschutz

6.1 The (p,n) Probe in Inverse Kinematics

Figs. 5.5 and 5.6 readily show the achievement of the main goal of e10003 and this thesis—to validate the (p,n) probe in inverse kinematics for the study of isovector giant resonances in radioactive nuclei. The full GT response and a portion of the spin-dipole resonance have been measured in a neutron-rich isotope. This technique will allow future experiments to explore the isovector response of unstable nuclei up to high excitation energy. As Figs. 5.5 and 5.6 shows, it is clearly a powerful probe, providing enough resolution to see the low-lying structure of ^{16}N, while at the same time capturing a large range of excitation energy.

Higher excitation energies and the remaining portion of the spin-dipole resonance would have been available if more particle decay channels were measured (^{13}C opens at $\sim$21 MeV). Given the finite time of the experiment and the wide momentum distributions of the multi-nucleon decay channels, a cutoff had to be made. However, for heavier systems this will be become easier as the change in rigidity from few nucleon decays becomes less severe. This will simplify the experimental procedure and analysis, since many decay channels can be fully measured in a single spectrometer setting.

6.2 Shell Model Comparison

The spectrum in Fig. 5.5 allows us to see the quality of shell-model calculations for the GT response in neutron-rich nuclei up to high excitation energies for the first time. It is clear that the details of the spectrum are not well reproduced by either of the interactions. This is a departure from previous charge-exchange data where shell-model calculations have achieved better agreement (for example, Refs. [78, 64]). In Fig. 5.5, the positions of many of the strong states seen in the spectrum are shifted from the data by several MeV. The WBP interaction does a better job at spreading the strength out in the spectrum, while the WBT interaction concentrates a large amount in the state at ∼11 MeV. However, it is important to note that the higher-lying states most likely have large intrinsic widths since the particle-decay thresholds are exceeded. Such effects are not included in the shell model—only the experimental resolution is used to smear the shell-model states. In light of this, an exact match in the shape of the spectrum is not expected. Further, the shell-model spectrum is unquenched and is expected to over predict what is seen in the data. These limitations often make the summed strength spectrum a more reliable indicator of the quality of the calculation.

The spin-dipole spectrum also gives guidance to the validity of the shell model. Presented in Fig. 5.6 is the measured ΔL=1 differential cross section in the 14-16° bin, overlaid with the cross section calculated in DWBA. The theoretical cross section is broken down into the components coming from pure 1 and 3 $\hbar\omega$ configurations in the final state. The calculations shows that the ground state comes from the 1 $\hbar\omega$ component. There is additional 1 $\hbar\omega$ strength predicted at ∼6 MeV, where an enhancement in the data is seen, but the strength is underestimated by the calculation. The 3 $\hbar\omega$ component opens at ∼4 MeV and vastly over

predicts the strength in the region. At higher excitation energy (∼12MeV and above) the calculation does a reasonable job at predicting the location and strength of the resonance.

The full calculation includes both of these components where they mix with each other. The mixing typically reduces the strength of the states, but in this case does not alleviate the issues seen in the 3 $\hbar\omega$ calculation. The full calculation still vastly over predicts the low lying strength compared to the data. Further investigation and improvements in the model are needed.

6.3 Quenching

Fig. 5.5 shows the measured, summed GT strength in ^{16}N. As discussed in Section 1.9 this experiment has given one of the first measurement of the quenching of summed GT strength in a neutron-rich, unstable nucleus. Under the assumption that the strength in β_+ direction is small due to fermi blocking, the data shows 73.5% $\pm 2.8(st) \pm 15.5(sys)$% of the model-independent sum rule up to 20 MeV. Table 6.1 shows a comparison of this result with the known quenching values in the region from charge-exchange and β decay studies. The charge-exchange studies shown in Table 6.1 give their quenching values relative to the GT sum rule, while the β-decay numbers are from comparisons to shell-model calculations.

Relative to Sum Rule		Relative to Shell Model	
System	Quenching Factor	System	Quenching Factor
^{18}O	67% [116]	p-shell	65.6% [117]
^{14}C	60% [49]	^{18}Ne	62.2±0.2% [76]
$^{16}C_{Ex0\rightarrow20}$	73.5 $\pm2.8(st) \pm 15.5(sys)$%	sd-shell	57.8% [76]
$^{16}C_{Ex0\rightarrow12}$	50.7 $\pm1.2(st) \pm 10.7(sys)$%	pf-shell	55.4% [83]
		$^{16}C_{Ex0\rightarrow12}$	61.1 $\pm1.5(st) \pm 12.8(sys)$%
		$^{16}C_{Ex0\rightarrow20}$	79.0 $\pm3.0(st) \pm 16.7(sys)$%

Table 6.1: Comparison of the quenching factors of GT strength for ^{16}C, various nearby nuclei, and adopted values for several nuclear shells. Quenching studies from charge-exchange reactions and β decay studies are presented. The p-shell factor comes from the empirical relation given in Ref. [117] with $A = 16$. See text for details.

The β-decay quenching results come from measurements of individual states. Since they are restricted by the β-decay Q-value window, they can only probe the properties of the low-lying strength. To make a fair comparison with the ^{16}C charge-exchange data, the summed strength up to the end of the main part of the resonance ($\sim$12 MeV) was compared with the shell model. This yields a quenching factor of 61.1 $\pm1.5(st)\pm12.8(sys)$%, which is consistent with the β-decay factors seen in Table 6.1. Though the systematic error is large, the 61.1% value follows the trend of decreasing quenching between the p and sd shells. As discussed in Section 1.9, the strength is thought to be pushed to higher excitation energies through several proposed mechanisms, such as higher-order configuration mixing. The charge-exchange data confirms this for ^{16}C, where 79.0 $\pm3.0(st) \pm 16.7(sys)$% is found up to 20 MeV of excitation energy in ^{16}N. This shows that about a third more strength is found at excitation energies above the GT giant resonance.

More insight into this behavior is given in Fig. 6.1, where the quenching factor relative to the shell model as a function of excitation energy is shown. After the end of the main resonance at ∼12 MeV the quenching factor steadily increases. This shows that the measured distribution is "catching up" to the calculation, which has predicted too much strength in the main portion of the resonance. The calculation does predict strength after the resonance, going all the way up to ∼ 30 MeV of excitation energy before the sum rule is exhausted. However, the data increases faster than the calculation in the measured region recovering a portion of the missing strength. With the (p,n) reaction in inverse kinematics a similar recovery of strength is seen in the neutron-rich ^{16}C as was seen in the ^{90}Zr experiment discussed in Section 1.9.

The first half of Table 6.1 compares the quenching in this measurement relative to the model-independent sum rule with ^{18}O and ^{14}C—the closest measurements where the full GT spectrum was measured through charge exchange. Here a quenching factor of 73.5 $\pm 2.8(st) \pm 15.5(sys)\%$ up to 20 MeV was found. This is consistent with the measurements on ^{18}O and ^{14}C. The number is naturally lower than the quenching factor relative to the shell model since the full sum rule is not exhausted in the shell model at 20 MeV.

6.4 The First Two 1^+ States

As alluded to earlier, there are GT proportionality breaking effects in the two low-lying states of ^{16}N. With the differential cross section and extracted B(GT) spectra shown in Figs. 5.4 and 5.5 respectively, the cross section and B(GT) values for the first two states can be determined. These values along with a breakdown of the statistcal and systematic errors are shown in Table 6.2. Table 6.3 shows a comparison of the B(GT) values from charge-

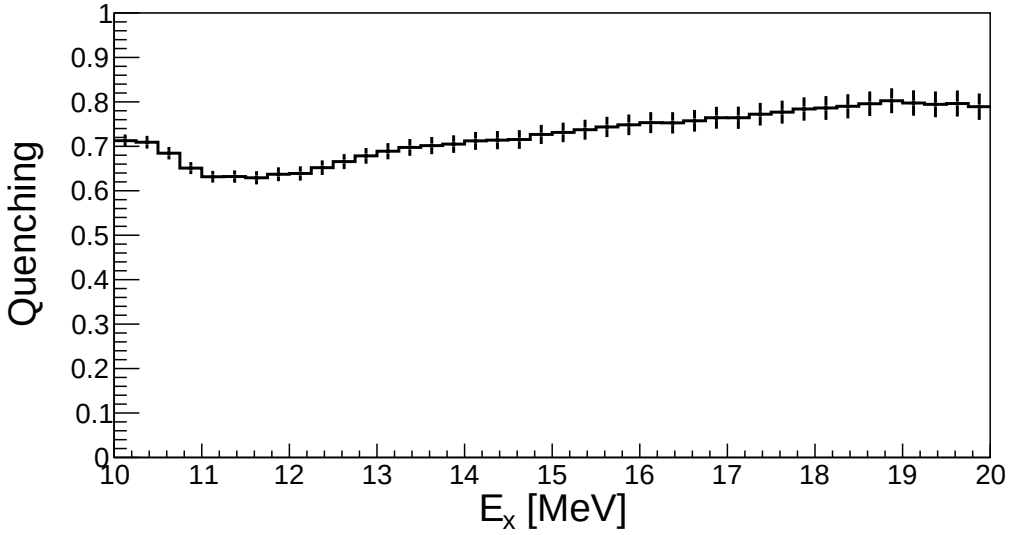

Figure 6.1: The amount of quenching between the experimental data and the shell model (WBP interaction) as a function of excitation energy.

exchange, β decay and the shell model. It is clear that the strengths of the first two states from charge-exchange and β decay are significantly different. The summed strength, however, is a near match. The predictions from the WBT interaction also do a good job at predicting the total strength, but does worse than WBP at properly recreating the individual strengths seen in β decay. Further, the separation of the two states in the shell-model calculations are underestimated: 375 keV for the WBP interaction and 625 keV for the WBT interaction versus 967 keV from the β decay data. In the following analysis the WBT interaction is used to investigate the two states.

E_x	$(d\sigma/d\Omega)_{q\to 0}$ [mb/sr]	B(GT)$_{CE}$
3.353 MeV	3.39± 0.19(st)±0.56(sys)	0.70 ± 0.04 (st) ± 0.15(sys)
4.320 MeV	4.62± 0.20(st)±0.76(sys)	0.96 ± 0.04 (st) ± 0.20(sys)

Table 6.2: Charge-exchange differential cross section at zero momentum transfer and extracted B(GT) for the first two 1^+ states in ^{16}N. A breakdown of the statistical and systematic error is shown. The systematic error for the B(GT) is increased by the uncertainty in $\hat{\sigma}_{GT}$.

E_x	B(GT)$_{WBT}$	B(GT)$_{WBP}$	$B(GT)_{CE}$	B(GT)$_{\beta}$
3.353 MeV	1.34	0.97	0.70	1.104
4.320 MeV	0.27	0.39	0.96	0.586
Sum	1.61	1.36	1.66	1.69

Table 6.3: Comparison of the B(GT) values from charge-exchange, β decay, and the shell model for the first two 1^+ states in ^{16}N.

Proportionality breaking effects in charge-exchange reactions have been seen before [78, 118]. These are often explained by interference from the $\Delta L = 2$ $\Delta S = 1$ transitions that are mediated by the tensor-τ portion of the NN interaction, which interferes with the $\Delta L = 0$ $\Delta S = 1$ $\sigma\tau$ portion. This effect is typically seen in states with small B(GT) values. The calculation of $\hat{\sigma}_{GT}$ presented in Fig. 2.5 shows this feature in ^{16}C. The spread in the calculated $\hat{\sigma}_{GT}$ values increase significantly below B(GT) values of $\sim$0.1. This spreading can be largely removed by turning off the tensor portion of the effective NN interaction.

However, the first two states are not weak. Further, the DWBA calculations with and without the tensor force included in the interaction do not show a large enough sensitivity to explain the inconsistency in Table 6.3. However, the calculation presented in Fig. 2.5 does show that the expected $\hat{\sigma}_{GT}$ for the second state is $\sim$ 52% higher than the average of the other strong states. If the unit cross section for that state is abnormally high, then the measured charge-exchange cross section should be enhanced, which is seen in the data. Since shell-model calculations are available, the details of these two states can be explored. To do this the transition densities for these two states are examined (see Equation 2.23).

Fig. 6.2 shows a typical transition density (shown as $r^2\rho$), broken down into the significant 1p-1h contributions. This transition density comes from the shell-model calculation of the 4^{th} 1^+ state in ^{16}N. As the figure shows the sum of the different 1p-1h components of

the transition gives a smooth function. This is not the case when looking at the 1^{st} and 2^{nd} 1^+ states in ^{16}N.

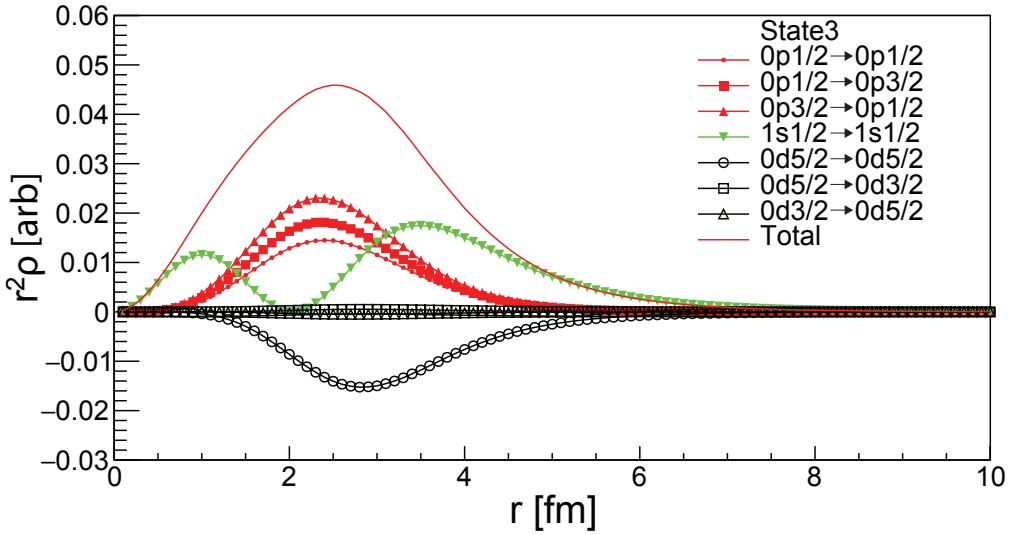

Figure 6.2: A typical transition density with its 1p-1h components. This is the calculation of the transition to the third 1^+ state in ^{16}N with the WBT interaction.

Fig. 6.3 shows the transition densities for the first two states. In both cases there is a node, and in the second state, the transition density switches sign in the interior. In β decay, the whole transition density is probed and its integral squared proportional to B(GT). In the case of the second state, the portion of the transition density that is negative will bring down the strength. However, in the (p,n) charge-exchange case, the proton does not fully penetrate the target and so only probes a portion of the transition density. Further, distortion effects bias the integration of the transition density—it enhances the role of the surface and decreases the effect of the interior. For the 2^{nd} state, this means that the charge-exchange cross section will increase because the negative portion of the transition density is suppressed. This increased cross section will give the state a increased unit cross section as seen in Fig. 2.5.

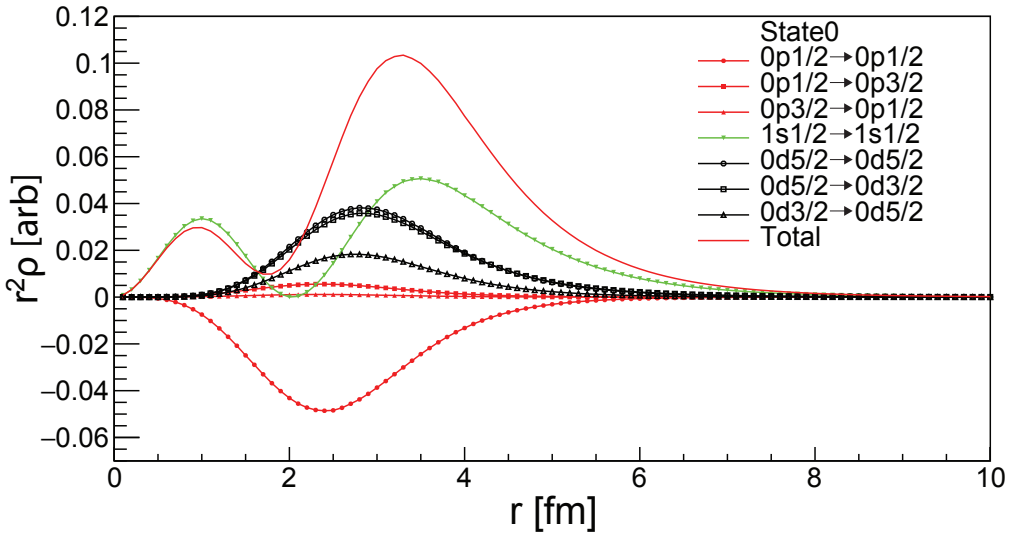

(a) State 0

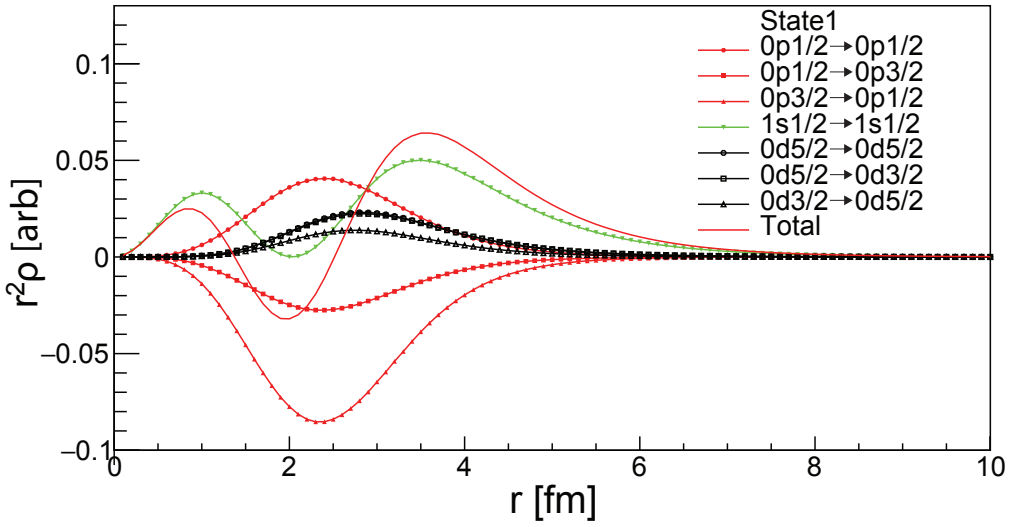

(b) State 1

Figure 6.3: The transition densities and their 1p-1h components for the first two 1^+ states in ^{16}N, calculated with the WBT interaction. The details of these states create an atypical transition density that has a significant effect on the unit cross section for these two states.

The distortion can have this effect only because of the unique and subtle details of the state. There is not one, or even two, dominate transitions that create this behavior for the second state. Instead, many things must go "wrong" at the same time. The $1s_{1/2} \rightarrow 1s_{1/2}$ transition must be strong enough to create the abnormal shape, while the p and d transitions must have the right amplitudes to keep the shape and bring a portion of the transition density below 0. While the shell-model calculation predicts this behavior for only the second state, the B(GT) extracted from the CE data for the first state also is inconsistent with the β decay value. Given the closeness of the two states in the shell model, some mixing of the two must be closer to the true states.

Since both of the states likely suffer from these effects, it motivated using the systematics of the unit cross section to find $\hat{\sigma}_{GT}$ for ^{16}C. It is interesting to note that the unit cross section determined from the sum of the two states is consistent with the $\hat{\sigma}_{GT} = 4.83 \pm 0.61\ mb/sr$ used in the analysis. The sum is $\sigma_1 + \sigma_2 = 8.01\ mb/sr$, which gives $\hat{\sigma}_{GT} = 8.01/1.69 = 4.74\ mb/sr$. This consistency gives confidence in the normalization procedure and the determination of the unit cross section.

Chapter 7

Conclusion and Outlook

Soon we will all be graduated

Unknown origin

The (p,n) charge-exchange reaction in inverse kinematics has been successfully validated as a tool for studying isovector giant resonances in neutron-rich nuclei up to high excitation energy. This was done through the measurement of the absolute, differential cross section of the ^{16}C(p,n)^{16}N reaction at 100 MeV/u and the subsequent extraction of GT and SD strength distributions up to 20 MeV of excitation energy. This was one of the first measurements of isovector giant resonances in an unstable, neutron-rich nucleus. Future experiments utilizing this technique will allow the isovector response of exotic nuclei to be probed up to high excitation energy.

Key to the success of the measurement was the development of a new digital data acquisition system for LENDA and its integration with the S800 DAQ. E10003 was the first experiment at the NSCL to combine the Pixie digital system with the analog S800 DAQ—laying the foundation for future NSCL experiments. The results of the experiment were compared with detailed shell-model calculations, which gave a measure of their reliability in the neutron-rich, high-excitation energy regime. With the full GT resonance measured, a summed GT spectrum was produced, allowing for the quenching of GT strength in a neutron-rich nucleus to be determined and discussed. Alongside this broad information, there was

sufficient resolution to analyze the details of the first two 1^+ states in ^{16}N, where peculiar structure effects were found.

There is an exciting future for the (p,n) probe inverse kinematics. The first measurement of GT strength in a heavy, neutron-rich system (^{132}Sn(p,n)^{132}Sb) has already been performed at RIKEN and is in its final stages of analysis. The next NSCL experiment has already been approved, in which the (p,n) probe will be validated on the proton-rich side through the ^{11}C(p,n)^{11}N and ^{12}N(p,n)^{12}O reactions at 100 MeV/u. These initial, proof-of-principle experiments prepare the charge-exchange group for future (p,n) experiments in the FRIB era. There increased beam rates and optimized detector systems will allow for ambitious measurements of isovector strength in highly exotic nuclei.

APPENDICES

Appendix A

Derivation of the Gamow-Teller Sum Rule

This appendix presents a derivation of the model independent Gamow-Teller (GT) sum rule, first derived by Ikeda in 1964 [119]. Sum rules exists for the other giant resonances, but are not disccused here. The interested reader is directed to Ref. [14] for more information. Beginning with the definition of the total GT strength,

$$S_{\pm} = \left| \sum_{\mu f} \langle f|\hat{\beta}_{\mu\pm}|i\rangle \right|^2 , \tag{A.1}$$

and

$$\hat{\beta}_{\mu\pm} = \frac{1}{2} \sum_{k}^{A} \hat{\sigma}_{\mu} \hat{\tau}_{\pm k}, \tag{A.2}$$

where the sum over μ goes through the components of $\hat{\sigma}_{\mu}$ $(-1, 0, +1)$, and sum over f goes through all possible final states—summing up the total strength. Each $\hat{\sigma}_{\mu}$ is a Pauli matrix and is related to the spin operator by $\hat{s} = 2\hat{\sigma}$. The expression above can be rewritten as,

$$S_{\pm} = \sum_{\mu f} \langle f|\hat{\beta}_{\mu\pm}|i\rangle^{*} \langle f|\hat{\beta}_{\mu\pm}|i\rangle , \tag{A.3}$$

$$S_{\pm} = \sum_{\mu f} \langle i|\hat{\beta}^{\dagger}_{\mu\pm}|f\rangle \langle f|\hat{\beta}_{\mu\pm}|i\rangle \,, \tag{A.4}$$

$$S_{\pm} = \sum_{\mu} \langle i|\hat{\beta}^{\dagger}_{\mu\pm}\hat{\beta}_{\mu\pm}|i\rangle \,. \tag{A.5}$$

Considering the difference $S_- - S_+$ and noting that $\hat{\tau}^{\dagger}_{\pm} = \hat{\tau}_{\mp}$,

$$S_- - S_+ = \frac{1}{4}\sum_{\mu k} \langle i|\hat{\sigma}^{\dagger}_{\mu k}\hat{\sigma}_{\mu k}\hat{\tau}_{+k}\hat{\tau}_{-k} - \hat{\sigma}^{\dagger}_{\mu k}\hat{\sigma}_{\mu k}\hat{\tau}_{-k}\hat{\tau}_{+k}|i\rangle \,. \tag{A.6}$$

Recognizing that $\sum_{\mu} \hat{\sigma}^{\dagger}_{\mu}\hat{\sigma}_{\mu} = 3$, the expression reduces to,

$$S_- - S_+ = \frac{3}{4}\sum_{k} \langle i|\hat{\tau}_{+k}\hat{\tau}_{-k} - \hat{\tau}_{-k}\hat{\tau}_{+k}|i\rangle \,. \tag{A.7}$$

Using the following values for the τ operators, the above expression can be further simplified: $\hat{\tau}_+ |n\rangle = \hat{\tau}_- |p\rangle = 0$, $\hat{\tau}_+\hat{\tau}_- |n\rangle = 4|n\rangle$, and $\hat{\tau}_-\hat{\tau}_+ |p\rangle = 4|p\rangle$. The first term in A.7 will count 4 times the number of neutrons, while the second term will count 4 times the number of protons in the initial state. This gives the resulting sum rule,

$$S_- - S_+ = 3(N - Z). \tag{A.8}$$

For the case of neutron-rich nuclei the strength in the $\Delta T_z = +1$ direction can be small due to Pauli blocking, resulting in the approximation,

$$S_- \approx 3(N - Z). \tag{A.9}$$

This gives a simple and powerful statement on the total GT strength one can expect to see for a given initial nucleus.

Appendix B

Energy of a Compton Edge

This appendix presents a short derivation of the expected energy of a Compton edge in a detector given a known γ decay energy. It is written down so that future students will not make the same foolish mistake that I have made. This mistake is indicated below in bold font. We being with the Compton scattering formula,

$$\lambda_f - \lambda_i = \frac{h}{m_e c} \left(1 - cos(\theta)\right), \tag{B.1}$$

where λ denotes the wave length, h the plank constant, m_e the mass of the electron, and θ the scattering angle. Rewriting this in terms of energy,

$$\frac{1}{E_f^\gamma} - \frac{1}{E_i^\gamma} = \frac{1}{m_e c^2}(1 - cos(\theta)) \tag{B.2}$$

where it is **important to remember that this is the energy of the recoiling γ not the electron that will deposit energy into the detector.** Rearranging,

$$E_f^\gamma = \frac{E_i^\gamma m_e c^2}{(1 - cos(\theta))E_i^\gamma + m_e c^2}. \tag{B.3}$$

The Compton edge will occur at the energy where the recoiled electron is maximized, meaning the final energy of the γ is minimized. Setting $cos(\theta) = -1$ gives,

$$E_f^\gamma = \frac{E_i^\gamma m_e c^2}{2E_i^\gamma + m_e c^2}. \tag{B.4}$$

As an example consider the 661 keV γ ray from ^{137}Cs. Equation B.4 gives $E_f^\gamma = 184$ keV. This makes the energy of the scattered electron 661 keV - 184 keV=477 keV. Hence we expect to see the Compton edge at 477 keV.

Appendix C

The Number of Beam Particles in a Beam Bunch

Beam-based nuclear physics experiments performed at incident particle rates that are an appreciable fraction of the underlying RF frequency of the accelerator require special considerations when determining the true incident beam rate from a direct measurement. This appendix will discuss some of the difficulties and derive some important relations.

Suppose we have an incident beam rate given by R and a RF frequency given by RF. This means that in a 1-second period we have a total of RF buckets to place randomly R particles. The total number of ways that the particles can be arranged where any number of particles are allowed in a bucket is given by,

$$ {}_nH_r = {}_{n+r-1}C_r = \frac{(n+r-1)!}{r!(n-1)!}, \tag{C.1} $$

where n is number of buckets, r is the number of particles, and C is a binomial coefficient. Figure C.1 shows a simple example of the case of 2 particles distributed in 3 possible buckets. From inspection it is clear that there are 6 possible configurations. For this case we can

readily confirm the validity of Equation C.1 as

$$ {}_3H_2 = \frac{(3+2-1)!}{2!(3-1)!} = \frac{(4)!}{2!(2)!} = \frac{(4)!}{4} = 6. \tag{C.2} $$

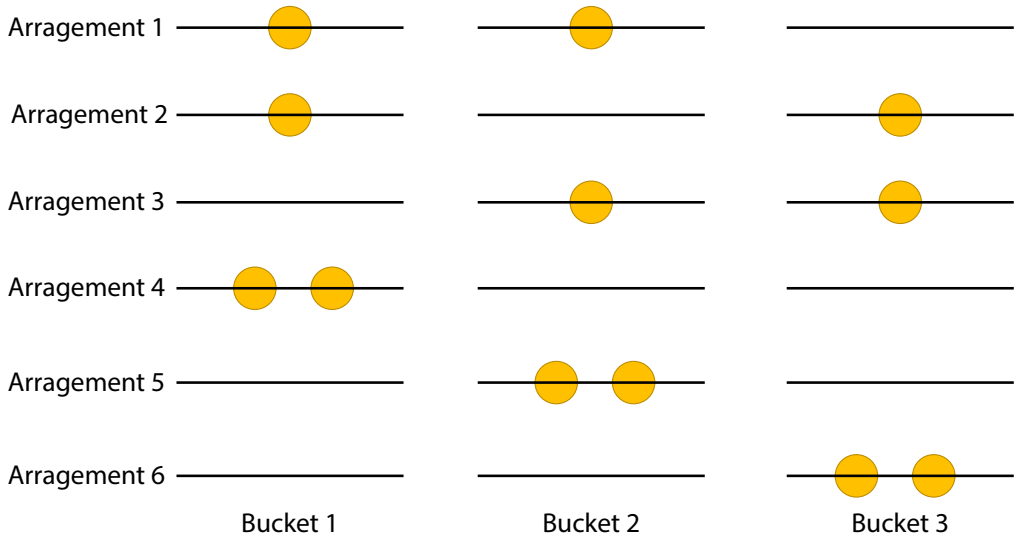

Figure C.1: The figure shows all possible ways to distribute 2 particles into 3 buckets. Each row in the figure indicates a different arrangement of particles, giving a total of 6 possible configurations.

The number of instances when a given bucket contains zero particles is given by,

$$ {}_{n-1}H_r = \frac{(n+r-2)!}{r!(n-2)!}. \tag{C.3} $$

${}_nH_r$ gives the total number of possible arrangements for n buckets and r particles. The case where there are $n+1$ buckets but that extra bucket contains no particles is the same situation as the number of arrangements where a particular bucket contains zero particles in the case of n buckets and r particles. This gives an intuitive reason for the $n-1$ in Equation

C.3. Utilizing Equation C.3 and comparing it to Fig. C.1, we can confirm that the total number of arrangements with a given empty bucket should be 3,

$$_{3-1}H_2 = \frac{(3+2-2)!}{2!(3-2)!} = \frac{(3)!}{2!} = 3. \tag{C.4}$$

Generalizing this relation to the number of configurations where a bunch has k particles in it,

$$_{n-1}H_{r-k} = \frac{(n+r-k-2)!}{(r-k)!(n-2)!}. \tag{C.5}$$

To complete the example, we can calculate the number of configurations where a bucket contains 1 and 2 particles given 3 possible buckets and 2 particles,

$$_{3-1}H_{2-1} = \frac{(3+2-1-2)!}{(2-1)!(3-2)!} = \frac{2!}{1!} = 2, \tag{C.6}$$

and

$$_{3-1}H_{2-2} = \frac{(3+2-2-2)!}{(2-2)!(3-2)!} = \frac{1!}{1!} = 1. \tag{C.7}$$

Knowing the total number configurations for each number of particles, the probability to find a certain number of particles in a bucket can be calculated as,

$$P_k(n,r) = \frac{_{n-1}H_{r-k}}{_nH_r}. \tag{C.8}$$

Using Equations C.1 and C.3, we can calculate the ratio of the number of buckets with

greater than 1 particle $S_{>1}$ to the number with just 1 particle S_1,

$$\begin{aligned}\frac{S_{>1}}{S_1} &= \frac{{}_{n-1}H_{r-2} + {}_{n-1}H_{r-3} + \cdots {}_{n-1}H_0}{{}_{n-1}H_{r-1}} \\ &= \frac{-{}_{n-1}H_r + {}_{n-1}H_r - {}_{n-1}H_{r-1} + {}_{n-1}H_{r-1} + {}_{n-1}H_{r-2} + {}_{n-1}H_{r-3} + \cdots {}_{n-1}H_0}{{}_{n-1}H_{r-1}} \\ &= \frac{{}_nH_r - {}_{n-1}H_r - {}_{n-1}H_{r-1}}{{}_{n-1}H_{r-1}},\end{aligned} \tag{C.9}$$

where in the last step, the following was used,

$${}_nH_r = {}_{n-1}H_{r-1} + {}_{n-1}H_{r-2} \ldots + {}_{n-1}H_0. \tag{C.10}$$

Reducing the expression further,

$$\begin{aligned}&= \frac{{}_nH_r - {}_{n-1}H_r - {}_{n-1}H_{r-1}}{{}_{n-1}H_{r-1}} \\ &= \frac{{}_nH_r}{{}_{n-1}H_{r-1}} - \frac{{}_{n-1}H_r}{{}_{n-1}H_{r-1}} - \frac{{}_{n-1}H_{r-1}}{{}_{n-1}H_{r-1}} \\ &= \frac{{}_nH_r}{{}_{n-1}H_{r-1}} - \frac{{}_{n-1}H_r}{{}_{n-1}H_{r-1}} - 1 \\ &= \frac{(n+r-1)!(r-1)!(n-2)!}{r!(n-1)!(n+r-3)!} - \frac{(n+r-2)!(r-1)!(n-2)!}{r!(n-2)!(n+r-3)!} - 1 \\ &= \frac{(n+r-1)(n+r-2)}{r(n-1)} - \frac{(n+r-2)}{r} - 1 \\ &= \frac{r-1}{n-1}.\end{aligned} \tag{C.11}$$

This yields a useful relation for incident beam rate,

$$\frac{S_{>1}}{S_1} = \frac{r-1}{n-1}, \tag{C.12}$$

which for $r >> 1$ and $n >> 1$ reduces further to,

$$\frac{S_{>1}}{S_1} = \frac{r}{n}. \tag{C.13}$$

Given the known number of buckets in a 1 second period (the RF rate) and the ratio of single particle to multi-particle buckets, the average incident particle rate can be determined.

Correcting an In-Beam Scaler Measurement

If the incoming beam rate is directly measured with an in-beam detector (a plastic scintillator for example), corrections will have to be made to the measured rate because of multi-particle buckets. The scaler will count only once if there is a bucket containing more than one beam particle, therefore the probabilities for each number of particles needs to be calculated. This can be done using Equation C.8,

$$\begin{aligned} P_0(n,r) &= \frac{{}_{n-1}H_{r-0}}{{}_nH_r} \\ &= \frac{(n-2+r)!r!(n-1)!}{r!(n-2)!(n+r-1)!} \\ &= \frac{(n-1)}{(n+r-1)}, \end{aligned} \tag{C.14}$$

$$\begin{aligned} P_1(n,r) &= \frac{{}_{n-1}H_{r-1}}{{}_nH_r} \\ &= \frac{(n-3+r)!r!(n-1)!}{(r-1)!(n-2)!(n+r-1)!} \\ &= \frac{r(n-1)}{(n+r-1)(n+r-2)}, \end{aligned} \tag{C.15}$$

and

$$\begin{aligned} P_2(n,r) &= \frac{{}_{n-1}H_{r-2}}{{}_nH_r} \\ &= \frac{(n-4+r)!r!(n-1)!}{(r-2)!(n-2)!(n+r-1)!} \\ &= \frac{r(r-1)(n-1)}{(n+r-1)(n+r-2)(n+r-3)}. \end{aligned} \tag{C.16}$$

Continuing the clear pattern, the following are presented for completeness:

$$\begin{aligned} P_3(n,r) &= \frac{{}_{n-1}H_{r-3}}{{}_nH_r} \\ &= \frac{r(r-1)(r-2)(n-1)}{(n+r-1)(n+r-2)(n+r-3)(n+r-4)}, \end{aligned} \tag{C.17}$$

$$\begin{aligned} P_4(n,r) &= \frac{{}_{n-1}H_{r-4}}{{}_nH_r} \\ &= \frac{r(r-1)(r-2)(r-3)(n-1)}{(n+r-1)(n+r-2)(n+r-3)(n+r-4)(n+r-5)}, \end{aligned} \tag{C.18}$$

$$\begin{aligned} P_5(n,r) &= \frac{{}_{n-1}H_{r-5}}{{}_nH_r} \\ &= \frac{r(r-1)(r-2)(r-3)(r-4)(n-1)}{(n+r-1)(n+r-2)(n+r-3)(n+r-4)(n+r-5)(n+r-6)}, \end{aligned} \tag{C.19}$$

and

$$\begin{aligned} P_6(n,r) &= \frac{{}_{n-1}H_{r-6}}{{}_nH_r} \\ &= \frac{r(r-1)(r-2)(r-3)(r-4)(r-5)(n-1)}{(n+r-1)(n+r-2)(n+r-3)(n+r-4)(n+r-5)(n+r-6)(n+r-7)}. \end{aligned} \tag{C.20}$$

Taking the RF rate from e10003 of 21.8259 MHz and considering a one second period, the following table can be generated using Equations C.14 through C.20,

R_T	N_0	N_1	N_2	...	N_6	R_m	R_T/R_m
5.00E+5	2.13E+07	4.78E+05	1.07E+04	...	2.69E-03	4.89E+05	1.023
1.00E+6	2.09E+07	9.14E+05	4.01E+04	...	1.48E-01	9.56E+05	1.046
1.50E+6	2.04E+07	1.31E+06	8.45E+04	...	1.44E+00	1.40E+06	1.069
2.00E+6	2.00E+07	1.68E+06	1.41E+05	...	6.99E+00	1.83E+06	1.092
2.50E+6	1.96E+07	2.01E+06	2.07E+05	...	2.31E+01	2.24E+06	1.115
3.00E+6	1.92E+07	2.32E+06	2.80E+05	...	5.97E+01	2.64E+06	1.137
3.50E+6	1.88E+07	2.60E+06	3.59E+05	...	1.31E+02	3.02E+06	1.160
4.00E+6	1.84E+07	2.86E+06	4.42E+05	...	2.55E+02	3.38E+06	1.183
4.50E+6	1.81E+07	3.09E+06	5.29E+05	...	4.51E+02	3.73E+06	1.206
5.00E+6	1.78E+07	3.31E+06	6.17E+05	...	7.45E+02	4.07E+06	1.229
5.50E+6	1.74E+07	3.51E+06	7.06E+05	...	1.16E+03	4.39E+06	1.252

where R_T is the true number of particles, N_x is the number of buckets containing x particles and R_m is the sum $\sum_{x=1}^{6} N_x$. An in beam detector will measure R_m since the scalar will only count once when there is one or more particles in the bucket. To correct for this the measured rate only needs to be multiplied by the correction factor seen in the last column of the table. As the true rate increases, the size of this effect becomes more significant.

It is convenient to express this correction as a linear fit to the points given in the last column as a function of the measured rate in the object scintillator (R_{object}),

$$R_{cor} = 5.6 \cdot 10^{-8} R_{object} + 0.99. \tag{C.21}$$

This expression is used in the analysis of the experimental data.

BIBLIOGRAPHY

BIBLIOGRAPHY

[1] E. Rutherford, "LXXIX. The scattering of α and β particles by matter and the structure of the atom," *The London, Edinburgh, and Dublin Philosophical Magazine and Journal of Science*, vol. 21, p. 669, 1911.

[2] J. Erler, N. Birge, M. Kortelainen, W. Nazarewicz, E. Olsen, A. M. Perhac, and M. Stoitsov, "The limits of the nuclear landscape," *Nature*, vol. 486, p. 509, 2012.

[3] K. Gelbke *et al.*, *Isotope Science Facility at Michigan State University*. 2006.

[4] M. G. Mayer, "On Closed Shells in Nuclei," *Physical Review*, vol. 74, p. 235, 1948.

[5] E. Feenberg, K. C. Hammack, and M. G. Mayer, "On Closed Shells in Nuclei. II," *Physical Review*, vol. 75, p. 1877, 1949.

[6] O. Haxel, J. H. D. Jensen, and H. E. Suess, "On the "Magic numberNOTs" in Nuclear Structure," *Physical Review*, vol. 75, p. 1766, 1949.

[7] B. A. Brown, "Lecture Notes in Nuclear Structure Physics," November 2005.

[8] B. A. Brown, "Oxbash for Windows," 2004.

[9] B. A. Brown and W. D. M. Rae, "The Shell-Model Code NuShellX@MSU," *Nuclear Data Sheets*, vol. 120, p. 115, 2014.

[10] A. Gade and T. Glasmacher, "In-beam nuclear spectroscopy of bound states with fast exotic ion beams," *Progress in Particle and Nuclear Physics*, vol. 60, p. 161, 2008.

[11] T. Otsuka, R. Fujimoto, Y. Utsuno, B. A. Brown, M. Honma, and T. Mizusaki, "Magic numberNOTs in exotic nuclei and spin-isospin properties of the NN interaction," *Physical Review Letters*, vol. 87, p. 082502, 2001.

[12] T. Otsuka, T. Suzuki, R. Fujimoto, H. Grawe, and Y. Akaishi, "Evolution of nuclear shells due to the tensor force," *Physical Review Letters*, vol. 95, p. 232502, 2005.

[13] W. Bethe and W. Gentner, "Weitere Atomumwandlunger, durch γ-Struhlen," *Zeitschrift für Physik*, vol. 19, p. 191, 1937.

[14] M. Harakeh and A. V. D. Woude, *Giant Resonances Fundemental High-Frequency Modes of Nuclear Excitation*. Oxford University Press, 2001.

[15] G. C. Baldwin and G. S. Klaiber, "Photo-fission in heavy elements," *Physical Review*, vol. 71, p. 3, 1947.

[16] G. C. Baldwin and G. S. Klaiber, "X-ray yield curves for γ-n reactions," *Physical Review*, vol. 73, p. 1156, 1948.

[17] F. Buskirk, H.-D. Gräf, R. Pitthan, H. Theissen, O. Titze, and T. Walcher, "Evidence for E2 resonances at high excitation energies in ^{208}Pb," *Physics Letters B*, vol. 42, p. 194, 1972.

[18] S. Noji, *A new spectroscopic tool by the radioactive-isotope-beam induced exothermic charge-exchange reaction*. PhD thesis, University of Tokyo, 2012.

[19] Y.-W. Lui, D. H. Youngblood, S. Shlomo, X. Chen, Y. Tokimoto, Krishichayan, M. Anders, and J. Button, "Isoscalar giant resonances in ^{48}Ca," *Physical Review C*, vol. 83, p. 044327, 2011.

[20] D. Youngblood, Y.-W. Lui, and H. Clark, "Giant resonances in ^{24}Mg," *Physical Review C*, vol. 60, p. 014304, 1999.

[21] Y. Tokimoto, Y. W. Lui, H. L. Clark, B. John, X. Chen, and D. H. Youngblood, "Giant resonances in ^{46,49}Ti," *Physical Review C*, vol. 74, p. 044308, 2006.

[22] Y. W. Lui, H. L. Clark, and D. H. Youngblood, "Giant resonances in ^{16}O," *Physical Review C*, vol. 64, p. 064308, 2001.

[23] Y.-W. Lui, P. Bogucki, J. D. Bronson, D. H. Youngblood, and U. Garg, "Giant resonaces in ^{112}Sn," *Physical Review C*, vol. 30, p. 51, 1984.

[24] M. Uchida, H. Sakaguchi, M. Itoh, M. Yosoi, T. Kawabata, Y. Yasuda, H. Takeda, T. Murakami, S. Terashima, S. Kishi, U. Garg, P. Boutachkov, M. Hedden, B. Kharraja, M. Koss, B. K. Nayak, S. Zhu, M. Fujiwara, H. Fujimura, H. P. Yoshida, K. Hara, H. Akimune, and M. N. Harakeh, "Systematics of the bimodal isoscalar giant dipole resonance," *Physical Review C*, vol. 69, p. 051301, 2004.

[25] T. Li, U. Garg, Y. Liu, R. Marks, B. K. Nayak, P. V. Madhusudhana Rao, M. Fujiwara, H. Hashimoto, K. Nakanishi, S. Okumura, M. Yosoi, M. Ichikawa, M. Itoh, R. Matsuo, T. Terazono, M. Uchida, Y. Iwao, T. Kawabata, T. Murakami, H. Sakaguchi, S. Terashima, Y. Yasuda, J. Zenihiro, H. Akimune, K. Kawase, and M. N. Harakeh, "Isoscalar giant resonances in the Sn nuclei and implications for the asymmetry term in the nuclear-matter incompressibility," *Physical Review C*, vol. 81, p. 034309, 2010.

[26] M. Itoh, H. Sakaguchi, M. Uchida, T. Ishikawa, T. Kawabata, T. Murakami, H. Takeda, T. Taki, S. Terashima, N. Tsukahara, Y. Yasuda, M. Yosoi, U. Garg, M. Hedden, B. Kharraja, M. Koss, B. K. Nayak, S. Zhu, H. Fujimura, M. Fujiwara, K. Hara,

H. P. Yoshida, H. Akimune, M. N. Harakeh, and M. Volkerts, "Systematic study of $L \leq 3$ giant resonances in Sm isotopes via multipole decomposition analysis," *Physical Review C*, vol. 68, p. 064602, 2003.

[27] M. Uchida, H. Sakaguchi, M. Itoh, M. Yosoi, T. Kawabata, H. Takeda, Y. Yasuda, T. Murakami, T. Ishikawa, T. Taki, N. Tsukahara, S. Terashima, U. Garg, M. Hedden, B. Kharraja, M. Koss, B. K. Nayak, S. Zhu, M. Fujiwara, H. Fujimura, K. Hara, E. Obayashi, H. P. Yoshida, H. Akimune, M. N. Harakeh, and M. Volkerts, "Isoscalar giant dipole resonance in ^{208}Pb via inelastic α scattering at 400 MeV and nuclear incompressibility," *Physics Letters B*, vol. 557, p. 12, 2003.

[28] B. K. Nayak, U. Garg, M. Hedden, M. Koss, T. Li, Y. Liu, P. V. Madhusudhana Rao, S. Zhu, M. Itoh, H. Sakaguchi, H. Takeda, M. Uchida, Y. Yasuda, M. Yosoi, H. Fujimura, M. Fujiwara, K. Hara, T. Kawabata, H. Akimune, and M. N. Harakeh, ""Bi-modal" isoscalar giant dipole strength in ^{58}Ni," *Physics Letters B*, vol. 637, p. 43, 2006.

[29] M. Itoh, H. Sakaguchi, M. Uchida, T. Ishikawa, T. Kawabata, T. Murakami, H. Takeda, T. Taki, S. Terashima, N. Tsukahara, Y. Yasuda, M. Yosoi, U. Garg, M. Hedden, B. Kharraja, M. Koss, B. K. Nayak, S. Zhu, H. Fujimura, M. Fujiwara, K. Hara, H. P. Yoshida, H. Akimune, M. N. Harakeh, and M. Volkerts, "Compressional-mode giant resonances in deformed nuclei," *Physics Letters B*, vol. 549, p. 58, 2002.

[30] J. P. Blaizot, "Nuclear compressibilities," *Physics Reports*, vol. 64, p. 171, 1980.

[31] D. H. Youngblood, H. L. Clark, and Y.-W. Lui, "Incompressibility of Nuclear Matter from the Giant Monopole Resonance," *Physical Review Letters*, vol. 82, p. 691, 1999.

[32] D. H. Youngblood, H. L. Clark, and Y.-W. Lui, "Compressibility of Nuclear Matter from the Giant Monopole Resonance," *Nuclear Physics A*, vol. 649, p. 49, 1999.

[33] S. Nakayama, H. Akimune, Y. Arimoto, I. Daito, H. Fujimura, Y. Fujita, M. Fujiwara, K. Fushimi, H. Kohri, N. Koori, K. Takahisa, T. Takeuchi, A. Tamii, M. Tanaka, T. Yamagata, Y. Yamamoto, K. Yonehara, and H. Yoshida, "Isovector Electric Monopole Resonance in ^{60}Ni," *Physical Review Letters*, vol. 83, p. 690, 1999.

[34] R. G. T. Zegers, A. Van den Berg, S. Brandenburg, F. Fleurot, M. Fujiwara, J. Guillot, V. Hannen, M. Harakeh, H. Laurent, K. Van der Schaaf, S. Van der Werf, A. Willis, and H. Wilschut, "Search for Isovector Giant Monopole Resonances via the Pb(^{3}He,t p) Reaction," *Physical Review Letters*, vol. 84, p. 3779, 2000.

[35] M. Scott, R. G. T. Zegers, R. Almus, S. M. Austin, D. Bazin, B. A. Brown, C. Campbell, A. Gade, M. Bowry, S. Galès, U. Garg, M. N. Harakeh, E. Kwan, C. Langer, C. Loelius, S. Lipschutz, E. Litvinova, E. Lunderberg, C. Morse, S. Noji, G. Perdikakis, T. Redpath, C. Robin, H. Sakai, Y. Sasamoto, M. Sasano, C. Sullivan, J. A. Tostevin,

T. Uesaka, and D. Weisshaar, "Observation of the Isovector Giant Monopole Resonance via the ^{28}Si(^{10}Be, ^{10}B [1.74 MeV]) Reaction at 100 AMeV," *Physical Review Letters*, vol. 118, p. 172501, 2017.

[36] A. Erell, J. Alster, J. Lichtenstadt, M. A. Moinester, J. Bowman, M. Cooper, F. Irom, H. Matis, E. Piasetzky, U. Sennhause, and Q. Ingram, "Properties of the Isovector Monopole and Other Giant Resonances in Pion Charge Exchange," *Physical Review Letters*, vol. 52, p. 2134, 1984.

[37] K. Yako, H. Sagawa, and H. Sakai, "Neutron skin thickness of ^{90}Zr determined by charge exchange reactions," *Physical Review C*, vol. 74, p. 051303(R), 2006.

[38] A. Klimkiewicz, N. Paar, P. Adrich, M. Fallot, K. Boretzky, T. Aumann, D. Cortina-Gil, U. D. Pramanik, T. W. Elze, H. Emling, H. Geissel, M. Hellström, K. L. Jones, J. V. Kratz, R. Kulessa, C. Nociforo, R. Palit, H. Simon, G. Surówka, K. Sümmerer, D. Vretenar, and W. Waluś, "Nuclear symmetry energy and neutron skins derived from pygmy dipole resonances," *Physical Review C*, vol. 76, p. 051603(R), 2007.

[39] B. A. Brown, "Neutron radii in nuclei and the neutron equation of state," *Physical Review Letters*, vol. 85, p. 5296, 2000.

[40] S. Typel and B. A. Brown, "Neutron radii and the neutron equation of state in relativistic models," *Physical Review C*, vol. 64, p. 027302, 2001.

[41] S. Yoshida and H. Sagawa, "Neutron skin thickness and equation of state in asymmetric nuclear matter," *Physical Review C*, vol. 69, p. 024318, 2004.

[42] Y. Fujita, B. Rubio, and W. Gelletly, "Spin-isospin excitations probed by strong, weak and electro-magnetic interactions," *Progress in Particle and Nuclear Physics*, vol. 66, p. 549, 2011.

[43] D. H. Wilkinson, "Renormalization of the Axial-Vector Coupling Constant in Nuclear β Decay," *Physical Review C*, vol. 7, p. 930, 1973.

[44] M. P. Nakada, J. Anderson, C. Gardner, J. McClure, and C. Wong, "Neutron Spectrum from p+d Reaction," *Physical Review*, vol. 110, p. 594, 1958.

[45] J. Anderson and C. Wong, "Evidence For Charge Independence in Medium Weight Nuclei," *Physical Review Letters*, vol. 7, p. 250, 1961.

[46] P. H. Bowen, G. C. Cox, G. B. Huxtable, J. J. Thresher, and A. Langsford, "Neutrons Emitted at 0° From Nuclei Bombarded by 143 MeV Protons," *Nuclear Physics*, vol. 30, p. 475, 1962.

[47] R. R. Doering and A. Galonsky, "Observation of Giant Gamow-Teller Strength in (p,n) Reactions," *Physical Review Letters*, vol. 35, p. 1691, 1975.

[48] C. Goodman, C. Goulding, M. Greenfield, J. Rapaport, D. Bainum, C. Foster, W. Love, and F. Petrovich, "Gamow-Teller Matrix Elements from 0° (p, n) Cross Sections," *Physical Review Letters*, vol. 44, p. 1755, 1980.

[49] J. Rapaport and D. Wang, "($\vec{p}$,n) reaction on carbon isotopes at E_p=160 MeV," *Physical Review C*, vol. 36, p. 500, 1987.

[50] T. N. Taddeucci, J. Rapaport, and C. C. Fostster, "Spin excitations in ^{40}Ca(p,n)," *Physical Review C*, vol. 28, p. 2511, 1983.

[51] B. D. Anderson, R. J. Mccarthy, M. Ahmad, A. Fazely, A. M. Kalenda, J. N. Knudson, J. Watson, R. Madey, and C. C. Foster, "Comparison of 0°(p,n) cross sections and B(M1) values for seperating current and spin contributions to isovector M1 transitions," *Physical Review C*, vol. 26, p. 8, 1982.

[52] X. Yang, L. Wang, J. Rapaport, C. D. Goodman, C. Foster, Y. Wang, W. Unkelbach, E. Sugarbaker, D. Marchlenski, S. de Lucia, B. Luther, J. L. Ullmann, A. G. Ling, B. K. Park, D. S. Sorenson, L. Rybarcyk, T. N. Taddeucci, C. R. Howell, and W. Tornow, "Dipole and spin-dipole resonances in charge-exchange reactions on ^{12}C," *Physical Review C*, vol. 48, p. 1158, 1993.

[53] L. Wang, X. Yang, J. Rapaport, C. D. Goodman, C. C. Foster, Y. Wang, R. A. Lindgren, E. Sugarbaker, D. Marchlenski, S. De Lucia, B. Luther, L. Rybarcyk, T. N. Taddeucci, and B. K. Park, "^{10}B(p,n)^{10}C reaction at 186 MeV," *Physical Review C*, vol. 47, p. 2123, 1993.

[54] J. Rapaport, T. N. Taddeucci, C. Gaarde, C. D. Goodman, C. C. Foster, C. A. Goulding, D. Horen, E. Sugarbaker, T. Masterson, and D. Lind, "^{12}C(p,n)^{12}N reaction at 120, 160, and 200 MeV," *Physical Review C*, vol. 24, p. 335, 1981.

[55] M. Bhattacharya, C. D. Goodman, R. S. Raghavan, M. Palarczyk, J. Rapaport, I. J. V. Heerden, and P. Zupranski, "Measurement of Gamow-Teller Strength for ^{176}Yb$\rightarrow^{176}$Lu and the Efficiency of a Solar Neutrino Detector," *Physical Review Letters*, vol. 85, p. 4446, 2000.

[56] T. N. Taddeucci, C. A. Goulding, T. A. Carey, R. C. Byrd, C. D. Goodman, C. Gaarde, J. Larsen, D. Horen, J. Rapaport, and E. Sugarbaker, "The (p,n) reaction as a probe of beta decay strength," *Nuclear Physics A*, vol. 469, p. 125, 1987.

[57] K. P. Jackson, A. Celler, W. P. Alford, K. Raywood, R. Abegg, R. E. Azuma, C. K. Campbell, S. El-Kateb, D. Frekers, P. W. Green, O. Häusser, R. L. Helmer, R. S. Henderson, K. H. Hicks, R. Jeppesen, P. Lewis, C. A. Miller, A. Moalem, M. A.

Moinester, R. B. Schubank, G. G. Shute, B. M. Spicer, M. C. Vetterli, A. I. Yavin, and S. Yen, "The (n,p) reaction as a probe of Gamow-Teller strength," *Physics Letters B*, vol. 201, p. 25, 1988.

[58] E. R. Flynn and J. D. Garrett, "Excitation of the Parent Analogs of the ^{58}Ni Giant M1 Resonance by the Reaction ^{58}Ni(t,h)^{58}Co," *Physical Review Letters*, vol. 29, p. 1748, 1972.

[59] S. Rakers, F. Ellinghaus, R. Bassini, C. Bäumer, A. M. Van den Berg, D. Frekers, D. De Frenne, M. Hagemann, V. M. Hannen, M. N. Harakeh, M. Hartig, R. Henderson, J. Heyse, M. A. De Huu, E. Jacobs, M. Mielke, J. M. Schippers, R. Schmidt, S. Y. Van der Werf, and H. J. Wörtche, "Measuring the (d,^{2}He) reaction with the focal-plane detection system of the BBS magnetic spectrometer at AGOR," *Nuclear Instruments and Methods in Physics Research A*, vol. 481, p. 253, 2002.

[60] H. Okamura, S. Fujita, Y. Hara, K. Hatanaka, T. Ichihara, S. Ishida, K. Katoh, T. Niizeki, H. Ohnuma, H. Otsu, H. Sakai, N. Sakamoto, Y. Satou, T. Uesaka, T. Wakasa, and T. Yamashita, "Tensor analyzing power of the (d,^{2}He) reaction at 270 MeV," *Physics Letters B*, vol. 345, p. 1, 1995.

[61] T. Annakkage, J. Jgnecke, J. S. Winfield, G. R. A. Berg, J. A. Brown, G. Crawley, S. Danczyk, M. Fujiwara, D. J. Mercer, K. Pham, D. A. Roberts, and G. H. Yoo, "Isovector giant resonances in ^{6}He, ^{12}B, ^{90}Y, ^{120}In and ^{208}Tl observed in the (^{7}Li,^{7}Be) charge-exchange reaction," *Nuclear Physics A*, vol. 648, p. 3, 1999.

[62] M. Fujiwara, H. Akimune, I. Daito, and H. Ejiri, "Spin-Isospin Resonances in Nuclei," *Nuclear Physics A*, vol. 599, p. 223, 1996.

[63] M. Sasano, G. Perdikakis, R. G. T. Zegers, S. M. Austin, D. Bazin, B. A. Brown, C. Caesar, A. L. Cole, J. M. Deaven, N. Ferrante, C. J. Guess, G. W. Hitt, R. Meharchand, F. Montes, J. Palardy, A. Prinke, L. A. Riley, H. Sakai, M. Scott, A. Stolz, L. Valdez, and K. Yako, "Gamow-Teller Transition Strengths from ^{56}Ni," *Physical Review Letters*, vol. 107, p. 202501, 2011.

[64] M. Sasano, G. Perdikakis, R. G. T. Zegers, S. M. Austin, D. Bazin, B. A. Brown, C. Caesar, A. L. Cole, J. M. Deaven, N. Ferrante, C. J. Guess, G. W. Hitt, M. Honma, R. Meharchand, F. Montes, J. Palardy, A. Prinke, L. A. Riley, H. Sakai, M. Scott, A. Stolz, T. Suzuki, L. Valdez, and K. Yako, "Extraction of Gamow-Teller strength distributions from ^{56}Ni and ^{55}Co via the (p,n) reaction in inverse kinematics," *Physical Review C*, vol. 86, p. 034324, 2012.

[65] K. Langanke and G. Martínez-Pinedo, "Nuclear weak-interaction processes in stars," *Reviews of Modern Physics*, vol. 75, p. 819, 2003.

[66] R. G. T. Zegers, R. Meharchand, Y. Shimbara, S. M. Austin, D. Bazin, B. A. Brown, C. A. Diget, A. Gade, C. J. Guess, M. Hausmann, G. W. Hitt, M. E. Howard, M. King, D. Miller, S. Noji, a. Signoracci, K. Starosta, C. Tur, C. Vaman, P. Voss, D. Weisshaar, and J. Yurkon, "^{34}P(^{7}Li,^{7}Be+γ) reaction at 100A MeV in inverse kinematics.," *Physical Review Letters*, vol. 104, p. 212504, 2010.

[67] K. Yako *Unpublished*.

[68] Y. Satou, T. Nakamura, Y. Kondo, N. Matsui, Y. Hashimoto, T. Nakabayashi, T. Okumura, M. Shinohara, N. Fukuda, T. Sugimoto, H. Otsu, Y. Togano, T. Motobayashi, H. Sakurai, Y. Yanagisawa, N. Aoi, S. Takeuchi, T. Gomi, M. Ishihara, S. Kawai, H. J. Ong, T. K. Onishi, S. Shimoura, M. Tamaki, T. Kobayashi, Y. Matsuda, N. Endo, and M. Kitayama, "^{14}Be(p,n)^{14}B reaction at 69 MeV in inverse kinematics," *Physics Letters B*, vol. 697, p. 459, 2011.

[69] D. Alburger and D. Wilkinson, "Beta decay of ^{16}C and ^{17}N," *Physical Review C*, vol. 13, p. 835, 1976.

[70] C. A. Gagliardi, G. Garvey, N. Jarmie, and R. Roberston, "$0^{+}\rightarrow 0^{-}$ beta decay of ^{16}C," *Physical Review C*, vol. 27, p. 1353(R), 1983.

[71] S. Grévy, N. L. Achouri, J. C. Angélique, C. Borcea, A. Buta, F. De Oliveira, M. Lewitowicz, E. Liénard, T. Martin, F. Negoita, N. A. Orr, J. Peter, S. Pietri, and C. Timis, "Observation of a new transition in the β-delayed neutron decay of ^{16}C," *Physical Review C*, vol. 63, p. 037302, 2001.

[72] K. Snover, E. Adelberger, P. G. Ikossi, and B. A. Brown, "Proton capture to excited states of ^{16}O M1, E1, and Gamow-Teller transitions and shell model calculations," *Physical Review C*, vol. 27, p. 1837, 1983.

[73] E. K. Warburton and B. A. Brown, "Effective interactions for the $0p1s0d$ nuclear shell-model space," *Physical Review C*, vol. 46, p. 923, 1992.

[74] G. F. Bertsch and H. Esbensen, "The (p,n) reaction and the nucleon-nucleon force," *Reports on Progress in Physics*, vol. 50, p. 607, 1987.

[75] A. Arima, "History of giant resonances and quenching," *Nuclear Physics A*, vol. 649, p. 260, 1999.

[76] B. A. Brown and B. H. Wildenthal, "Experimental and theoretical Gamow-Teller beta-decay observables for the *sd*-shell nuclei," *Atomic Data and Nuclear Data Tables*, vol. 33, p. 347, 1985.

[77] B. H. Wildenthal, M. S. Curtin, and B. A. Brown, "Predicted features of the beta decay of neutron-rich *sd*-shell nuclei," *Physical Review C*, vol. 28, p. 1343, 1983.

[78] R. G. Zegers, H. Akimune, S. M. Austin, D. Bazin, A. M. D. Berg, G. P. Berg, B. A. Brown, J. Brown, A. L. Cole, I. Daito, Y. Fujita, M. Fujiwara, S. Galès, M. N. Harakeh, H. Hashimoto, R. Hayami, G. W. Hitt, M. E. Howard, M. Itoh, J. Jänecke, T. Kawabata, K. Kawase, M. Kinoshita, T. Nakamura, K. Nakanishi, S. Nakayama, S. Okumura, W. A. Richter, D. A. Roberts, B. M. Sherrill, Y. Shimbara, M. Steiner, M. Uchida, H. Ueno, T. Yamagata, and M. Yosoi, "The (t,^{3}He) and (^{3}He, t) reactions as probes of Gamow-Teller strength," *Physical Review C*, vol. 74, p. 024309, 2006.

[79] K. Yako, H. Sakai, M. B. Greenfield, K. Hatanaka, M. Hatano, J. Kamiya, H. Kato, Y. Kitamura, Y. Maeda, C. L. Morris, H. Okamura, J. Rapaport, T. Saito, Y. Sakemi, K. Sekiguchi, Y. Shimizu, K. Suda, A. Tamii, N. Uchigashima, and T. Wakasa, "Determination of the Gamow-Teller quenching factor from charge exchange reactions on ^{90}Zr," *Physics Letters B*, vol. 615, p. 193, 2005.

[80] K. J. Raywood, B. M. Spicer, S. Yen, S. A. Long, M. A. Moinester, R. Abegg, W. P. Alford, A. Celler, T. E. Drake, D. Frekers, P. E. Green, O. Häusser, R. L. Helmer, R. S. Henderson, K. H. Hicks, K. P. Jackson, R. G. Jeppesen, J. D. King, N. S. P. King, C. A. Miller, V. C. Officer, R. Schubank, G. G. Shute, M. Vetterli, J. Watson, and A. I. Yavin, "Spin-flip isovector giant resonances from the ^{90}Zr(n,p)^{90}Y reaction at 198 MeV," *Physical Review C*, vol. 41, p. 2836, 1990.

[81] T. Wakasa, H. Sakai, H. Okamura, H. Otsu, S. Fujita, S. Ishida, N. Sakamoto, T. Uesaka, Y. Satou, M. Greenfield, and K. Hatanaka, "Gamow-Teller strength of ^{90}Nb in the continuum studied via multipole decomposition analysis of the ^{90}Zr(p,n) reaction at 295 MeV," *Physical Review C*, vol. 55, p. 2909, 1997.

[82] H. Sakai and K. Yako, "Experimental determination of Gamow-Teller quenching value, Landau-Migdal parameter $g_{N\Delta}$ and pion condensation," *Nuclear Physics A*, vol. 731, p. 94, 2004.

[83] G. Martínez-Pinedo, A. Poves, E. Caurier, and A. P. Zuker, "Effective g_A in the pf shell," *Physical Review C*, vol. 53, p. R2602, 1996.

[84] F. M. Nunes and I. J. Thompson, *Nuclear Reactions for Astrophysics*. Cambridge University Press, 2009.

[85] W. G. Love and M. A. Franey, "Effective nucleon-nucleon interaction for scattering at intermediate energies," *Physical Review C*, vol. 24, p. 1073, 1981.

[86] M. A. Franey and W. G. Love, "Nucleon-nucleon t-matrix interaction for scattering at intermediate energies," *Physical Review C*, vol. 31, p. 488, 1985.

[87] R. Schaeffer, J. Raynal, and J. Comfort, "Program DW81," *unpublished*, 1981.

[88] J. Raynal, "Multipole Expansion of a Two-Body Interaction in Helicity Formalism and its Applications to Nuclear structure and Nuclear Reaction Calculations," *Nuclear Physics A*, vol. 97, p. 572, 1967.

[89] P. Schwandt and M. D. Kaitchuck, "Analyzing power of proton-nucleus elastic scattering between 80 and 180 MeV," *Physical Review C*, vol. 26, p. 55, 1982.

[90] G. Perdikakis, M. Sasano, S. M. Austin, D. Bazin, C. Caesar, S. Cannon, J. M. Deaven, H. J. Doster, C. J. Guess, G. W. Hitt, J. Marks, R. Meharchand, D. T. Nguyen, D. Peterman, A. Prinke, M. Scott, Y. Shimbara, K. Thorne, L. Valdez, and R. G. T. Zegers, "LENDA: A low energy neutron detector array for experiments with radioactive beams in inverse kinematics," *Nuclear Instruments and Methods in Physics Research A*, vol. 686, p. 117, 2012.

[91] S. Lipschutz, R. Zegers, J. Hill, S. Liddick, S. Noji, C. Prokop, M. Scott, M. Solt, C. Sullivan, and J. Tompkins, "Digital data acquisition for the Low Energy Neutron Detector Array (LENDA)," *Nuclear Instruments and Methods in Physics Research A*, vol. 815, p. 1, 2016.

[92] S. V. Paulauskas, M. Madurga, R. Grzywacz, D. Miller, S. Padgett, and H. Tan, "A digital data acquisition framework for the Versatile Array of Neutron Detectors at Low Energy (VANDLE)," *Nuclear Instruments and Methods in Physics Research A*, vol. 737, p. 22, 2014.

[93] W. A. Peters, S. Ilyushkin, M. Madurga, C. Matei, S. V. Paulauskas, R. K. Grzywacz, D. W. Bardayan, C. R. Brune, J. Allen, J. M. Allen, Z. Bergstrom, J. Blackmon, N. T. Brewer, J. A. Cizewski, P. Copp, M. E. Howard, R. Ikeyama, R. L. Kozub, B. Manning, T. N. Massey, M. Matos, E. Merino, P. D. O'Malley, F. Raiola, C. S. Reingold, F. Sarazin, I. Spassova, S. Taylor, and D. Walter, "Performance of the Versatile Array of Neutron Detectors at Low Energy (VANDLE)," *Nuclear Instruments and Methods in Physics Research A*, vol. 836, p. 122, 2016.

[94] D. Bazin, J. A. Caggiano, B. M. Sherrill, J. Yurkon, and A. Zeller, "The S800 spectrograph," *Nuclear Instruments and Methods in Physics Research B*, vol. 204, p. 629, 2003.

[95] D. J. Morrissey, B. M. Sherrill, M. Steiner, A. Stolz, and I. Wiedenhoever, "Commissioning the A1900 projectile fragment separator," *Nuclear Instruments and Methods in Physics Research B*, vol. 204, p. 90, 2003.

[96] P. A. Zavodszky, B. Arend, D. Cole, J. DeKamp, G. Machicoane, F. Marti, P. Miller, J. Moskalik, J. Ottarson, J. Vincent, and A. Zeller, "Design of SuSI - superconducting source for ions at NSCL/MSU - II. The conventional parts," *AIP Conference Proceedings*, vol. 749, p. 131, 2005.

[97] P. A. Zavodszky, B. Arend, D. Cole, J. Dekamp, G. MacHicoane, F. Marti, P. Miller, J. Moskalik, J. Ottarson, J. Vincent, A. Zeller, and N. Y. Kazarinov, "Status report on the design and construction of the Superconducting Source for Ions at the National Superconducting Cyclotron Laboratory/Michigan State University," *Review of Scientific Instruments*, vol. 77, p. 03A334, 2006.

[98] G. Machicoane, D. Cole, J. Ottarson, J. Stetson, and P. Zavodszky, "ARTEMIS-B: A room-temperature test electron cyclotron resonance ion source for the National Superconducting Cyclotron Laboratory at Michigan State University," *Review of Scientific Instruments*, vol. 77, p. 03A322, 2006.

[99] X. Wu, H. Blosser, D. Johnson, F. Marti, and R. York, "The K500-to-K1200 coupling line for the coupled cyclotron facility at the NSCL," *Proceedings of the 1999 Particle Accelerator Conference*, vol. 2, p. 1318 vol.2, 1999.

[100] D. Morrissey, "The coupled cyclotron project at the NSCL," *Nuclear Physics A*, vol. 616, p. 45, 1997.

[101] J. Yurkon, D. Bazin, W. Benenson, D. J. Morrissey, B. M. Sherrill, D. Swan, and R. Swanson, "Focal plane detector for the S800 high-resolution spectrometer," *Nuclear Instruments and Methods in Physics Research A*, vol. 422, p. 291, 1999.

[102] G. W. Hitt, *The ^{64}Zn(t,^{3}He) Charge-Exchange Reaction at 115 MeV Per Nucleon and Application to ^{64}Zn Stellar Electron-Capture*. PhD thesis, Michigan State University, 2008.

[103] G. F. Knoll, *Radiation Detection and Measurement*, vol. 3. John Wiley and Sons, 2010.

[104] R. Zegers. private communication.

[105] XIA, "Digital Gamma Finder (DGF) PIXIE-16 User's Manual," 2005.

[106] C. Prokop, S. Liddick, N. Larson, S. Suchyta, and J. Tompkins, "Optimization of the National Superconducting Cyclotron Laboratory Digital Data Acquisition System for use with fast scintillator detectors," *Nuclear Instruments and Methods in Physics Research A*, vol. 792, p. 81, 2015.

[107] C. J. Prokop, S. N. Liddick, B. L. Abromeit, A. T. Chemey, N. R. Larson, S. Suchyta, and J. R. Tompkins, "Digital data acquisition system implementation at the National Superconducting Cyclotron Laboratory," *Nuclear Instruments and Methods in Physics Research A*, vol. 741, p. 163, 2014.

[108] H. Tan, M. Momayezi, A. Fallu-Labruyere, Y. X. Chu, and W. K. Warburton, "A fast digital filter algorithm for gamma-ray spectroscopy with double-exponential decaying scintillators," *IEEE Transactions on Nuclear Science*, vol. 51, p. 1541, 2004.

[109] N. Kudomi, "Energy calibration of plastic scintillators for low energy electrons by using Compton scatterings of γ rays," *Nuclear Instruments and Methods in Physics Research A*, vol. 430, p. 96, 1999.

[110] M. Berz, K. Joh, J. A. Nolen, B. M. Sherrill, and A. F. Zeller, "Reconstructive correction of aberrations in nuclear particle spectrographs," *Physical Review C*, vol. 47, p. 537, 1993.

[111] S. Agostinelli *et al.*, "GEANT4 - A simulation toolkit," *Nuclear Instruments and Methods in Physics Research A*, vol. 506, p. 250, 2003.

[112] E. Mendoza, D. Cano-Ott, T. Koi, and C. Guerrero, "New standard evaluated neutron cross section libraries for the GEANT4 code and first verification," *IEEE Transactions on Nuclear Science*, vol. 61, p. 2357, 2014.

[113] L. Stuhl, A. Krasznahorkay, M. Csatlós, A. Algora, J. Gulyás, G. Kalinka, J. Timár, N. Kalantar-Nayestanaki, C. Rigollet, S. Bagchi, and M. A. Najafi, "A neutron spectrometer for studying giant resonances with (p,n) reactions in inverse kinematics," *Nuclear Instruments and Methods in Physics Research A*, vol. 736, p. 1, 2014.

[114] Saint-Gobain, "Organic Scintillation Materials and Assemblies," *Catalogue*, p. 16, 2015.

[115] T. N. Taddeucci, C. D. Goodman, R. C. Byrd, T. A. Carey, D. J. Horen, J. Rapaport, and E. Sugarbaker, "A neutron polarimeter for (p,n) measurements at intermediate energies," *Nuclear Instruments and Methods in Physics Research A*, vol. 241, p. 448, 1985.

[116] B. D. Anderson, A. Fazely, R. J. McCarthy, P. C. Tandy, J. W. Watson, R. Madey, W. Bertozzi, T. N. Buti, J. M. Finn, J. Kelly, M. A. Kovash, B. Pugh, B. H. Wildenthal, and C. C. Foster, "Gamow-teller strength in the ^{18}O(p,n)^{18}F reaction at 135 MeV," *Physical Review C*, vol. 27, p. 1387, 1983.

[117] W. T. Chou, E. K. Warburton, and B. A. Brown, "Gamow-Teller beta-decay rates for A$\leq$18 nuclei," *Physical Review C*, vol. 47, p. 163, 1993.

[118] S. M. Austin, N. Anantaraman, and W. G. Love, "Charge Exchange Reactions and the Efficiency of Solar Neutrino Detectors," *Physical Review Letters*, vol. 73, p. 30, 1994.

[119] K. Ikeda, "Collective Excitation of Unlike Pair States in Heavier Nuceli," *Progress of Theoretical Physics*, vol. 31, p. 434, 1964.